이학박사 학위논문

Molecular Basis of Substrate Recognition and Peptide Modification by ATP-grasp Macrocyclase PsnB

ATP-grasp 거대고리화 효소 PsnB의 기질 인식 및 펩타이드 변형 분자 기전

2022 년 8 월

서울대학교 대학원

화학부

송인석

Molecular Basis of Substrate Recognition and Peptide Modification by ATP-grasp Macrocyclase PsnB

지도 교수 김 석 희

이 논문을 이학박사 학위논문으로 제출함
2022 년 8 월

서울대학교 대학원
화학부 생화학 전공
송 인 석

송인석의 이학박사 학위논문을 인준함
2022 년 8 월

위 원 장	이 연	(인)
부위원장	김 석 희	(인)
위 원	이 형 호	(인)
위 원	송 윤 주	(인)
위 원	기 정 민	(인)

Abstract

In Seok Song
Departments of Chemistry
The Graduate School
Seoul National University

Ribosomally-synthesized and post-translationally modified peptides (RiPPs) are a kind of natural product possessing diverse post-translational modifications on their skeletal peptide chains[1]. RiPPs are thought to be a promising candidate for the discovery of bioactive molecules because of their simple biosynthetic logic and broad substrate tolerance[2,3]. Understanding the reaction mechanism of the RiPP biosynthetic enzyme provides guidance for discovering novel biofunctional molecules from the RiPP biosynthetic systems. I selected the biosynthetic gene cluster of plesiocin as a model system to figure out the molecular basis underlying biosynthesis of graspetide, a family of RiPPs bearing side-chain to side-chain macrolactone (or macrolactam) linkages[4]. Biochemical and structural analyses were performed to find the molecular details of macrocyclization step of the graspetide biosynthesis. Chapter 1 describes previous biochemical and structural studies for the RiPP biosynthesis.

In chapter 2, 3, and 4, biochemical and structural studies of plesiocin biosynthesis are described. Plesiocin is a group 2 graspetide that contains 8 ester bonds between the side-chains of the highly conserved threonine and glutamic acid residues. Ester cross-links are introduced by PsnB, an ATP-grasp ligase that consumes ATP molecules and generates macrolactones on its cognate precursor peptide, PsnA2. PsnB and PsnA2, principal enzyme and substrate pair for the plesiocin biosynthesis, are chosen for a model system in this study.

Chapter 2 describes biochemical analyses of the substrate binding and enzymatic reaction of PsnB. A minimal precursor peptide was designed for the quantitative analysis of precursor-enzyme interaction. Kinetic studies of each reaction step of PsnB revealed that the phosphorylation step and ester formation step are highly coupled. The affinity between PsnB and its substrates indicated that unusual tight interaction between PsnB and the core region of the precursor peptide via the conserved glutamic acids of the core peptide. Substrates of PsnB—leader peptide, core peptide, and nucleotide—exhibit cooperativity with each other during the enzyme binding.

In Chapter 3, structural studies of the PsnB-substrate complex are described. PsnB complex structures with various substrates display molecular details of enzyme-substrate interaction. Especially, the highly conserved Arg213 of PsnB recognizes a reaction-participating glutamic acid before the phosphorylation step. Arg235 of PsnB is proposed to act as a catalytic base that deprotonates the nucleophilic hydroxyl group of the threonine. Conformational change of PsnB was observed during the substrate binding, which resulted in cooperativity and asymmetry in PsnB-substrate interaction.

In chapter 4, I suggest models for the substrate binding and reaction mechanism of the PsnB catalysis. Roles of leader peptide, core peptide, and catalytic residues of the enzyme are also described. Combining the biochemical and structural results, the molecular mechanism underlying each step of the enzyme reaction is depicted. Collectively, this thesis glimpsed the molecular basis of the graspetide biosynthesis.

Material from: 'Song, I., Kim, Y., Yu, J. et al. Molecular mechanism underlying substrate recognition of the peptide macrocyclase PsnB. Nat Chem Biol 17, 1123–1131 (2021). https://doi.org/10.1038/s41589-021-00855-x'

Keyword : Natural product, RiPP, Graspetide, Omega-Ester-containing Peptides, ATP-grasp ligase, Molecular mechanism

Student Number : 2017-25274

Table of Contents

List of Figures

List of Tables

Chapter 1. Introduction

1.1. RiPPs

Together with the evolution of organisms competing for survival in biological community, the chemical diversity of natural products has been greatly expanded in nature. This large chemical space of natural products makes them a huge source of therapeutic compounds[5]. Recent advances in genome-mining and biosynthetic engineering tools further expanded the availability of natural products in drug discovery[6]. Among the various categories of natural products, Ribosomally-synthesized and post-translationally modified peptides (RiPPs) are peptide-based natural products that contain diverse post-translational modifications in their ribosomally-synthesized precursor peptide chain[1,4]. Post-translational modifications in RiPPs involve thioether cross-links (lanthipeptide; Figure 1A), N-to-side-chain amide bond (lasso peptide; Figure 1B), side-chain to side-chain ester or amide bond (graspetide; Figure 1C), and thazol(in)e/oxazol(in)e (LAPs; Figure 1D).

RiPPs are initially synthesized as a precursor peptide from the ribosomes and subsequently modified by the cognate modification enzymes[1,4]. The precursor peptide is frequently divided into two segments, a leader peptide (LP), which is the site for enzyme recognition and is often cleaved during the biosynthesis, and a core peptide (CP), which is the part that is modified by the modification enzymes (Figure 2). Because the substrate recognition does not solely rely on the direct binding of a modification site to the enzyme, modular RiPP biosynthesis often leads to the natural evolution of diverse core peptides and enables facile engineering of variants with higher chemical diversity. As genome sequencing technology has experienced exceeding advances and bioinformatic tools have been developed, RiPPs with unique core sequence motifs and novel post-translational modifications are being largely found by genome-mining strategies[6].

Along with the large chemical space and simple biosynthetic logic of the RiPPs, efforts have been made to utilize RiPP biosynthetic systems to discover new biofunctional molecules[6]. Since RiPP biosynthetic enzymes are thought to have high substrate tolerance at the core region of the precursor peptide, the engineering of RiPPs has focused on the sequence diversification of the core region by the site-saturation mutagenesis or library generation. By the screening or selection of the non-native RiPPs, researchers developed new modified peptides which act as novel protease inhibitors[7], antimicrobial molecules[8,9] and peptides binders for integrin[10], uPA[11], UEV[12], and spike protein[13]. Still, the RiPP biosynthetic systems that are employed in these works are limited to the systems that are well-studied and that accommodate broad substrate scope. To take advantage of diverse RiPP modification enzymes for the development of functional biomolecule, understanding the molecular mechanism of RiPP biosynthesis would be helpful.

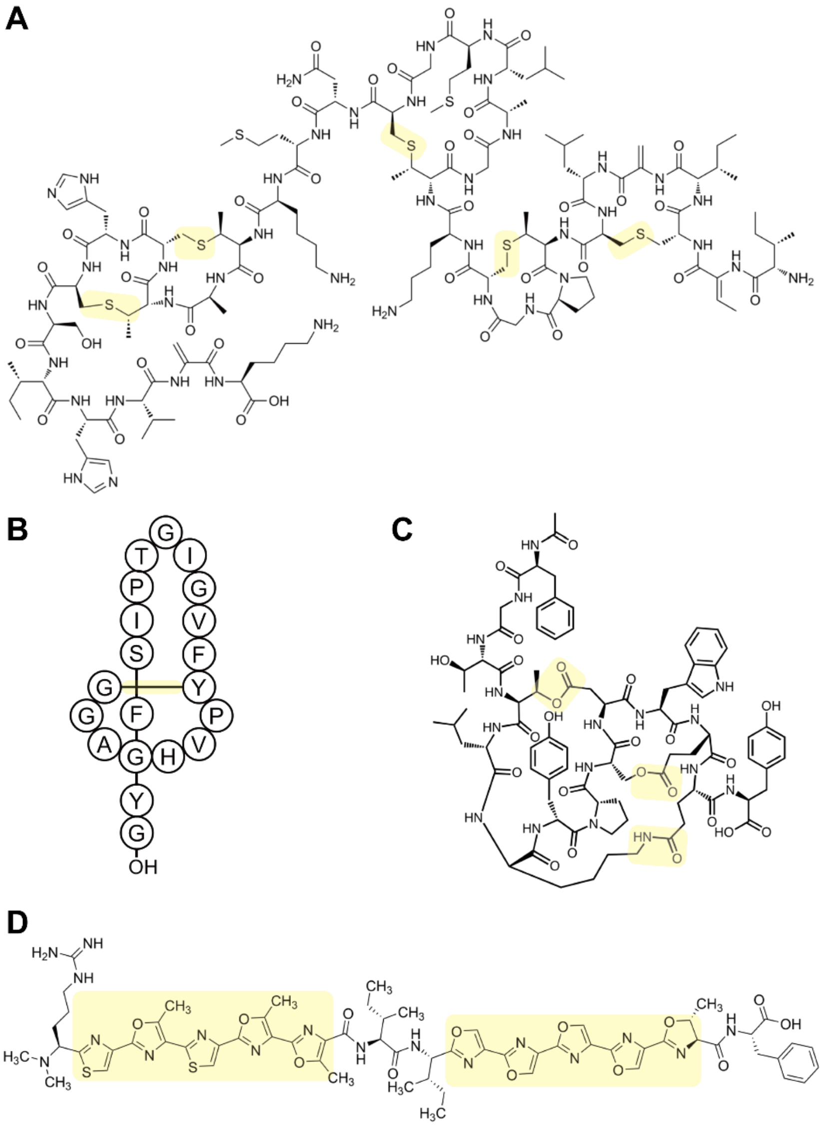

Figure 1. Structures of RiPPs. Structure of lanthipeptide (A, Nisin), lassopeptide (B, Microcin J25), graspetide (C, Microviridin), and LAP (D, Plantazolicin). Class defining modifications are colored as yellow.

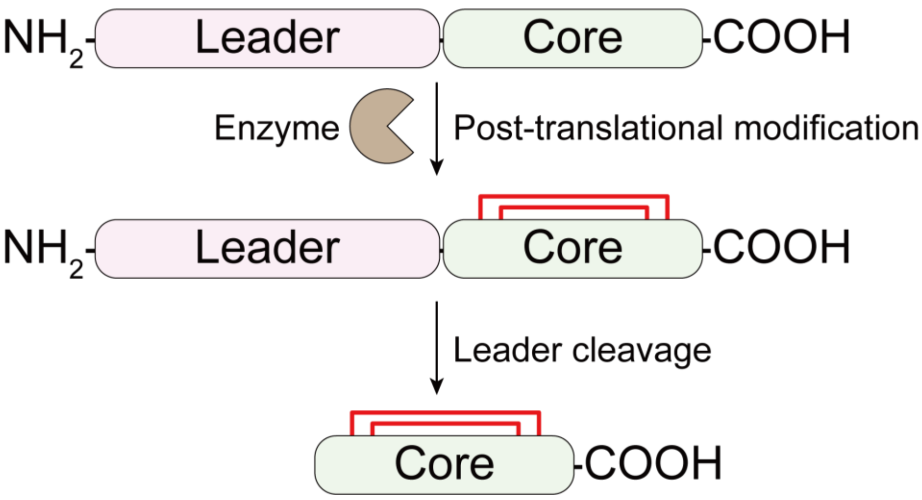

Figure 2. Biosynthesis of RiPPs. Modification enzyme recognizes the leader peptide of the precursor peptide and introduces PTMs at the core region of the precursor. Leader peptide is cleaved after the modification.

1.2. Mechanistic studies of RiPP biosynthesis

Biosynthetic mechanism of RiPPs has been discovered by structural and biochemical analyses[14]. Many structures of the enzyme-leader peptide complex have been determined and provided molecular details of leader peptide recognition by the enzymes[15-26]. Our understanding of enzyme-core interaction is, however, largely limited due to the difficulty of obtaining a complex structure of the enzyme-core peptide. Recent examples of enzyme-core peptide complex structures include the ATP-grasp ligase CdnC in graspetide biosynthesis[27] (Figure 3A), radical S-adenosylmethionine (rSAM) enzyme CteB in ranthipeptide biosynthesis[22] (Figure 3B), backbone N-methyltransferase OphMA in borosin biosynthesis[28,29] (Figure 3C), lantipeptide dehydratase NisB[30] (Figure 3D), and, while not a RiPP enzyme, thioamide-installing YcaO (Mj-YcaO)[31]. The difficulty of obtaining the enzyme-core peptide complex structure may arise from the transient nature of the enzyme-core peptide complex in enzyme reactions, and the apparent low affinity of core peptides to the cognate enzyme in many RiPP families[24,32,33]. Therefore, the above examples show only a small part of the CP (CteB)[22] or take advantage of the natural covalent linkage to the enzyme (OphMA)[28,29], the artificial fusion of a substrate mimic to the enzyme (NisB)[30], or the synonymous activity of the non-RiPP enzyme (Mj-YcaO)[31].

As it is difficult to measure the direct binding between the core peptide and the enzyme due to its transient binding property, researchers characterized enzyme-core peptide interaction by determining whether the modifications are introduced to the precursor peptide variants with diverse core peptide sequences. Site-saturation mutagenesis[34], library generation and screening[35], or in vitro translation system[36,37] were used to determine critical residues of the core peptides. The development of high-throughput assays further enhanced our understanding of enzyme-core interaction in RiPP biosynthetic enzymes[38].

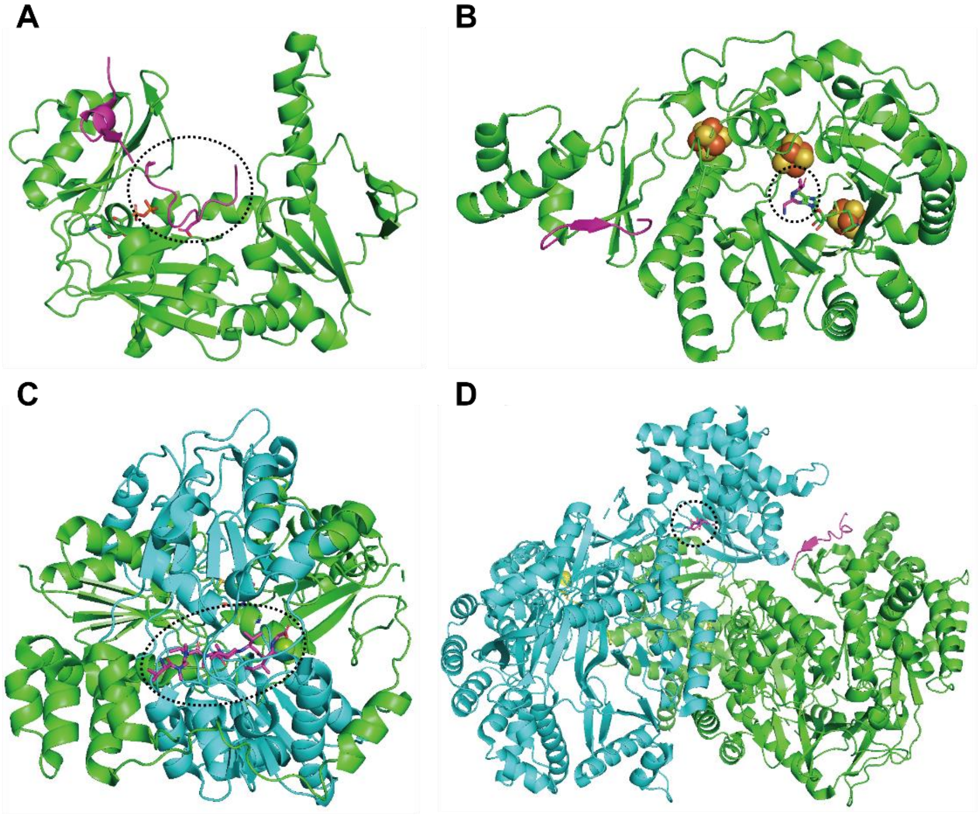

Figure 3. Structures of the core-complexed RiPP biosynthetic enzymes. Enzyme-core peptide complex structure of CdnC (A; 7MGV), CteB (B; 5WGG), OphMA (C; 5N0X), and NisB (D; 6M7Y). Enzymes are shown as green/cyan cartoon, and precursor peptides as magenta sticks. Core peptides (or core peptide mimetic) are denoted with dashed circles.

1.3. Graspetides (Omega-ester-containing peptides)

Graspetides, also known as omega-ester-containing peptides (OEPs), are RiPPs that harbor side-chain to side-chain macrolactone or macrolactam linkages between an acidic residue (Asp or Glu) and a hydroxyl- or amine-containing residue (Ser, Thr, or Lys)[4]. The very firstly discovered members of this RiPP family are microviridins (Group 1 graspetides; Figure 1C) that have a cage-like tricyclic structure with two macrolactones and one macrolactam on the highly conserved TxRxPSDxDE core motif[39-41]. Recent bioinformatic and biochemical analyses revealed 11 new or putative groups of graspetides that have novel core motifs and ring connectivities, including plesiocin and thuringinin[42-45].

Biosynthesis of macrocyclic linkages in graspetides is performed by ATP-grasp ligases[40,41]. ATP-grasp ligases contain an atypical ATP-binding site, called the ATP-grasp fold, and are situated within many diverse biological systems such as purine biosynthesis (PurD, PurT, PurK, and PurP)[46-49], glutathione biosynthesis (GSHase)[50], fatty acid biosynthesis (Acetyl-CoA carboxylase)[51], and peptidoglycan biosynthesis (DDLigase)[52,53]. ATP-grasp fold consists of three common conserved domains, called A-C domains. Domain A and C assemble and form a large central core that contains substrate binding sites. ATP binds between the B domain and A/C central domain. ATP-grasp ligases catalyze the ATP-assisted reaction of a carboxyl group with a nucleophile (amine or hydroxyl) via the formation of an acyl-phosphate intermediate. In graspetide biosynthesis, ATP-grape ligases use ATP to activate a carboxyl side-chain by phosphorylation and mediate the nucleophilic substitution of a hydroxyl or amine group to form an ester or amide bond (Figure 4). The presence of topologically diverse graspetides and simple biosynthesis logic suggests that the formation of multi-cyclic peptides by side-chain to side-chain crosslinking is a simple but powerful strategy to expand the chemical space of peptides both in natural evolution[44,54] and for engineering novel functionalities[7,34,55].

Recent structural analyses unearthed the molecular mechanism of the graspetide biosynthesis. In 2016, two crystal structures of the ATP-grasp enzymes in microviridin biosynthesis, an apo form of MdnB and a MdnC-LP complex, revealed a novel LP-binding domain and a distinct conformational change of the enzyme upon the leader binding—the movement of the β9β10 loop by 25 Å opens the core binding site[24]. These structures, however, showed neither the core peptide nor the nucleotide in the electron density maps, leaving a question about how the enzyme recognizes the core peptide and proceeds to the specific phosphorylation and following ligation of the acidic residue. More recently, a quaternary complex structure of CdnC that binds to leader peptide, core peptide, and ADP was determined. CdnC complex structure revealed a large conformational change upon the substrate binding and also CdnC interactions with leader peptide, core peptide, and ADP[27].

Here, I characterized the mechanism underlying precursor recognition and ester formation reaction using plesiocin biosynthesis as a model system (Figure 5). Biochemical studies revealed that the binding of the leader peptide and a nucleotide promotes core peptide binding and that the core peptide enhances the enzyme-precursor interaction. Eight crystal structures of PsnB, including those with the well-resolved nucleotide, leader peptide and even core peptide, revealed residues involved in the substrate binding and showed the conformational changes of the PsnB dimer upon substrate recognition. Collectively, these results suggest a molecular mechanism for the precursor binding and activation of graspetide biosynthetic enzymes.

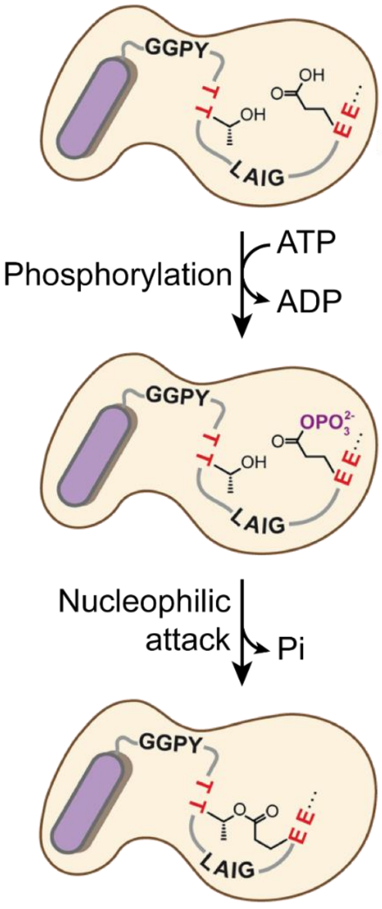

Figure 4. Biosynthetic scheme of graspetide. After substrate binding, the carboxylic acid side-chain is phosphorylated by using ATP. Acyl-phosphate intermediate then reacts with hydroxyl (or amine) to form an ester (or amide) bond.

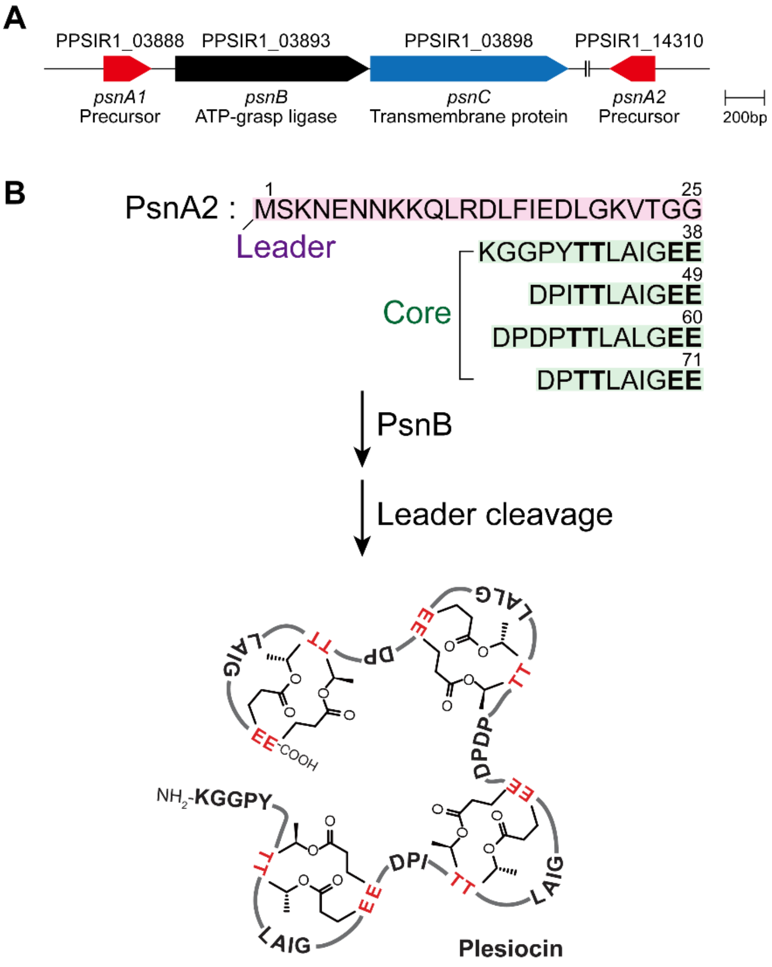

Figure 5. Introduction of plesiocin biosynthesis. (A) Plesiocin biosynthetic gene cluster. (B) Sequence of precursor peptide PsnA2 and biosynthesis of plesiocin. PsnA2 consists of leader peptide (PsnA2$_{1\text{-}25}$) and core peptide (PsnA2$_{26\text{-}71}$). PsnB introduces ester bonds to PsnA2. Plesiocin is produced after the leader cleavage.

Chapter 2. Substrate binding and enzymatic reaction of PsnB

2.1. Minimal precursor peptide design as a model substrate.

To study the molecular mechanism of substrate recognition and macrocyclization reaction in graspetides, I chose precursor peptide (PsnA2) and ATP-grasp ligase (PsnB) from the plesiocin biosynthetic gene cluster as a model system (Figure 5A). PsnB installs two macrolactones on each of the four conserved TTxxxxEE core motifs of PsnA2 and the following leader cleavage produces the plesiocin[42] (Figure 5B). To quantitatively analyze the multiple steps of the macrocyclization reaction—precursor binding, ATP consumption, and macrolactone formation—I started by finding a minimal precursor peptide that contains only the essential residues of the leader peptide and one core motif. Previous report showed that the conserved region of the leader peptide, LFIEDL (PsnA2$_{14\text{-}19}$; Figure 6A) is essential for the complete macrocyclization reaction[42]. Here, I examined whether PsnA2$_{14\text{-}19}$ is required for the enzyme binding step by using fluorescence anisotropy of fluorophore-labeled leader peptide (Fl_LP) and its variants. Indeed, PsnA2$_{14\text{-}19}$ was a key residue for tight enzyme binding, whereas the N-terminal 13 residues were dispensable. Therefore, I chose PsnA2$_{14\text{-}38}$ as the minimal precursor peptide (MP) for further studies (Figures 6B and C).

As the macrocyclization reaction shifts the molecular mass of precursor peptide to about -18 Da, the kinetics of the macrocyclization reaction of PsnB can be qualitatively estimated by MALDI spectra of the reaction solution. For both minimal precursor peptide and wild-type PsnA2, macrocyclization reaction is carried out by PsnB at a similar reaction rate, whose k_{cat} value was estimated at about 7–14 min^{-1} (Figure 7). As a result, the minimal precursor peptide behaves similarly to the wild-type PsnA2, which allows further quantitative analysis of the molecular interaction between PsnB and PsnA2 by using a designed minimal precursor peptide. Reaction kinetics of ATP hydrolysis of PsnB was also measured by using ATPase assay which quantifies the amount of ATP consumed[56]. For increasing amounts of minimal precursor peptide, the K_M and k_{cat} values were measured to be 30 μM and 14 min^{-1}, respectively (Figure 8A), which are similar to those of AMdnC, an ATP-grasp ligase of Group 1 graspetide (K_M = 27 μM and k_{cat} = 12 min^{-1})[57]. Titration with ATP resulted in K_M and k_{cat} of 92 μM and 16 min^{-1} (Figure 8B), of which K_M is comparable to those of non-RiPP ATP-grasp enzymes, glutathione synthetase (240 μM)[58], and D-ala-D-ala ligase (49 μM)[59]. $MgCl_2$ titration revealed that 10 mM of Mg^{2+} was sufficient for the full activity of PsnB (Figure 8C).

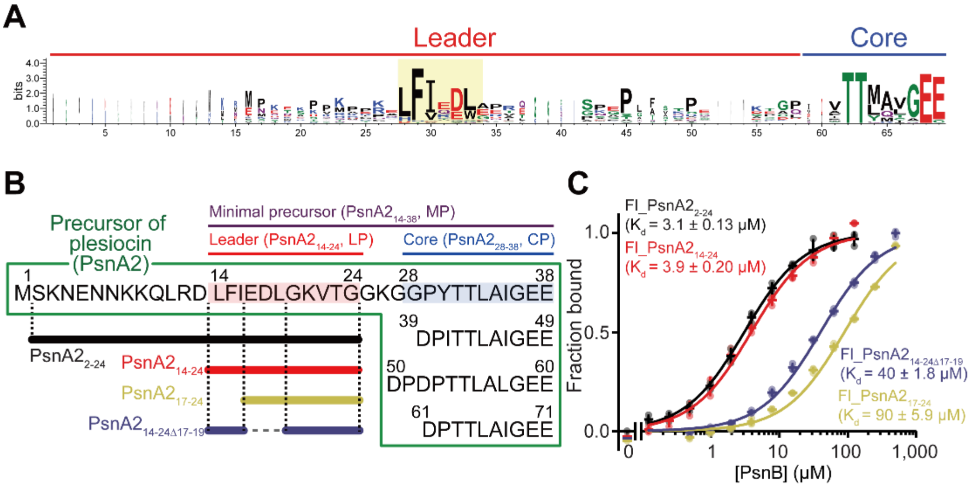

Figure 6. Minimal precursor design. (A) Sequence conservation of the leader peptide and first core motif of group 2 graspetide precursor peptide. LFIEDL region of the leader peptide is highly conserved. (B) Minimal precursor peptide (MP; PsnA2$_{14–38}$; overlined with purple) was designed from the native sequence of PsnA2. Minimal precursor peptide contains the key region of the leader peptide (PsnA2$_{14–24}$; red) and one core peptide (PsnA2$_{28–38}$; blue). Variants of the leader peptide used in (C) are shown as solid lines below PsnA2. (C) The affinity of the leader peptide variants was determined by measuring the fluorescence anisotropy of fluorophore-labeled LP variants (0.1 μM) with different concentrations of PsnB. Data are presented as dot plots with mean ± 1 s.d. (n = 3 independent experiments) and are fitted to a hyperbolic equation.

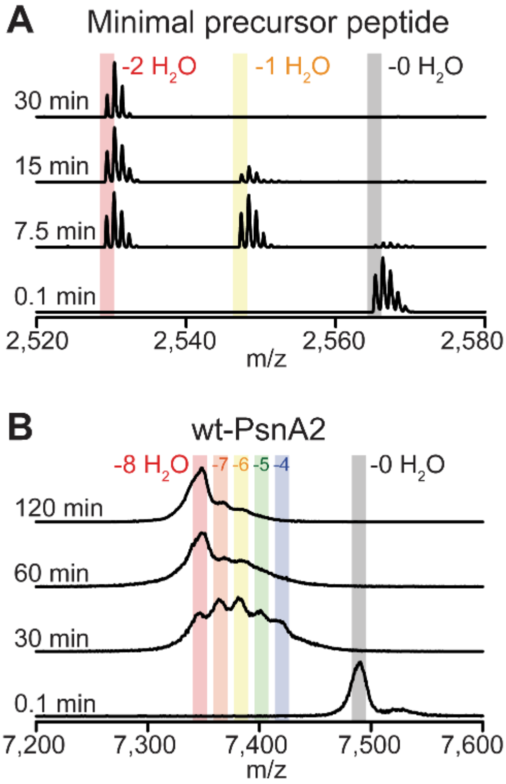

Figure 7. Modification of minimal precursor peptide. 50 μM minimal precursor (A; the product contains two ester bonds) or wild-type PsnA2 (B; the product contains eight ester bonds) was co-incubated with 0.5 μM PsnB in buffer A (100 mM Tris pH 7.3, 50 mM KCl, 5 mM ATP, and 10 mM $MgCl_2$) at 37 ℃, and the reaction solutions at designated time points were analyzed by MALDI-MS.

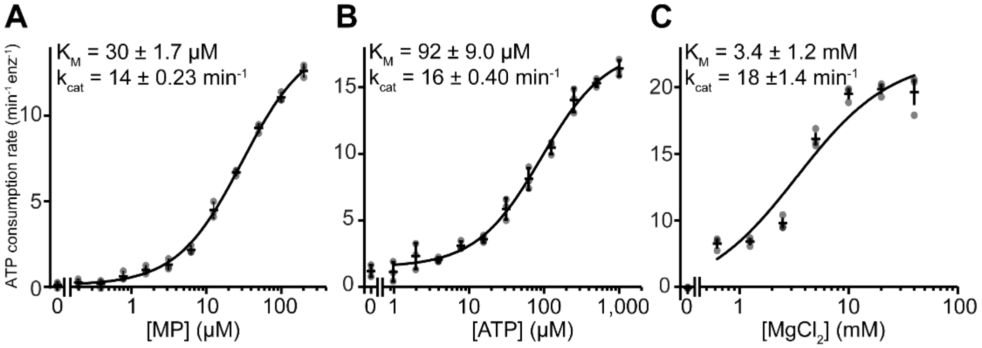

Figure 8. Michaelis-menten curves of PsnB with various substrates. ATPase assays titrating with minimal precursor (A) in solutions containing 0.4 μM PsnB, 100 mM Tris pH 7.3, 50 mM KCl, 5mM ATP, and 10 mM $MgCl_2$ or titrating with ATP (B) in solutions containing 0.4 μM PsnB, 200 μM MP, 100 mM Tris pH 7.3, 50 mM KCl, and 10 mM $MgCl_2$, or titrating with $MgCl_2$ (C) in solutions containing 0.4 μM PsnB, 200 μM MP, 100 mM Tris pH 7.3, 50 mM KCl, and 5 mM ATP. Data are presented as dot plots with mean ± 1 SD (n = 3 independent experiments) and fitted to a hyperbolic equation.

2.2. Characterization of acyl-phosphate intermediate.

Next, to obtain the evidence of the suggested enzyme mechanism (Figure 5), I characterized the acyl-phosphate intermediate of minimal precursor peptide by using hydroxylamine (NH_2OH) to trap the acyl-phosphate (Figure 9A). Hydroxylamine is known as a good nucleophile that readily reacts with acyl-phosphate and has been used to confirm the existence of acyl-phosphate intermediate[60,61]. After adding to the reaction solution 0.5 M NH_2OH, though it severely reduced PsnB activity, two different NH_2OH-trapped peptides (**1-b** and **2-b**) were detected by the MALDI-MS (Figure 9B). Hydroxylamine-adduct peptides were purified by HPLC and further analyzed to confirm their connectivity. MALDI-MS/MS revealed that NH_2OH was added to Glu37 of **1-b** while to Glu38 of **2-b** (Figure 9D). Methanolysis of **2-b** resulted in **2-c** and analyzing **2-c** with MALDI-MS/MS showed that **2-b** contains macrolactone between Thr32 and Glu37 (Figures 9C and D) These results are consistent with the activation of the carboxylate by ATP-grasp enzyme[52] (Figure 5) and with the reaction order of PsnA2—the Thr32-Glu37 inner ring formation before the Thr31-Glu38 outer ring formation[42].

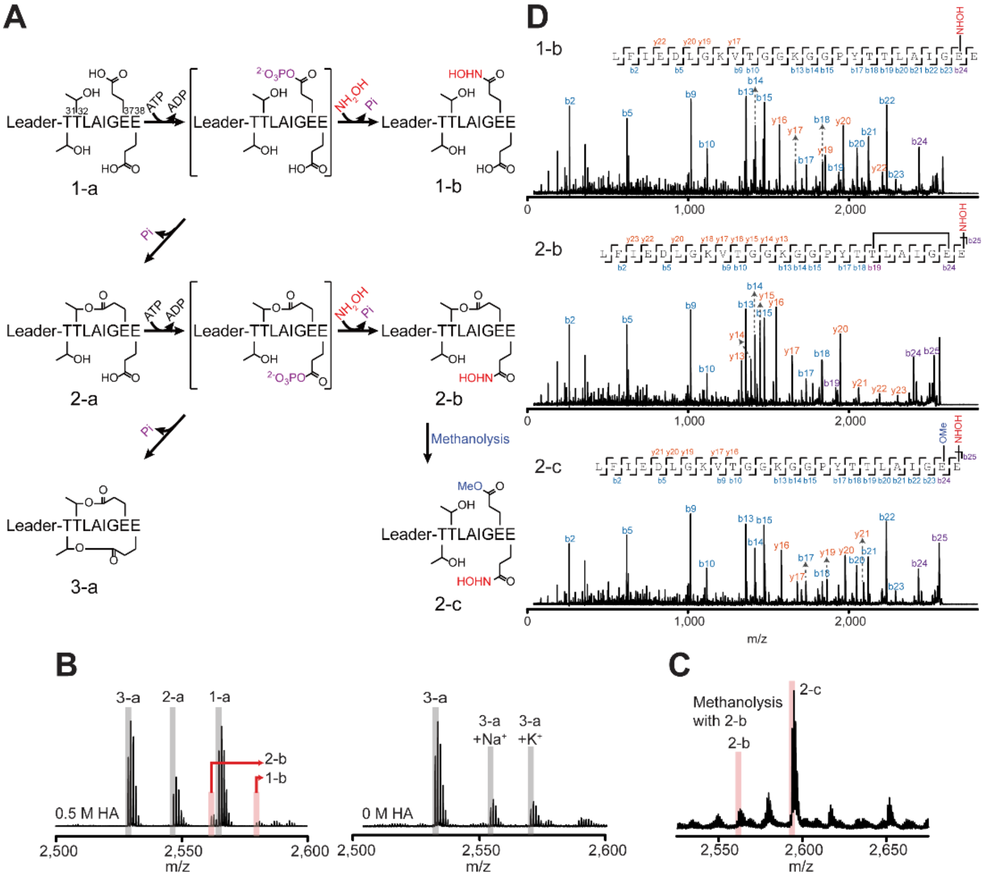A
Leader-TTLAIGEE
1-a
ATP
ADP
NH$_2$OH
Pi
1-b
2-a
2-b
Methanolysis
2-c
3-a
B
3-a
2-a
1-a
2-b
1-b
0.5 M HA
2,500
2,550
2,600
m/z
3-a
3-a +Na⁺
3-a +K⁺
0 M HA
C
Methanolysis with 2-b
2-b
2-c
2,550
2,600
2,650
m/z
D
1-b
2-b
2-c
NHOH
OMe
0
1,000
2,000
m/z

Figure 9. Acyl-phosphate intermediates trapping by hydroxylamine. (A) Scheme of the acyl-phosphate trapping during the macrocyclization reaction. Nucleophilic attack of hydroxylamine rather than the core threonine generates the hydroxylamine adducts of the precursor. (B) MALDI analysis of the reaction solution with (left) or without (right) hydroxylamine. 0.5 M hydroxylamine was added to the reaction mixture containing 100 μM MP (**1-a**) and 6 μM PsnB in buffer A. The reaction mixtures were analyzed by MALDI after 4 hr incubation at 37 ℃. Co-incubation of 0.5 M hydroxylamine generated NH_2OH-added precursor peptides (**1-b** and **2-b**), which are the result of nucleophilic attack of hydroxylamine to acyl-phosphate intermediates. (C) **2-b** was purified by HPLC and methanolysis was performed with purified **2-b** as previously reported[42]. The methanolysis product (**2-c**) was detected by MALDI. (D) MALDI-MS/MS analysis of three hydroxylamine adducts. The connectivities of ester bonds were determined by MS/MS analysis with NH_2OH-added precursor peptides (**1-b** and **2-b**) and methanolysis product (**2-c**).

2.3. Two steps of macrocyclization reaction are highly coupled.

Catalysis of PsnB is divided into two sequential steps—phosphorylation, and ester formation (Figure 5). Previous assays determined the kinetic parameters of each step of PsnB catalysis, ATPase assay for the phosphorylation step, and time-point MALDI analysis for the ester formation step. These two steps seem like happening in a comparable reaction rates (k_{cat} = 12 min^{-1} for phosphorylation, Figure 8A; k_{cat} = 7 –14 min^{-1}, Figure 7A), indicating that two steps of enzyme reaction might be coupled. To confirm whether these reaction steps are highly coupled, I performed a quantitative analysis using HPLC to confirm the efficiency of the macrocyclization reaction of PsnB. At each time-point of PsnB reaction, I measured the amount of ADP generated and the amount of ester bond produced in the precursor peptide (Figure 10). ATP consumption rate was also measured by ATPase assay. The amount of generated ADP was almost identical to that of the ester bond produced, indicating that nucleophilic attack of solvent water is highly prevented and the acyl-phosphate intermediate efficiently undergoes to next step, a nucleophilic attack by the hydroxyl of Thr, which infers that the PsnB reaction would happen in the solvent excluded system.

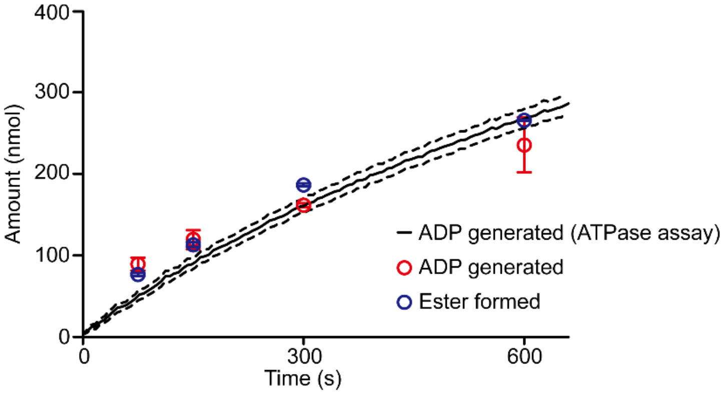

Figure 10. Kinetics of ATP consumption and macrocyclization formation. Amount of consumed ATP and generated ester bond was measured by HPLC (circles) and ATPase assay (line). Data are presented as dot or line plots with mean ± 1 SD (n = 3 independent experiments).

2.4. PsnB is activated by leader peptide binding.

In many RiPP biosynthesis, including graspetide, leader peptide functions as an allosteric effector that activates the enzyme, as well as brings a precursor the affinity to the enzyme[16,24,32,34,62-66]. So, I investigated the role of leader peptide in the behavior of PsnB. Addition of the leader peptide (PsnA2$_{14\text{-}24}$) highly enhanced the affinity between the fluorophore-labeled core peptide (Fl_CP) (Figure 11A). Also, the ATP consumption rate of PsnB was increased about 6.4-fold when saturating amount of leader peptide was added (Figure 11B). These results infer that the binding of leader peptide activates PsnB to enable its substrate binding and to hydrolyze ATP.

Further analyses were performed with the leader-fused PsnB (LP_PsnB), of which the *cis*-leader peptide sequence is attached to the N-terminus of PsnB with a sufficient length of linker. To confirm that the N-terminal cis-leader peptide is stably bound to the linked PsnB, a competitive binding assay with the *in trans* leader peptide was performed. The binding of in trans leader was reduced about 3.2-fold in LP_PsnB than wild-type PsnB due to the cis-leader binding, indicating that the *cis*-leader peptide is stably bound to the PsnB (Figure 11C). The fluorescence anisotropy of Fl_CP with PsnB or LP_PsnB was measured and revealed that the core peptide binds more tightly to the LP_PsnB (K_d = 11 μM) than to the PsnB (K_d > 100 μM; Figure 12A). This enhancement of the enzyme-core peptide interaction by the leader peptide was also observed in HalM2, a class II lanthipeptide synthetase[32]. LP_PsnB also had much higher ATPase activity, which further increased with more amount of core peptide, whereas PsnB had minimal ATPase activity regardless of the core peptide (Figure 12B). As previously reported[7], LP_PsnB, not PsnB alone, successfully modified the core peptide (Figure 12C). Collectively, the binding of the leader peptide promotes the overall process of the enzyme reaction after the leader peptide binding—interaction between PsnB and core peptide, ATP hydrolysis, and also macrolactone formation.

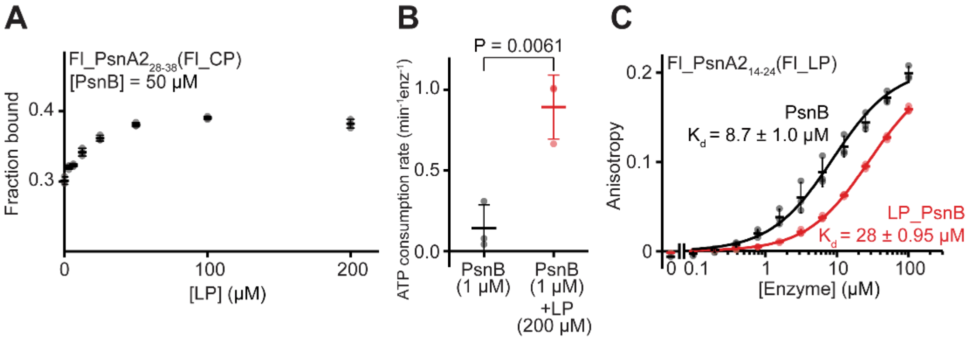

Figure 11. Binding of the leader peptide activates PsnB. (A) Leader peptide (PsnA2$_{14-24}$) enhances the affinity of the core peptide (PsnA2$_{28-38}$) to PsnB. Fraction bound of Fl_CP (0.1 µM) to PsnB (50 µM) was determined by fluorescence anisotropy. (B) LP enhances the ATPase activity of PsnB. Basal ATP consumption rate of PsnB was 0.14 min^{-1}enz^{-1}, whereas the addition of 200 µM LP increased the ATP consumption rate to 0.89 min^{-1}enz^{-1}. P-value < 0.01 by two-sided Student's t-test. (C) Fluorescence anisotropy of Fl_LP (0.1 µM) to wild-type PsnB or leader-fused PsnB (LP_PsnB). Data are presented as dot plots with mean ± 1 SD (n = 3 independent experiments; a-c) and fitted to a hyperbolic equation (C).

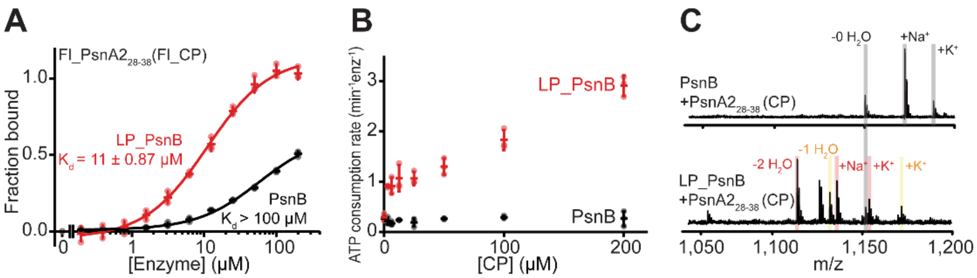

Figure 12. Behavior of leader-fused PsnB. (A) The affinity of the core peptide to PsnB or to the leader-fused PsnB (LP_PsnB) was determined by measuring the fluorescence anisotropy of the fluorophore-labeled CP (Fl_CP; 0.1 μM). (B) The ATPase activity of PsnB or LP_PsnB (2 μM; 37 °C) was measured with different amounts of the core peptide. (C) Macrocyclization of core peptide (200 μM) by PsnB or LP_PsnB (10 μM; 4 h, 37 °C) was monitored by the loss of water in MALDI spectra of reaction solutions. Data are presented as dot plots with mean ± 1 s.d. (n = 3 independent experiments; A, B) and fitted to a hyperbolic equation (A).

2.5. Highly conserved glutamic acid residues of the core peptide enhance PsnB binding.

In many RiPP families, the core peptide has an apparent low affinity to the cognate enzyme[24,32,33]. The affinity assay of the core peptide to the PsnB, however, indicates unexpectedly high affinity between core peptide and PsnB, especially when the enzyme is activated by the leader peptide and I wondered about the characteristics of the interaction between the core peptide and PsnB. To study the effect of the core peptide on the interaction between PsnB and its precursor peptide, I performed fluorescence anisotropy experiments with either Fl_LP or the fluorophore-labeled minimal precursor peptide (Fl_MP). Surprisingly, the minimal precursor peptide showed ~6 times tighter binding to the PsnB than the leader peptide (Figure. 13A), indicating that the core region of PsnA2 also contributes to the interaction between PsnB and precursor peptide. In contrast, the core peptide of MdnA, a precursor of Group1 graspetide, did not enhance the interaction with MdnB or MdnC[24].

To understand the molecular basis of the PsnB–core peptide interaction, I performed Ala scanning for the highly conserved Thr or Glu residues of the core peptide. Affinity of minimal precursor variants to the PsnB was firstly measured and revealed that Ala mutations in Glu, but not in Thr, remarkably reduced the affinity to the PsnB (about 4–10-fold), indicating that the conserved glutamic acid residues are crucial for the core recognition of the PsnB (Figures 13B and 14A). Interestingly, the ATP consumption rate and the modification rate of all these variants were considerably reduced (> 4-fold), although some of these variants still had the ring-forming Thr–Glu side chain pair (Figures 13B, C, and 14B-H). In particular, the T31A or T32A variants that retain two conserved glutamic acid residues also showed much lower ATPase activity than the minimal precursor peptide, suggesting that threonine residue may contribute to the phosphorylation of the acidic residue or the phosphorylation step may not be independent of the subsequent macrocyclization. Collectively, these results indicate that the PsnB binds to the core peptide primarily by recognizing the conserved glutamic acid residues, but the efficient phosphorylation and macrocyclization steps require all the conserved residues of the core peptide, TTxxxxEE.

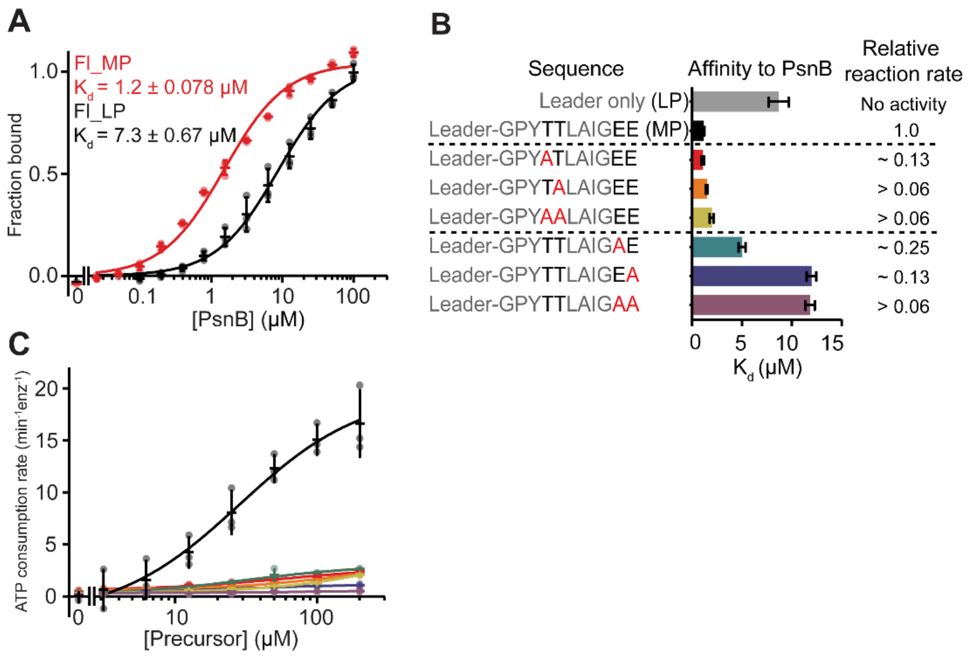

Figure 13. Role of core peptides in enzyme behavior. (A) The affinity of minimal precursor peptide or leader peptide to PsnB was determined by fluorescence anisotropy of fluorophore-labeled MP or LP (0.1 μM). (B) Minimal precursor peptide variants with one or two threonine-to-alanine or glutamate-to-alanine mutations were tested for affinity to PsnB (bar graphs) and macrocyclization reaction (numbers). Affinity was determined as in d, and bar graphs represent the determined K_d and the error of fitting (see **Figure 14** for data and fitting). The relative reaction rates were estimated by using MALDI spectra of the samples taken at different time points (see **Figure 14** for MALDI spectra). (C) ATPase activity of PsnB with different concentrations of the MP variants is shown in (B). Data are presented as dot plots with mean ± 1 s.d. (n = 3 independent experiments; A, C) and fitted to a hyperbolic equation (A, C).

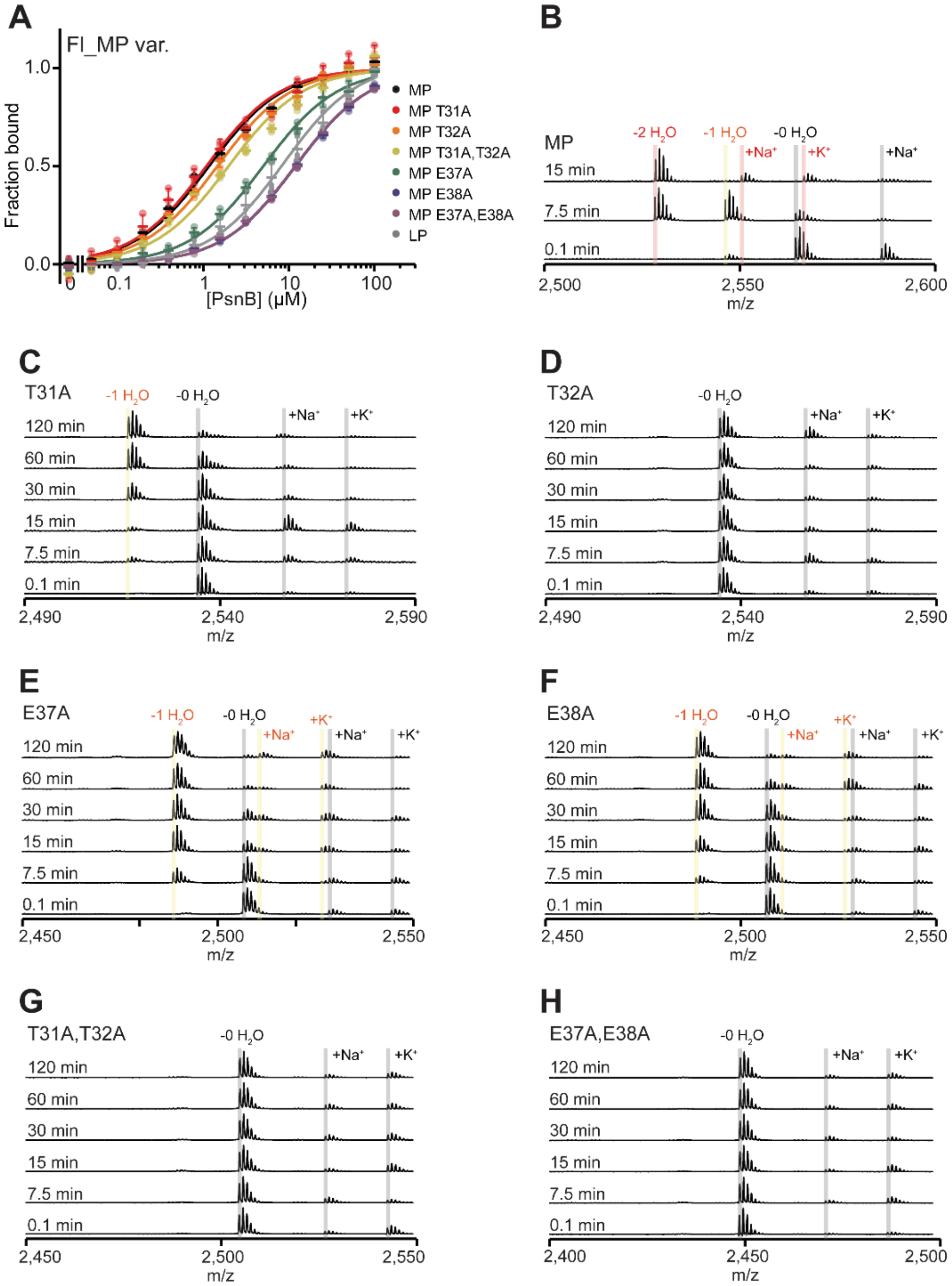
A
FI_MP var.
Fraction bound
1.0
0.5
0.0
0
0.1
1
10
100
[PsnB] (μM)
MP
MP T31A
MP T32A
MP T31A,T32A
MP E37A
MP E38A
MP E37A,E38A
LP
B
MP
-2 H2O
-1 H2O
-0 H2O
+Na+
+K+
+Na+
15 min
7.5 min
0.1 min
2,500
2,550
2,600
m/z
C
T31A
-1 H2O
-0 H2O
+Na+
+K+
120 min
60 min
30 min
15 min
7.5 min
0.1 min
2,490
2,540
2,590
m/z
D
T32A
-0 H2O
+Na+
+K+
120 min
60 min
30 min
15 min
7.5 min
0.1 min
2,490
2,540
2,590
m/z
E
E37A
-1 H2O
-0 H2O
+K+
+Na+
+Na+
+K+
120 min
60 min
30 min
15 min
7.5 min
0.1 min
2,450
2,500
2,550
m/z
F
E38A
-1 H2O
-0 H2O
+K+
+Na+
+Na+
+K+
120 min
60 min
30 min
15 min
7.5 min
0.1 min
2,450
2,500
2,550
m/z
G
T31A,T32A
-0 H2O
+Na+
+K+
120 min
60 min
30 min
15 min
7.5 min
0.1 min
2,450
2,500
2,550
m/z
H
E37A,E38A
-0 H2O
+Na+
+K+
120 min
60 min
30 min
15 min
7.5 min
0.1 min
2,400
2,450
2,500
m/z

Figure 14. Binding and modification property of MP variants. (A) Affinity of Fl_MP variants (0.1 μM) to PsnB was measured by fluorescence anisotropy. Data are presented as dot plots with mean ±1 SD (n = 3 independent experiments) and fitted to a hyperbolic equation. (B to H) Macrolactone formation of MP variants (B; wild-type MP, C; MP T31A, D; MP T32A, E; MP E37A, F; MP E38A, G; MP T31A+T32A, H; MP E37A+E38A) by the PsnB was monitored by MALDI. 1 μM PsnB and 50 μM MP variants were incubated in buffer A at 37°C, and the reaction solutions at designated time points were analyzed by MALDI-MS.

2.6. Binding of ADP or AMPPNP enhances interaction between PsnB and core peptide.

As ATP is another key component for the macrocyclization reaction, I explored the effect of nucleotides on the enzyme–precursor interaction. The fluorescence anisotropy of Fl_MP or Fl_LP with ADP or AMPPNP, a nonhydrolyzable analog of ATP, revealed that ADP and AMPPNP enhance the interaction between PsnB and precursor peptide by 9- and 2-folds, respectively (Figure 15A), but not as much the interaction between PsnB and leader peptide (Figure 15B), suggesting that ADP and AMPPNP strengthen the interaction between PsnB and core peptide. In agreement with this result, saturating amounts of AMPPNP at a single concentration of PsnB (1 µM for Fl_MP and 5 µM for Fl_LP), at which only 30–40% of the peptide binds to PsnB without AMPPNP, increased the bound fraction of Fl_MP, but not of Fl_LP (Figure 15C). These results suggest the binding of nucleotide activates PsnB for the core binding. Collectively, PsnB substrates, including the precursor peptide, both the leader and core peptide, and also a nucleotide reveal the cooperative interaction with the enzyme.

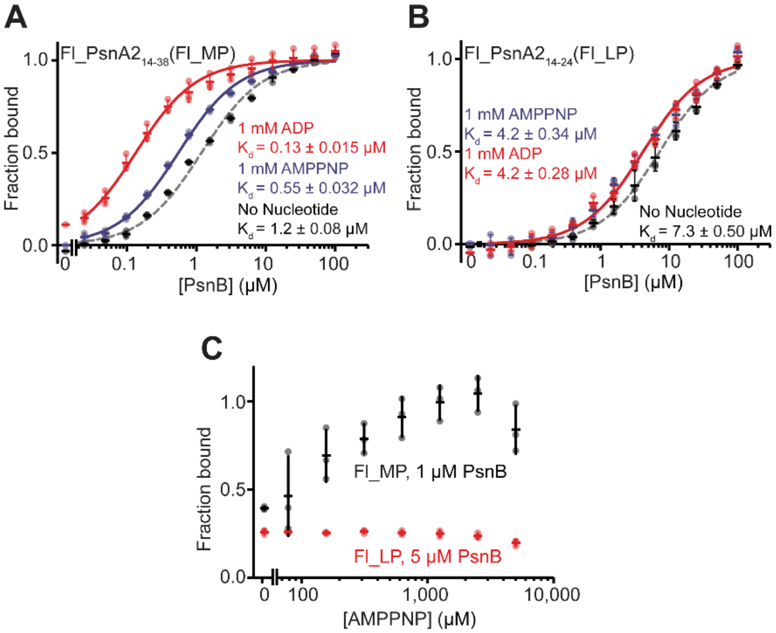

Figure 15. ADP and AMPPNP enhance the affinity of the core peptide to PsnB. (A, B) The affinity of (A) minimal precursor peptide or (B) leader peptide to PsnB in the presence of ADP or AMPPNP (1 mM) was determined by fluorescence anisotropy. (C) The fractions of PsnB-bound Fl_MP or Fl_LP were determined by fluorescence anisotropy with different amounts of AMPPNP. Either 1 μM PsnB or 5 μM PsnB was used for Fl_MP or Fl_LP, respectively, to start with the bound fraction of 0.3–0.4 in the absence of AMPPNP. Data are presented as dot plots with mean ± 1 s.d. (n = 3 independent experiments; A–C) and fitted to a hyperbolic equation (A, B).

2.7. Interaction of PsnB with the ester-containing precursor peptide.

As PsnB introduces two ester bonds to each core motif (TTxxxxEE) of the precursor peptide, a minimal precursor peptide with one ester bond is still a substrate of the enzyme. After two ester bonds are introduced, the reaction product is thought to be released from the enzyme. To investigate the interaction of PsnB with the reaction intermediate or reaction product, the affinity of the precursor peptide with one (MP-1H_2O) or two ester bonds (MP-2H_2O) was checked with or without 1 mM of ADP (Figures 16A and B). MP-1H_2O showed the highest affinity to the enzyme, about 10- or 2.3-fold enhancement compared to MP, with or without ADP respectively. MP-2H_2O bound to the PsnB with a similar affinity to that of the MP. The single-ring intermediate had the highest affinity in both conditions, although its maximal ATPase activity was approximately half that of the minimal precursor peptide (Figure 17C).

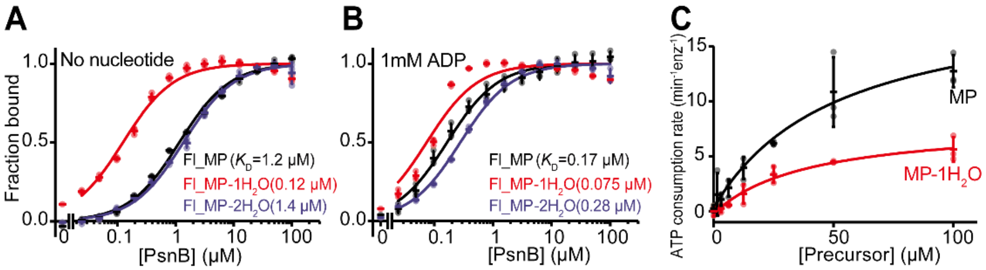

Figure 16. Binding and modification of ring-containing precursors. (A, B) Affinity of ring-containing MPs (MP-1H$_2$O, the single-ring intermediate; MP-2H$_2$O, the double-ring product) to PsnB was determined by fluorescence anisotropy without nucleotide (A) or with 1 mM ADP (B). (C) ATPase activity of PsnB was measured with different concentrations of MP or the single-ring intermediate (MP-1H$_2$O). Data are presented as dot plots with mean ± 1 SD (n = 3 independent experiments; A-C) and fitted to a hyperbolic equation (A-C).

Chapter 3. Structural analysis of PsnB catalysis

3.1. Structures of PsnB complex with minimal precursor peptide and nucleotide.

To understand the molecular basis underlying the interactions of PsnB and its substrates, precursor peptide, and ATP, I crystallized PsnB with a minimal precursor peptide and a nucleotide (Nuc), ADP or AMPPNP. Two structural models of the PsnB-MP-Nuc complex (PDB code: 7DRM for ADP and 7DRN for AMPPNP) and one of the PsnB-MP complex (PDB code: 7DRO) were determined (Table 1 for statistics). The overall structure of PsnB shows a common architecture of ATP-grasp enzymes, including MdnC and CdnC, a Group1 graspetide biosynthetic enzymes, and also non-RiPP ATP-grasp enzymes with known structures—RimK, GshB, LysX, PurT, and DdlB[24,27,50,67-70] (Figure 17). PsnB forms a stable dimer and is made up of typical ATP-grasp ligase domains, domain A, B, and C. A and C domains jointly establish a large central part of the enzyme that houses the substrate binding sites. The cleft between the central A, C domain and B domain displays highly conserved ATP-binding residues that recognize Mg^{2+} ion and nucleotide, ADP or AMPPNP. Like other ATP-grasp ligases of graspetide biosynthesis, domain B binds to a leader peptide. Compared to MdnC and CdnC, PsnB has a distinctively long β6α3 loop region (Arg72–Gln90) and a shorter β9β10 loop (Lys172–Arg181) (Figure 18). β13β14 loop (Asp230–Glu239) faces the outside of PsnB, which is akin to the corresponding helix-loop-helix structure of CdnC[24,27]. Interestingly, from the PsnB-MP-Nuc complex structures, one subunit of PsnB dimer shows the well-resolved nucleotide and the core peptide region as well as the leader peptide while the other monomer lacks substrate binding (Figure 17).

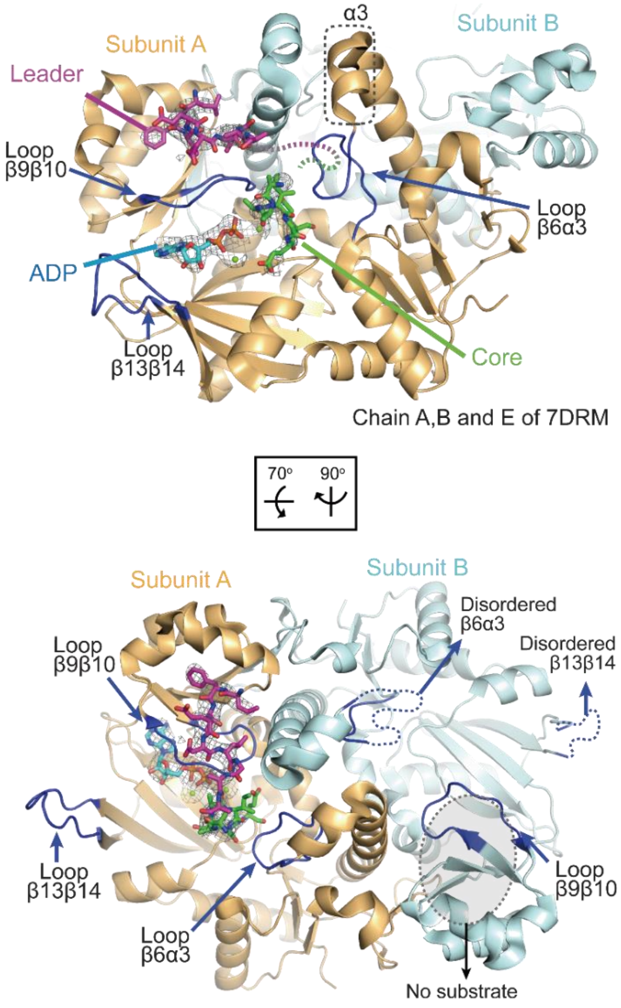

Figure 17. Crystal structure of PsnB complex (7DRM). PsnB (yellow or pale cyan cartoon) is bound with leader peptide (magenta stick), core peptide (green stick), and ADP (cyan stick). Loops β6α3, β9β10 and β13β14 are colored in blue. Folder OMIT maps (gray mesh) for the ADP, leader and core are contoured at 4σ. In subunit B, loops β6α3 and β13β14 are disordered.


β1
α1
β2
α2
β3
β4
β5
β6
α3
72
α3
α4
β7
α5
α6
β8
α7
β9
101
133
171
172
β10
α8
α9
β11
β12
β13
β14
α10
193
181
192
196
203
201
204
211
213
234
233
235
β15
β16
α11
α12
269
282
284
G2
G1
G3
G4
G5
G6
G7
G8
G9
G10
G11
G12
RimK
GshB
LysX
PurT
DdlB
ATP binding
DFR loop
Leader binding
Core binding

]

Figure 18. Sequence alignment of ATP-grasp enzymes. Sequence alignment of PsnB (an enzyme for Group 2 graspetide, G2), representative enzymes for remaining 11 graspetide groups (G1 and G3-G12), and non-RiPP ATP-grasp enzymes (RimK, GshB, LysX, PurT, and DdlB). Secondary structures of PsnB are shown above the alignment. Critical residues for specific interaction are highlighted (ATP binding, cyan; DFR loop, yellow; leader binding, magenta; core binding, green). Strain names and NCBI accession numbers of the representative enzymes for 12 graspetides and non-RiPP ATP-grasp enzymes are as follows: G1, Planktothrix agardhii, WP_042156020.1; G2, Plesiocystis pacifica, WP_006971586.1; G3, Bacillus thuringiensis, WP_000849148.1; G4, Sphingobacteriales bacterium 44-61, OJW02008.1; G5, Vibrio sp. JCM 18905, GAJ78971.1; G6, Chryseobacterium greenlandense, WP_059136627.1; G7, Agrobacterium sp. SUL3, WP_052821370.1; G8, Legionella beliardensis, WP_115303353.1; G9, Actinomadura darangshiensis, WP_132205758.1; G10, Citrobacter sp. wls827, WP_137346417.1; G11, Streptomyces acidiscabies, WP_059044944.1; G12, Nocardia abscessus, WP_043693582.1; RimK, Escherichia coli K-12, P0C0U4.1; GshB, Escherichia coli K-12, P04425.1; LysX, Thermus thermophilus HB8, Q5SH23; PurT, Escherichia coli K-12, P33221; DdlB, Escherichia coli K-12, P07862.

3.2. Phe15 of leader peptide is a key residue for PsnB binding.

Firstly, I investigated the interface between the PsnB and the leader peptide from the obtained structures. In group 1 graspetide biosynthetic enzymes, MdnC and CdnC, enzymes recognize highly conserved residue of cognate leader peptides, PFFARFL and PFFAAFL respectively, by electrostatic or hydrophobic interaction[24,27]. In group 2a graspetide, however, the highly conserved leader peptide sequence motif, LFIEDL, is different from that of group 1 graspetide, which is expected to reveal a distinct interaction scheme. PsnB-leader interface revealed a highly conserved LFIEDL motif of leader peptide binds to the leader-binding domain of PsnB. PsnB showed a hydrophobic interaction between the Phe15 of the leader peptide and the hydrophobic pocket of PsnB which is composed of Tyr171, Ile193, Leu196, Val201, and Phe203. Also, it is revealed that an electrostatic interaction—between Asp18 of leader peptide and Arg181 of PsnB—and a cation-π interaction—between Phe15 of leader peptide and Arg192 of PsnB—from the PsnB-leader peptide interface (Figure 19). These PsnB residues are highly conserved only in the ATP-grasp enzymes for Group 2a graspetide (Figure 20 and 21B), consistent with the divergence of leader sequences among the different groups of graspetides[44]. To confirm their contributions to the leader binding of PsnB, I evaluated the affinity of the leader peptide, ATP consumption activity, and macrocyclization activity of the Ala mutants in these residues; L196A and F203A mutants of PsnB showed 4–5-fold reduced binding affinity and >64-fold reduced ATP consumption and macrocyclization activity, whereas other mutants (Y171A, R181A, R192A, I193A, and V201A) resulted only modestly reduced activities (2–3-fold reduction in binding affinity and intermediate levels of ATP consumption and macrocyclization activity) (Figure 21A-E). The affinity of the leader peptide variants with a mutation—F15A, D18A, or F15(F5)F, a Phe15 mutation to the pentafluorinated Phe15, which can substantially reduce the cation-π interaction50—was also measured. F15A mutant showed the most reduced affinity to the PsnB, about 7.2-fold, while F15(F5)F and D18A revealed 2.6- and 1.5-fold reduced affinity (Figure 22). Collectively, the mutation studies of the PsnB-leader interface indicate that the hydrophobic interaction between Phe15 of the leader peptide and the hydrophobic pocket of the PsnB is most critical in the enzyme-leader binding and that the cation-π and electrostatic interactions contribute only modestly.

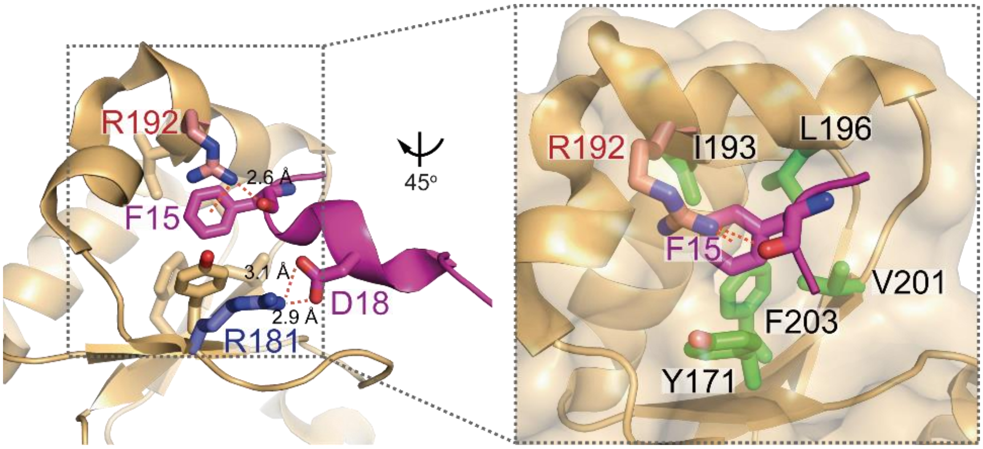

Figure 19. Molecular interactions between PsnB and leader peptide. Interaction scheme of leader peptide (magenta sticks/cartoon) and PsnB (yellow cartoon). Chains A and E of 7DRM. Five hydrophobic residues of PsnB (green sticks) form a hydrophobic pocket for the Phe15 of leader peptide. Arg192 (red sticks) of PsnB interacts with Phe15 by hydrogen bond and cation-π interaction. Arg181 (blue sticks) of PsnB shows auxiliary electrostatic interaction with Asp18 of leader peptide.

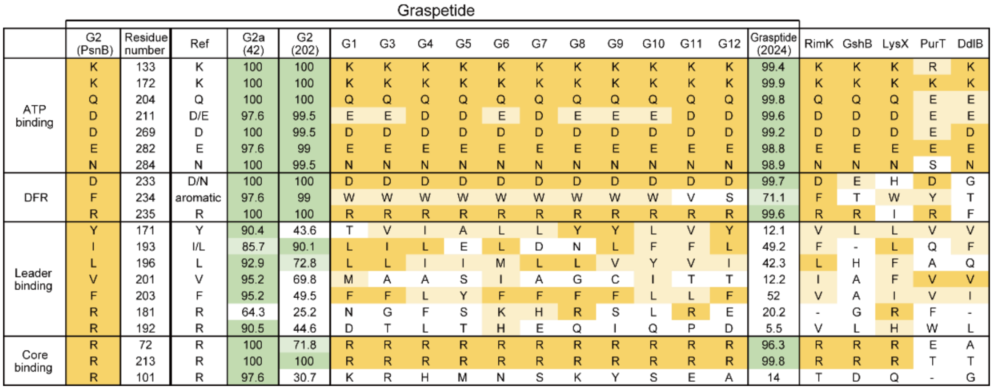

	Graspetide																					
	G2 (PsnB)	Residue number	Ref	G2a (42)	G2 (202)	G1	G3	G4	G5	G6	G7	G8	G9	G10	G11	G12	Grasptide (2024)	RimK	GshB	LysX	PurT	DdlB
ATP binding	K	133	K	100	100	K	K	K	K	K	K	K	K	K	K	K	99.4	K	K	K	R	K
	K	172	K	100	100	K	K	K	K	K	K	K	K	K	K	K	99.9	K	K	K	K	K
	Q	204	Q	100	100	Q	Q	Q	Q	Q	Q	Q	Q	Q	Q	Q	99.8	Q	Q	Q	E	E
	D	211	D/E	97.6	99.5	E	E	D	D	E	D	E	E	E	D	D	99.6	D	D	D	E	E
	D	269	D	100	99.5	D	D	D	D	D	D	D	D	D	D	D	99.2	D	D	D	E	D
	E	282	E	97.6	99	E	E	E	E	E	E	E	E	E	E	E	98.8	E	E	E	E	E
	N	284	N	100	99.5	N	N	N	N	N	N	N	N	N	N	N	98.9	N	N	N	S	N
DFR	D	233	D/N	100	100	D	D	D	D	D	D	D	D	D	D	D	99.7	D	E	H	D	G
	F	234	aromatic	97.6	99	W	W	W	W	W	W	W	W	W	V	S	71.1	F	T	W	Y	T
	R	235	R	100	100	R	R	R	R	R	R	R	R	R	R	R	99.6	R	R	I	R	F
Leader binding	Y	171	Y	90.4	43.6	T	V	I	A	L	L	Y	Y	L	V	Y	12.1	V	L	L	V	V
	I	193	I/L	85.7	90.1	L	I	L	E	L	D	N	L	F	F	L	49.2	F	-	L	Q	F
	L	196	L	92.9	72.8	L	L	I	I	M	L	L	V	Y	V	I	42.3	L	H	F	A	Q
	V	201	V	95.2	69.8	M	A	A	S	I	A	G	C	I	T	T	12.2	I	A	F	V	V
	F	203	F	95.2	49.5	F	F	L	Y	F	F	F	F	L	L	F	52	V	A	I	V	I
	R	181	R	64.3	25.2	N	G	F	S	K	H	R	S	L	R	E	20.2	-	G	R	F	-
	R	192	R	90.5	44.6	D	T	L	T	H	E	Q	I	Q	P	D	5.5	V	L	H	W	L
Core binding	R	72	R	100	71.8	R	R	R	R	R	R	R	R	R	R	R	96.3	R	R	R	E	A
	R	213	R	100	100	R	R	R	R	R	R	R	R	R	R	R	99.8	R	R	R	T	T
	R	101	R	97.6	30.7	K	R	H	M	N	S	K	Y	S	E	A	14	T	D	Q	-	G

Figure 20. Conservation pattern of critical residues. Yellow and light yellow indicate identical and synonymous residues, respectively. Conservation % in Group 2a or 2 graspetides or in all graspetides are also shown with the number of members in each group (70–90% conservation, light green; 90–100%, green).

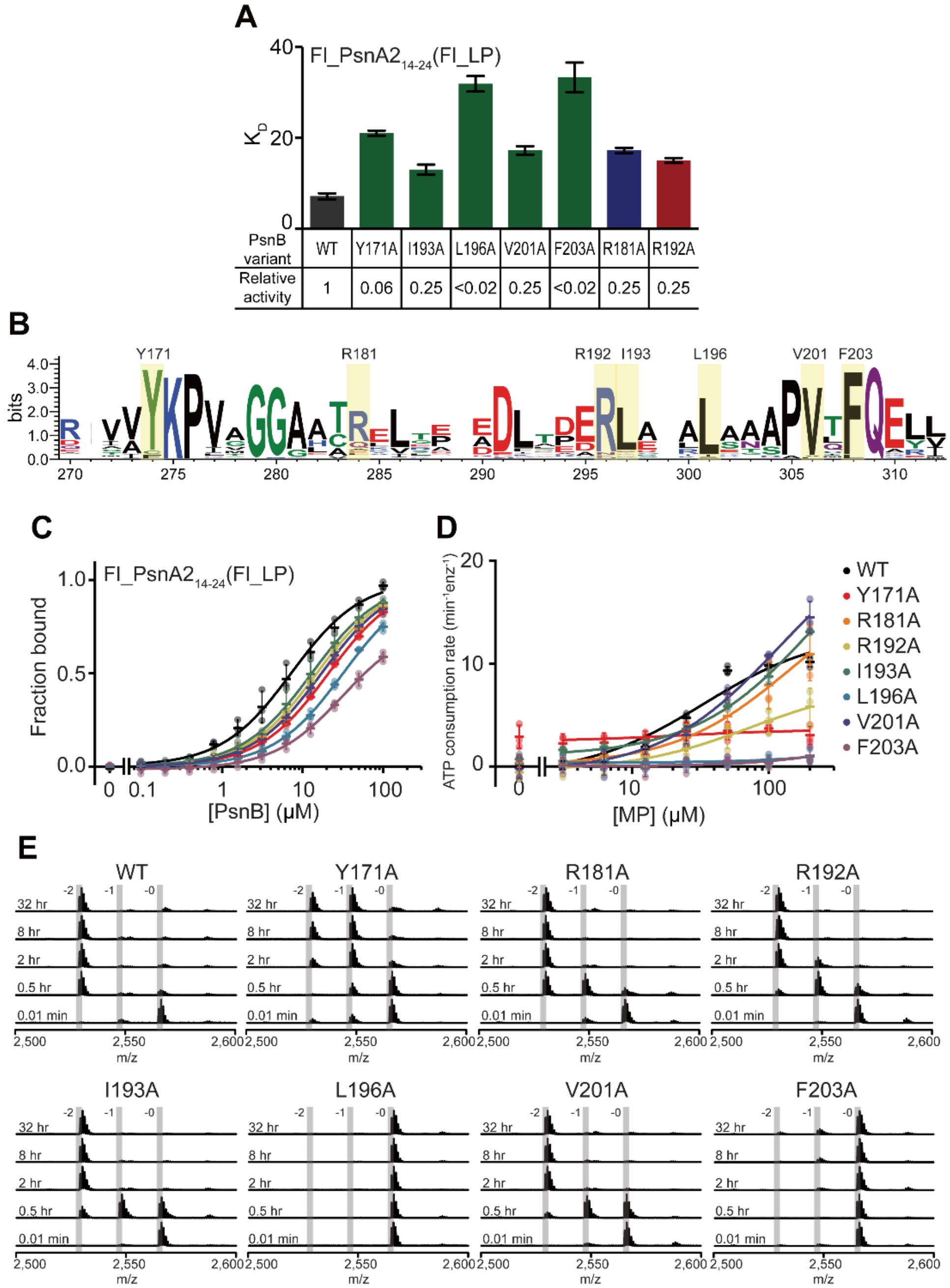

PsnB variant	WT	Y171A	I193A	L196A	V201A	F203A	R181A	R192A
Relative activity	1	0.06	0.25	<0.02	0.25	<0.02	0.25	0.25

Figure 21. Characterization of leader-binding site mutants of PsnB. (A) The affinity to LP (bar graphs) and enzymatic activity (number) of leader-binding site mutants. (B) Sequence logo of the leader binding domain in Group 2a graspetide biosynthetic enzymes. Most residues interacting with leader peptides are highly conserved (yellow boxes). (C, D) Fluorescence anisotropy of Fl_LP (0.1 μM; C) and ATP consumption rate (D) were measured with PsnB mutants. L196A and F203A were most deleterious. Data are presented as dot plots with mean ±1 SD (n = 3 independent experiments) and fitted to a hyperbolic equation (C, D). (E), MALDI-spectra of reactions of the leader-binding site mutants (0.5 μM) with MP (50 μM).

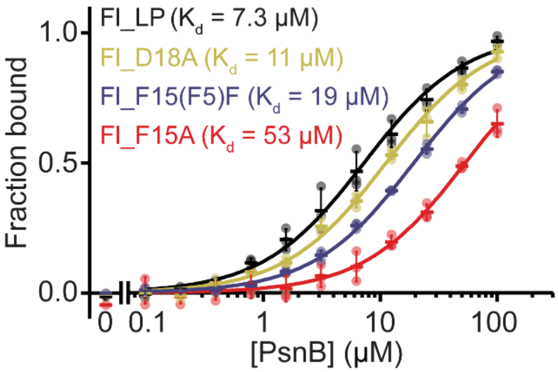

Figure 22. Binding of leader peptide variants. Fluorescence anisotropy of LP variants (0.1 μM) was measured to determine their PsnB affinity. Data are presented as dot plots with mean ±1 SD (n = 3 independent experiments) and fitted to a hyperbolic equation.

3.3. Arg213 of PsnB recognizes reaction-participating glutamic acid of core peptide.

Interface between PsnB and core peptide revealed distinct electrostatic interactions—between Arg213, Arg101 of the PsnB and Glu37, Glu38 of the core peptide respectively—and also a hydrogen-bond interaction between Arg72 of PsnB and Gly36 of the core peptide (Fig. 23). Interestingly, Arg213 of PsnB interacts with the carboxyl side-chain of Glu37 of core peptide, which is the first residue to be phosphorylated by the enzyme reaction. This interaction locates the Glu37 near the gamma-phosphate of AMPPNP (5.2 Å), which seems to be critical for enzyme catalysis. To confirm the importance of Arg101 and Arg213 of PsnB in enzyme catalysis, Ala mutants of PsnB were prepared (It was unable to prepare PsnB R72A due to the expression issue) and the activity was checked by measuring the ATP consumption and macrocyclization activity. PsnB R213A exhibits more than 100-fold reduced activity while Arg101 is largely dispensable for ATP consumption and macrocyclization activity. (Figures 24A and B). Also, I prepared leader-fused PsnB mutants of these residues and found that all three residues, Arg72, Arg101, and Arg213, are required to tight binding of the core peptide (Figure 24C). Arg72 and Arg213 are highly conserved in all of the graspetide biosynthetic enzymes while Arg101 is conserved only in group 2a (Figure 20), as the conservation pattern of core peptides are distinct from each group, of which enzymes would possess separately conserved residues that recognize core peptide. Collectively, although every three Arg residues that bind to the core peptide are important for the tight binding, only

Arg213 that binds to reaction-participating glutamic acid of the core peptide is a key residue for enzyme activity.

Interestingly, similar interaction pattern of Arg213-Glu37 is also shown in the CdnC-core peptide interface, in which the corresponding arginine (Arg217) of CdnC recognizes the reaction-participating acid residue[27]. Together with the 100% conservation rate of Arg213 in all graspetide biosynthetic enzymes, the interaction pattern between Arg213 of PsnB and Glu37 of core peptide, a reaction-participating acidic residue, would be highly conserved in all groups of graspetide, which is the key step that initializes the graspetide biosynthesis.

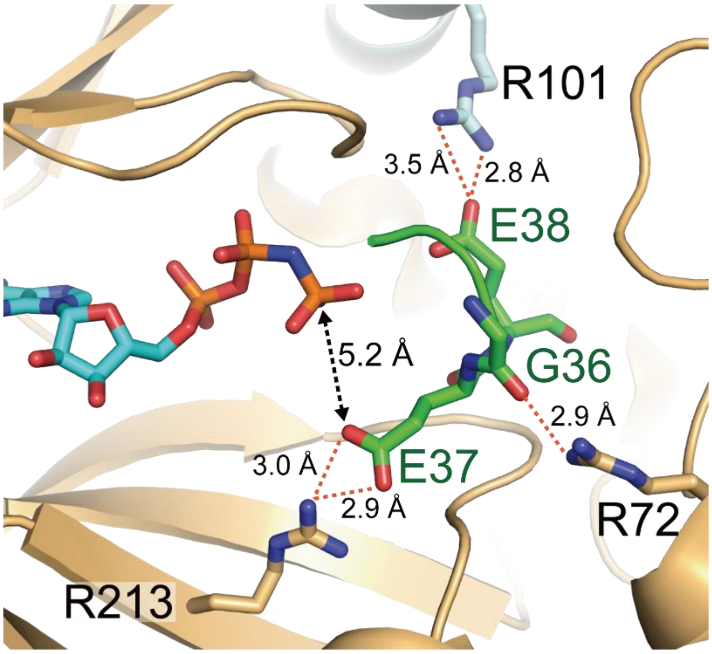

Figure 23. Interaction scheme of core peptide and PsnB (7DRN). Glu37 and Glu38 of core peptide (green sticks/cartoon) interact with Arg213 of PsnB (yellow sticks/cartoon) and Arg101 from the neighboring subunit (cyan sticks/cartoon), respectively. The backbone amide of Gly36 of the core peptide interacts with Arg72 of PsnB. The carboxylate oxygen of Glu37, which forms the first ring, is located only 5.2 Å away from the γ-phosphate of AMPPNP.

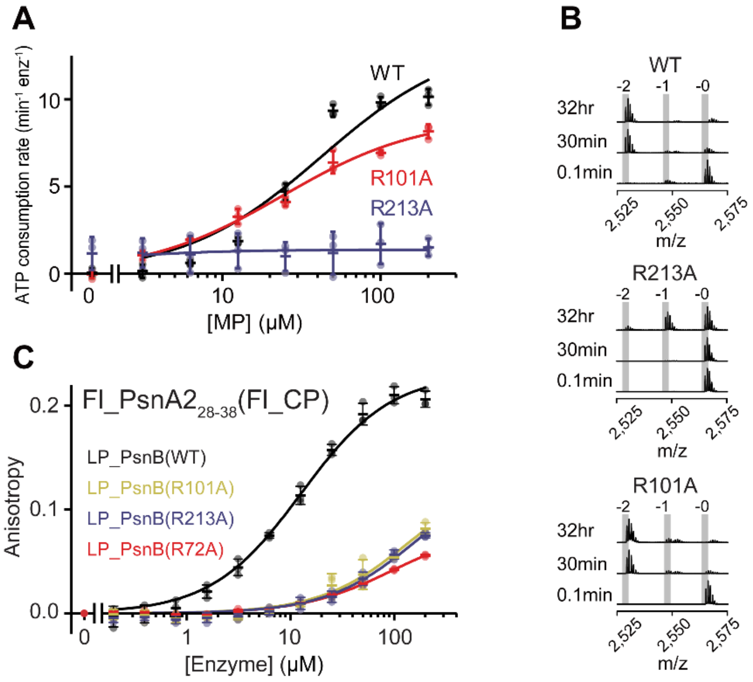

Figure 24. Activity of core-binding site mutants of PsnB. (A, B) ATPase activity (A) and macrocyclization reaction (B) of the wild-type PsnB, R101A mutant, or R213A mutant. (C) Fluorescence anisotropy of Fl_CP (0.1 μM) with leader-fused PsnB mutants. Mutation of core-binding residues reduced the affinity between CP and the enzyme. Data are presented as dot plots with mean ± 1 SD (n = 3 independent experiments) and fitted to a hyperbolic equation (A and C).

3.4. Key residues of PsnB that recognize ATP.

PsnB possesses highly conserved ATP-binding residues which are a common features of the ATP-grasp enzymes (Figure 20). Gln204 recognizes the base region of AMPPNP; Asp211 binds to the sugar of AMPPNP; Lys133, Lys172, and Mg^{2+} interact with α-phosphate; α- and β-phosphate also coordinate with two Mg^{2+} ions which are fastened by Asp269, Glu282, and Gln284 (Figure 25). The interaction scheme between PsnB and ADP is shared with various ATP-grasp enzymes[52] and participating residues are highly conserved in graspetide biosynthetic ATP-grasp ligases.

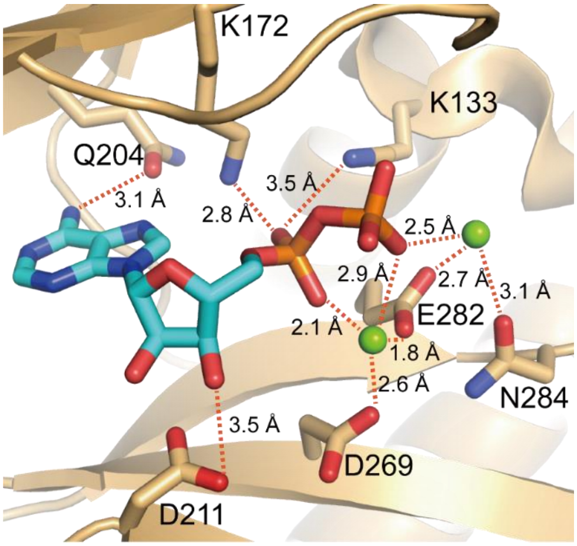

ADP from chain A, PsnB-MP-ADP (7DRM)

Figure 25. Interaction scheme of ADP and PsnB (7DRM). Gln204 of PsnB (yellow sticks/cartoon) recognizes the base of ADP (cyan sticks), Asp211 interacts with sugar of ADP, and Lys133, Lys172, Asp269, Glu282, and Asn284 of PsnB bind to a phosphate of ADP and Mg^{2+}.

3.5. Asymmetry of substrate binding in PsnB dimer.

All of the PsnB dimers resolved at PsnB-MP-Nuc complexes and two of three PsnB dimers at PsnB-MP show asymmetric substrate binding in each monomer (Figure 17 and 26). In PsnB-MP-Nuc complex, monomer A binds to both leader and core region of minimal precursor and also a nucleotide while monomer B lacks the substrates. Likewise, only monomer A interacts with the leader peptide in PsnB-MP complex. To examine whether PsnB also exhibits asymmetric substrate binding in solution condition, I checked the stoichiometry of the precursor binding in PsnB dimer by measuring the fraction of Fl_MP that binds to the PsnB with increasing amounts of unlabeled minimal precursor peptide that competes with Fl_MP in the presence of saturating amount of PsnB (10 µM) and ADP (1 mM) (Figure 27). Two simulations of two opposite models were also performed, the precursor-enzyme stoichiometry to 1:2 binding (complete asymmetry model) and 2:2 binding (complete symmetry model). In asymmetric binding model, only one PsnB subunit of dimer can bind to the minimal precursor with K_d of 0.13 µM while in symmetric binding model, each monomer independently binds to the minimal precursor with the same K_d. The competitive binding assay firstly follows the asymmetric binding model but it converged to the symmetric binding model as the amount of unlabeled minimal precursor peptide increased. This result can be analyzed by an intermediate model in which the two subunits of the PsnB dimer can bind to the minimal precursor with different affinities, which can be explained by the negative cooperativity of the enzyme-ligand interaction. Indeed, the data in Figure 10A fit much better to the Hill curves with Hill coefficients of 0.75 and 0.79 for minimal precursor and leader peptide, respectively (Figure 28). Similar to this, the structure of CdnC also reveals asymmetric substrate binding that only one monomer of CdnC dimer shows well-conserved core peptide[27].

A

PDB code (resolution)	Complex	State	Assembly	PsnB chain	Precursor chain	Nucleotide	Cα RMSD (# of Cα)	Loop β6α3	Loop β13β14	Resolved region of precursor
7DRM (3.28 Å)	PsnB PsnA2$_{14-38}$ ADP	ENLC-E	ABE	A	E	ADP	1.556 (293)	O	O	14-22(LP)/33-38(CP)
				B	-	-		X	X	-
			CDF	C	F	ADP	1.378 (292)	O	O	14-22(LP)/32-38(CP)
				D	-	-		X	X	-
7DRN (3.56 Å)	PsnB PsnA2$_{14-38}$ AMPPNP		ABE	A	E	AMPPNP	1.458 (292)	O	O	14-22(LP)/31-38(CP)
				B	-	-		X	X	-
			CDF	C	F	AMPPNP	1.395 (292)	O	O	14-22(LP)/31-38(CP)
				D	-	-		X	X	-
7DRP (2.98 Å)	PsnB PsnA2$_{14-38}$ (pE37) ADP	ENLC-EN	ABE	A	E	ADP	1.484 (294)	O	O	14-21(LP)/32-38(CP)
				B	-	ADP		X	X	-
			CDF	C	F	ADP	1.338 (291)	O	O	14-21(LP)/29-38(CP)
				D	-	ADP		X	X	-
7DRO (3.25 Å)	PsnB PsnA2$_{14-38}$	EL-EL	ABGH	A	G	-	0.541 (297)	X	O	14-19(LP)
				B	H	-		X	O	14-19(LP)
		EL-E	CDI	C	I	-	0.803 (283)	X	O	14-19(LP)
				D	-	-		X	X	-
			EFJ	E	J	-	0.888 (280)	X	O	14-19(LP)
				F	-	-		X	X	-

B

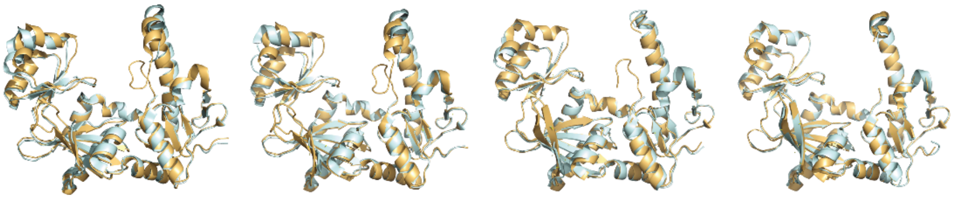

Overlap of
Chain A and B in 7DRM
RMSD = 1.556 Å
for Cα number of 293
(ENLC-E)

Overlap of
Chain A and B in 7DRP
RMSD = 1.484 Å
for Cα number of 294
(ENLC-EN)

Overlap of
Chain C and D in 7DRO
RMSD = 0.803 Å
for Cα number of 283
(EL-E)

Overlap of
Chain A and B in 7DRO
RMSD = 0.541 Å
for Cα number of 297
(EL-EL)

Figure 26. Four crystal structures of PsnB complexes. (A) Basic information for four crystal structures of PsnB complexes. 7DRM, 7DRN, and 7DRP contain two PsnB dimers in the asymmetric unit, whereas 7DRO has three PsnB dimers. Total of nine independent dimers were classified into four states based on the components of the dimer. Four states of PsnB dimers show a different levels of asymmetry between two monomers and different loop stability (O: resolved, X: not resolved). (B) Two superposed PsnB subunits in the dimers (yellow and light blue cartoons). Root-mean-square deviations (RMSDs) of Cα atoms are shown below.

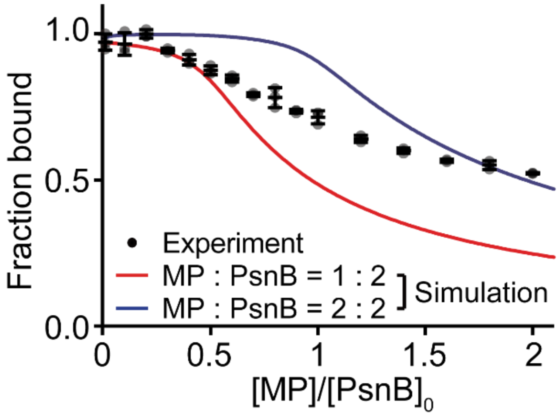

Figure 27. Stoichiometric binding of PsnB dimer. PsnB-bound MP fractions were measured by fluorescence anisotropy of the fluorophore-labeled MP (0.1 μM) with PsnB (10 μM) and increasing amounts of unlabeled MP. Data are presented as dot plots with a mean ± 1 s.d. (n = 3 independent experiments). The simulation curves of two models, in which the MP:PsnB stoichiometry is either 1:2 or 2:2, are shown as red and blue solid lines, respectively.

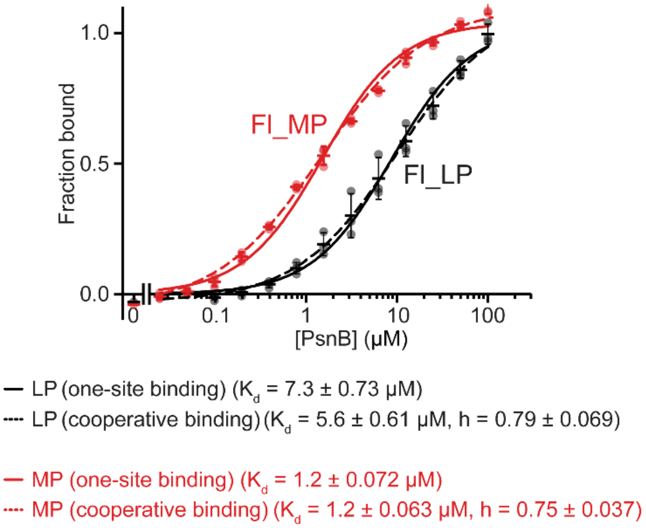

Figure 28. Negative cooperativity of MP and LP binding. Data in **Figure 13A** are fitted to two different equations: a normal hyperbolic equation ($y = [PsnB]/(K_d + [PsnB])$; solid lines) and a Hill equation ($y = [PsnB]^h /(K_d^h + [PsnB]^h)$; dashed lines). Data points below the inflection point, at which the fraction bound is 0.5, are mostly above the hyperbolic fitting curve, but those above the inflection point are mostly below the hyperbolic fitting curve. This pattern suggests the negative cooperativity in the protein-ligand interaction. The Hill curves show much better fitting, as shown that most data points are very close to the fitting curves. Indeed, the fitting to the Hill equation resulted in the Hill coefficients of 0.75 and 0.79 for Fl_MP and Fl_LP, respectively, demonstrating the negative cooperativity of the interactions. Data are presented as dot plots with mean ± 1 SD (n = 3 independent experiments).

3.6. Substrate binding induces a conformational change of PsnB.

By comparing nine different PsnB dimers from the four structural models of PsnB complex (PsnB-MP-ADP (7DRM), PsnB-MP-AMPPNP (7DRN), PsnB-MP (7DRO), and PsnB-MP(pE37)-ADP (7DRP); PsnB-MP(pE37)-ADP is a PsnB complex structure that possesses phospho-peptide mimic and will be minutely described in **3.8**), I classified these PsnB dimers into four different states based on their binding partners (Figure 29). In ENLC-E (E, enzyme; N, nucleotide; L, leader; C, core) and ENLC-EN, one PsnB monomer is a full enzyme-nucleotide-leader-core complex (ENLC) while the other monomer lacks the substrates (E) or interacts with ADP (EN). In EL-EL and EL-E, PsnB monomer has one leader peptide (EL) or nothing (E). From each of PsnB dimers, the asymmetry in the conformation of PsnB was evaluated by calculating the RMSD of the C(α) atoms of monomers A and B, which combine to each other (Figure 26). ENLC-E and ENLC-EN show the most asymmetric states (RMSD > 1 Å), while EL-E reveals only weak asymmetry (RMSD ~ 1 Å) and almost no asymmetry for EL-EL (RMSD = 0.54 Å). The β13β14 loop is shown only in the leader-bound PsnB, and the β6α3 loop is visible only in the core-bound PsnB subunit. Although ADP and leader peptides are sometimes found in both monomers of PsnB, the core peptide is found only in one monomer, inferring that the binding of the core peptide, rather than of the leader peptide or nucleotide, requires (and induces) the increased level of asymmetry in PsnB dimer.

A comparison of different PsnB monomer structures revealed conformational changes in PsnB upon binding of the precursor or a nucleotide

(Figure 30A). Leader peptide binding moves the α3α4 helices of the leader binding domain toward the dimeric center by 2.6 Å, generating a hydrophobic pocket to accommodate Phe15 in the leader peptide, and relocates Arg195 out of the entry of the hydrophobic pocket (Figure 30B). Binding of the nucleotide moves the β9β10 loop toward the nucleotide by 2.3 Å via interaction with Lys172 and Thr180 (Figure 30C). The binding of both leader peptide and core peptide shifts the α3α4 helices toward the active site by 2.4 Å (Figure 30A and D). The α3α4 helices extensively interact with the same helices in the neighboring PsnB monomer, and therefore, the movement of the rigid body of the two α3α4 pairs appears to induce dimeric asymmetry (Figure 30D and E). The β6α3 loop becomes ordered only after the core peptide binds to PsnB and tightly packs the active site (Figure 30F). Collectively, the overall conformational change of PsnB upon the precursor peptide and nucleotide binding establishes the space for the core peptide and makes the active site compact.

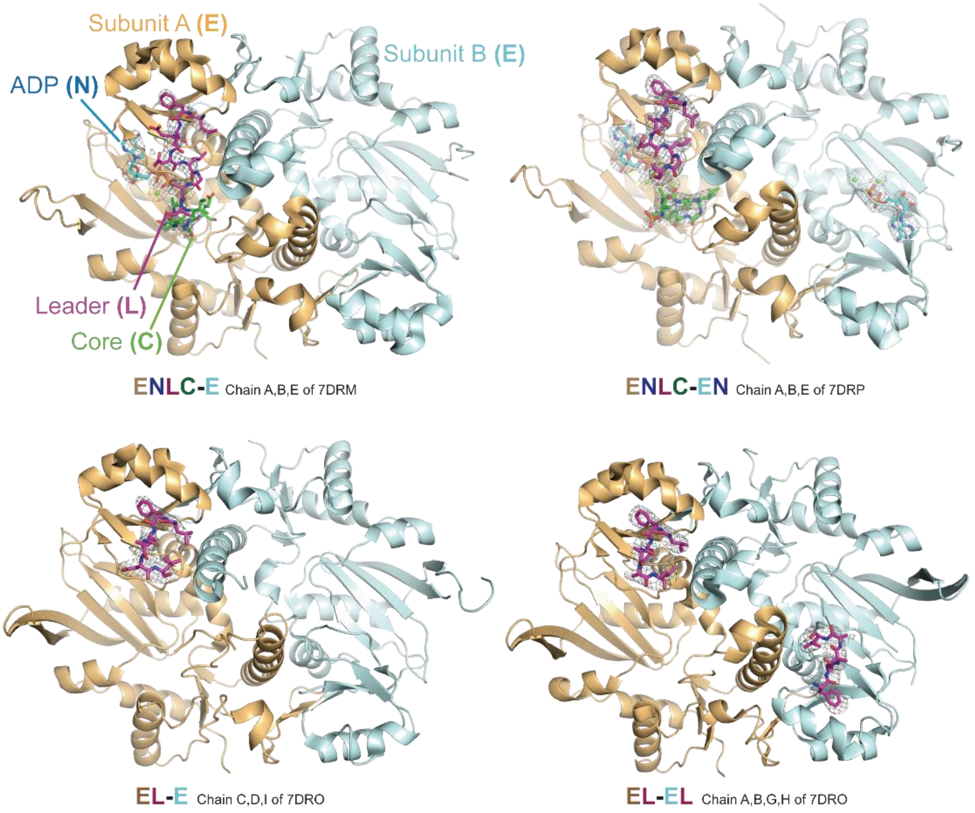

ENLC-E Chain A,B,E of 7DRM

ENLC-EN Chain A,B,E of 7DRP

EL-E Chain C,D,I of 7DRO

EL-EL Chain A,B,G,H of 7DRO

Figure 29. Four PsnB structures with different binding modes. Structure of four different states of PsnB dimers (E, enzyme, yellow or pale cyan cartoon; N, nucleotide, cyan sticks; L, leader, magenta sticks; C, core, green sticks). Polder OMIT map (gray mesh) of each peptide or nucleotide is contoured at 4.0 σ.

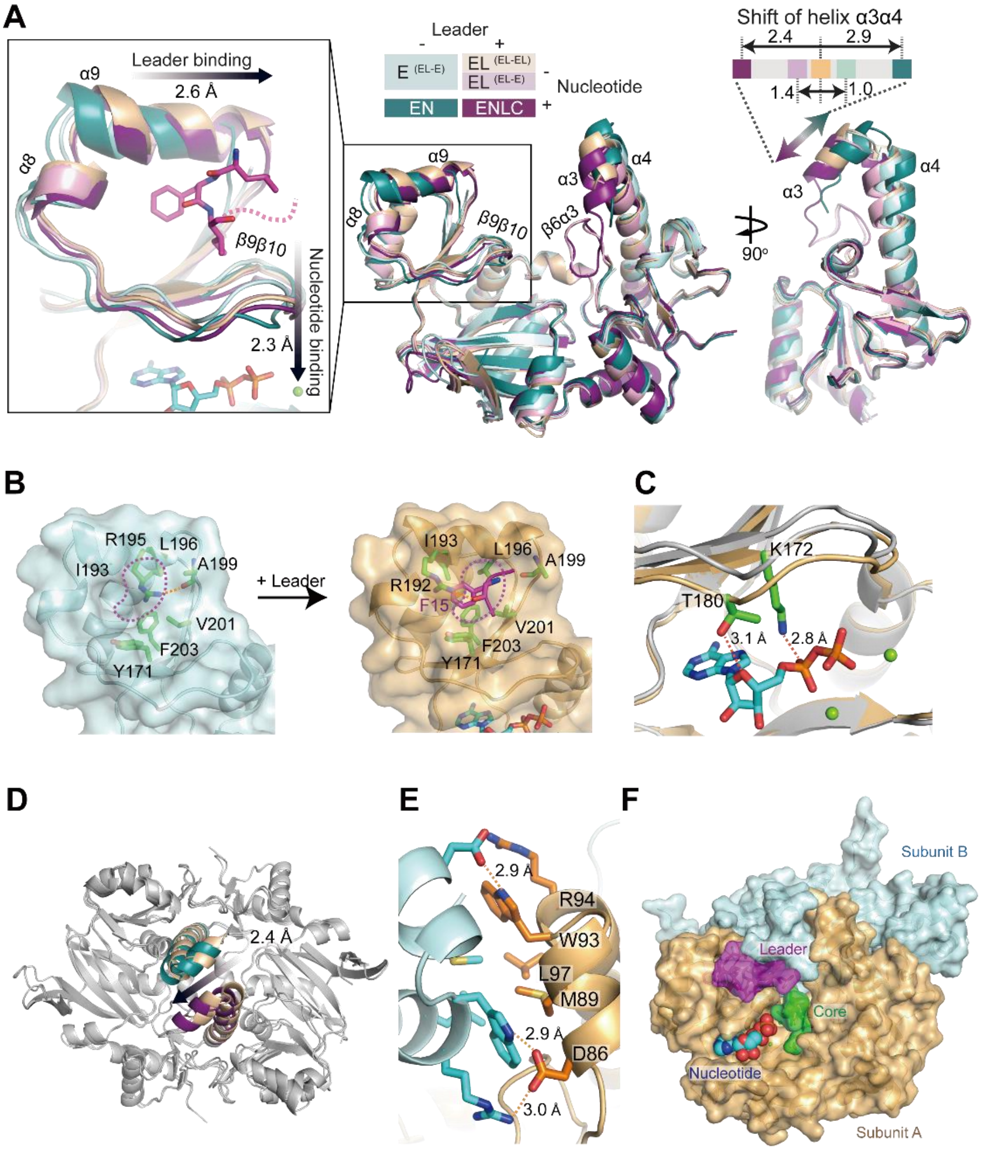
A
Leader binding
2.6 Å
α9
α8
β9β10
2.3 Å
Nucleotide binding
Leader
-
+
E (EL-E)
EL (EL-EL)
EL (EL-E)
-
Nucleotide
EN
ENLC
+
α9
α8
β9β10
β6α3
α3
α4
90°
Shift of helix α3α4
2.4
2.9
1.4
1.0
α3
α4
B
R195
L196
I193
A199
V201
F203
Y171
+ Leader
I193
L196
A199
R192
F15
V201
F203
Y171
C
K172
T180
3.1 Å
2.8 Å
D
2.4 Å
E
2.9 Å
R94
W93
L97
M89
2.9 Å
D86
3.0 Å
F
Subunit B
Leader
Core
Nucleotide
Subunit A

Figure 30. Conformational change of PsnB dimer during the substrate binding. (A) Superposition of five PsnB subunits (E, empty PsnB, pale cyan; EN, enzyme–nucleotide complex, teal; EL, enzyme–leader complex, pink (from EL–E dimer) or orange (from EL–EL dimer); ENLC, enzyme–nucleotide–leader–core holo-complex, magenta). Leader binding moves the α8α9 helices by 2.6 Å, nucleotide binding shifts the β9β10 loop by 2.3 Å and core binding attracts the α3α4 helices by 2.4 Å. The β6α3 loop is ordered only when the CP is bound to PsnB. (B) Surface models of the leader-binding domain without (left) or with (right) the bound Phe15 in the LP (magenta sticks). The hydrophobic pocket for Phe15 is shown as magenta dashed lines. (C) The nucleotide (cyan sticks) binding shifts the β9β10 loop (from gray to yellow cartoon). Lys172 and Thr180 that interact with a nucleotide are shown as green sticks. (D) Conformational change in PsnB in the dimeric context. Two pairs of α3α4 helices in the PsnB dimer move together during the 2.4-Å shift from symmetric dimer (EL from EL–EL; orange) to asymmetric dimer (ENLC and E; magenta and teal, respectively). (E) Two α3α4 pairs of a PsnB dimer show extensive interactions with each other to form a rigid body. Two PsnB subunits are shown as yellow and pale cyan cartoons, and their interacting residues are presented as orange and cyan sticks, respectively. (F) Surface model of the ENLC-E complex (yellow and pale cyan for two PsnB subunits). The binding of LP (magenta) and nucleotide (cyan spheres) induces the conformational change of PsnB dimer to generate a compact core (green) binding site.

3.7. Arg235 residues of PsnB recognizes the intramolecular ATP molecule by β- and γ-phosphate binding.

Although the obtained PsnB complex structures show that a dimer is a fundamental unit, distinct inter-dimeric interaction was found in the PsnB structures that contain leader peptides (ENLC and EL). In PsnB of ENLC state, the β13β14 loop in one monomer (A*), including the $DFR_{233-235}$ residues, interacts with the β9β10 loop and a nucleotide in the neighboring monomer (A) (Figure 31A). Meanwhile, if no nucleotide is present (EL), the β13β14 loop in one monomer (A*) occupies the nucleotide-binding site of the opponent PsnB monomer (A) (Figure 31B). In particular, Asp233 forms hydrogen bonds with a nitrogen of Arg235, Phe234 makes hydrophobic contacts with Ile227/Ile241/Phe292, and Arg235 interacts with the phosphate of the nucleotide. To test whether this inter-dimeric interaction also happens in solution, which leads to the formation of a higher oligomer, I performed size-exclusion chromatography and fluorescence resonance energy transfer (FRET). There was no evidence for stable higher oligomer formation in solution during the addition of ATP or coincident addition of the minimal precursor and AMPPNP though (Figure 32A-H). These results suggest that the β13β14 loop forms putative intramolecular interactions, rather than the PsnB dimers forming a higher oligomer. The intramolecular interaction is found in the corresponding loop region of other ATP-grasp enzymes[27,50,71]. Loop modeling (Figure 32I) supports the intramolecular interaction of β13β14 loop in PsnB. Still, the possibility that PsnB dimers transiently associate together for the reaction via the DFR motif remains.

To clarify the interaction scheme of β13β14 loop of the PsnB, I determined the additional structures of PsnB complex, PsnB-MP-ADP and PsnB-MP-AMPPNP, whose crystals were grown in different buffer conditions (Figure 33). These newly obtained crystal structures have different space group and packing from the previous structure models (Table 1). Interestingly, in these structures, β13β14 loop is flipped toward to ATP binding site of the enzyme and recognizes nucleotide intramolecularly, which is very similar to the loop modeling result. The interaction scheme of $\mathrm{DFR}_{233\text{-}235}$ also resembles that of the previous structures (Figure 31). Especially, the side-chain of Arg235 forms H-bond with β- and γ-phosphate of the nucleotide, which may be critical for enzyme activity via increasing the electrophilicity of γ-phosphate. All these three residues, $\mathrm{DFR}_{233\text{-}235}$, are highly conserved in graspetide biosynthetic enzymes (Figure 20) and the interaction patterns of these residues are also observed in the CdnC structure[27], indicating the catalytic significance of these residues in graspetide biosynthesis. To confirm their importance in enzyme reaction, Ala mutants of these residues were prepared and their activities were checked (Figure 34). Ala mutation on these residues abolished the macrocyclization activity indicating the catalytic importance of $\mathrm{DFR}_{233\text{-}235}$. Collectively, $\mathrm{DFR}_{233\text{-}235}$ in β13β14 loop shows flipped structure that the side-chain of Arg235 that leans toward the active site of the enzyme and binds to γ-phosphate of ATP, which is critical for enzyme catalysis and maybe a common architecture in graspetide biosynthetic enzymes.

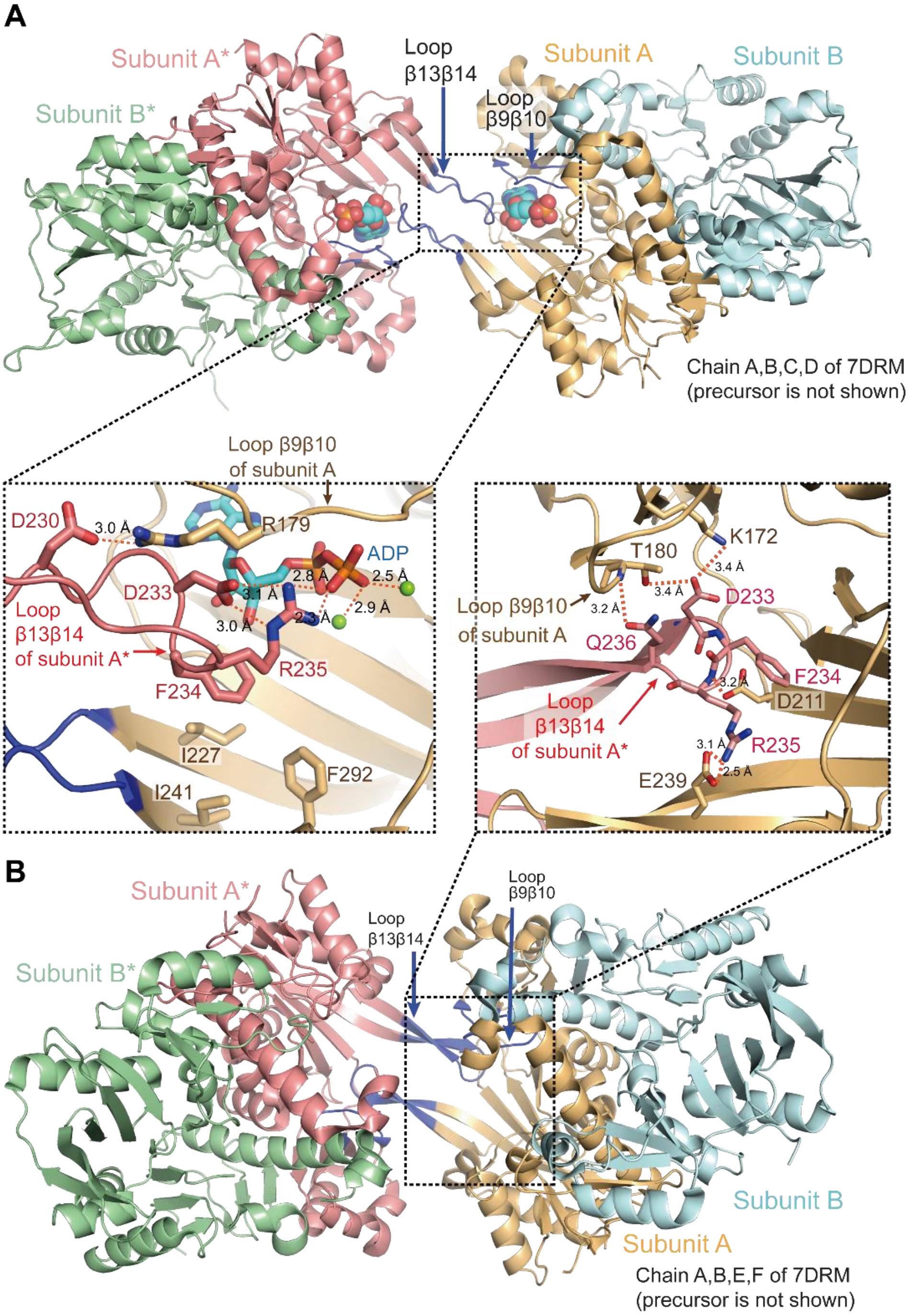
A
Subunit A*
Subunit B*
Loop β13β14
Loop β9β10
Subunit A
Subunit B
Chain A,B,C,D of 7DRM (precursor is not shown)
Loop β9β10 of subunit A
D230
3.0 Å
R179
ADP
2.8 Å
2.5 Å
D233
3.1 Å
2.9 Å
2.3 Å
3.0 Å
Loop β13β14 of subunit A*
R235
F234
I227
F292
I241
K172
T180
3.4 Å
3.4 Å
Loop β9β10 of subunit A
3.2 Å
D233
Q236
F234
3.2 Å
D211
Loop β13β14 of subunit A*
3.1 Å
R235
2.5 Å
E239
B
Subunit A*
Subunit B*
Loop β13β14
Loop β9β10
Subunit B
Subunit A
Chain A,B,E,F of 7DRM (precursor is not shown)

Figure 31. Interdimeric interactions in crystal structures. Loop β13β14 shows an interdimeric interaction with the neighboring subunit. (A) In ENLC-E, loop β13β14 from the subunit A* in the neighboring dimer (red sticks/cartoon) interacts with a nucleotide (cyan sticks), loop β9β10 and hydrophobic residues (yellow sticks) of subunit A. (B) In EL-EL, loop β13β14 from the subunit A* in the neighboring dimer (red sticks/cartoon) interacts with, loop β9β10 and hydrophobic residues (yellow sticks) of subunit A. The atoms in sticks are colored in red (O), blue (N), orange (P), and light green (Mg^{2+}). Hydrogen bonds are shown as red dashed lines.

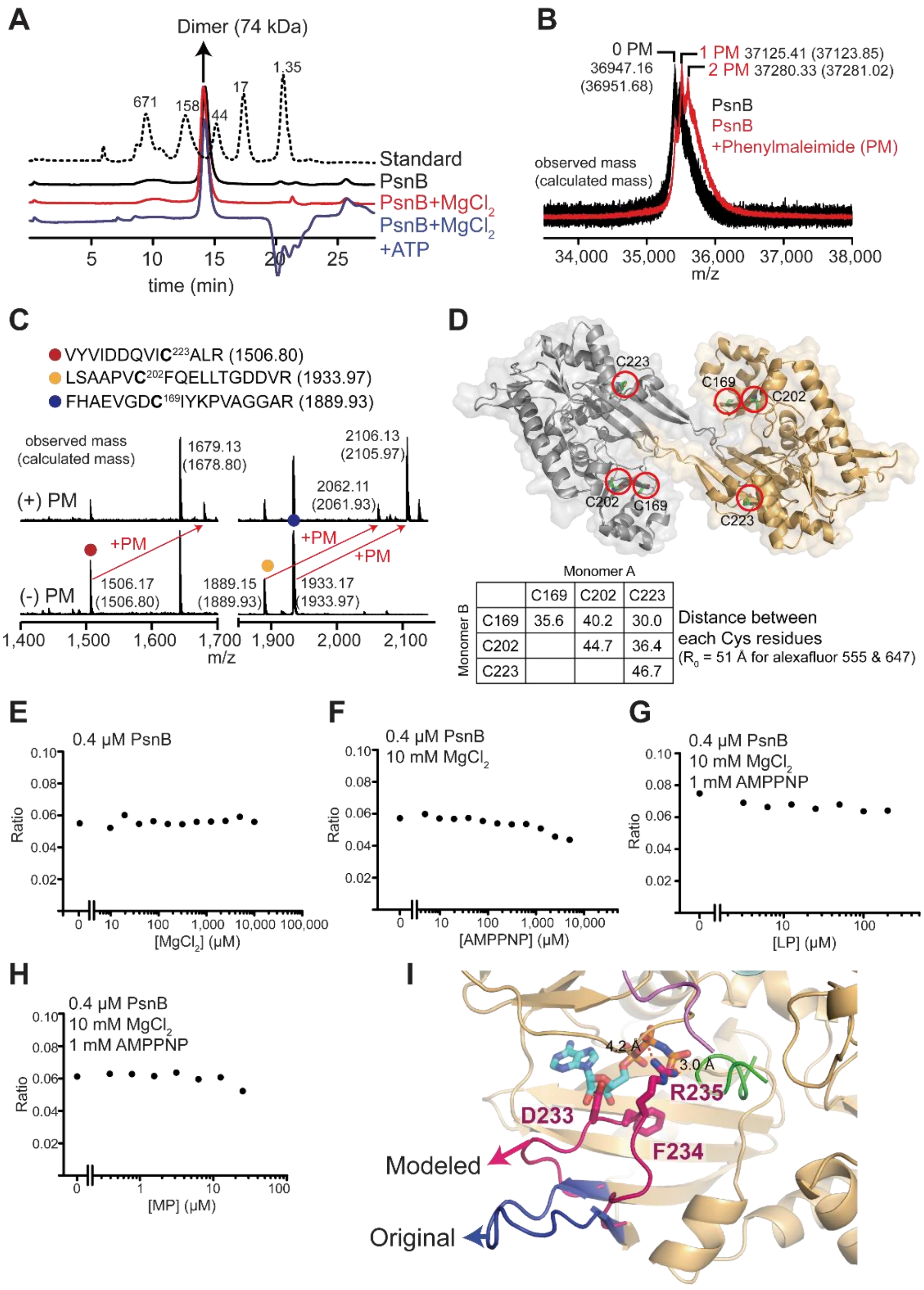

Monomer A

Monomer B	C169	C202	C223
C169	35.6	40.2	30.0
C202		44.7	36.4
C223			46.7

Distance between each Cys residues
(R_0 = 51 Å for alexafluor 555 & 647)

Figure 32. No higher oligomers were observed from PsnB. (A) Gel-filtration chromatogram of PsnB without $MgCl_2$ (black solid line), with $MgCl_2$ (red solid line), or with both $MgCl_2$ and ATP (blue solid line). A chromatogram of molecular weight standard (black dashed line) is also shown with known molecular weights. Addition of nucleotide did not induce the formation of the stable higher oligomer of PsnB dimer. (B-D), Prior to dye labeling, phenylmaleimide labeling was done to characterize the Cys residue of PsnB labeled. (B) From MALDI-MS spectrum of PsnB or PsnB labeled with phenylmaleimide (PM), 1 to 2 PM molecules were added to PsnB. (C) Trypsin digestion revealed that Cys169, Cys202, and Cys223 of PsnB are mainly labeled. (D) From the structure of inter-dimeric interaction, all of these residues are close to each other (30 to 45 Å), which is shorter than R_0 for Alexa fluor 555 and Alexa fluor 647 (51 Å). Pair-wise distances of three Cys residues between two neighboring dimers are shown in a table. (E-H) FRET of a solution containing both donor- and acceptor-labeled PsnB was measured with different amounts of $MgCl_2$ (E), AMPPNP (F), LP (G), or MP (H). Additional components in solutions are listed above the plots. Neither nucleotide nor precursor induced stable intermolecular interaction of PsnB. (I) Loop modeling of loop β13β14. DFR loop is long and flexible enough for intramolecular interaction. DFR loop region, from Ile227 to Ile247, was modeled by FALC[72,73] and overall complex structure was optimized by relaxation. In the modeling structure, the conformation of modeled loop was flipped and DFR residues moved toward the enzyme active site. Also, Arg235 had hydrogen bonding with nucleotide which is similar to the intermolecular interaction scheme shown in crystal structures.

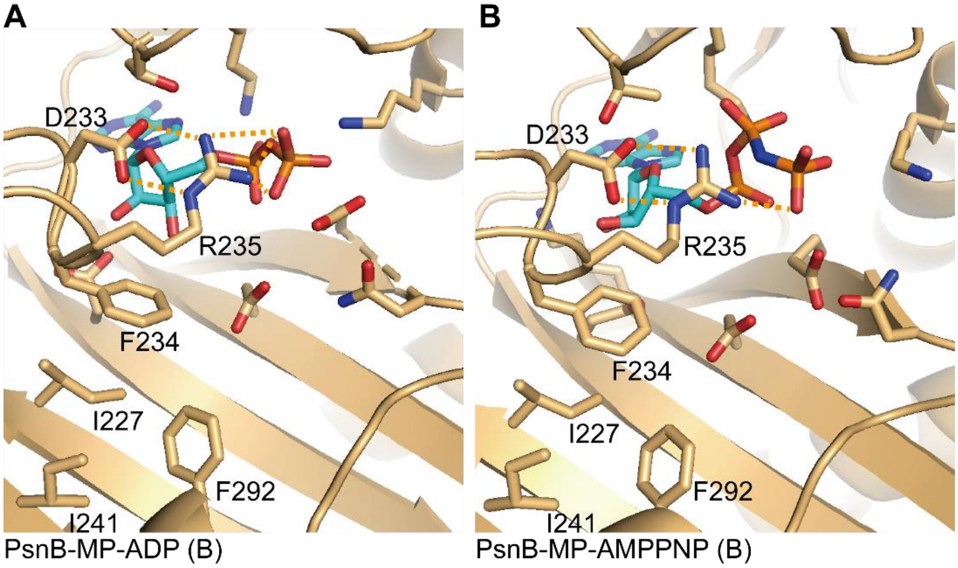

Figure 33. Intramolecular interaction between DFR motif and nucleotide. Arg235 of PsnB (yellow sticks/cartoon) interacts with phosphate of nucleotide (cyan sticks; β-phosphate of ADP or γ-phosphate of AMPPNP). Asp233 forms electrostatic interaction with Arg235. Phe234 sits on the hydrophobic patch of the PsnB which is composed of Ile227, Ile241, and Phe292.

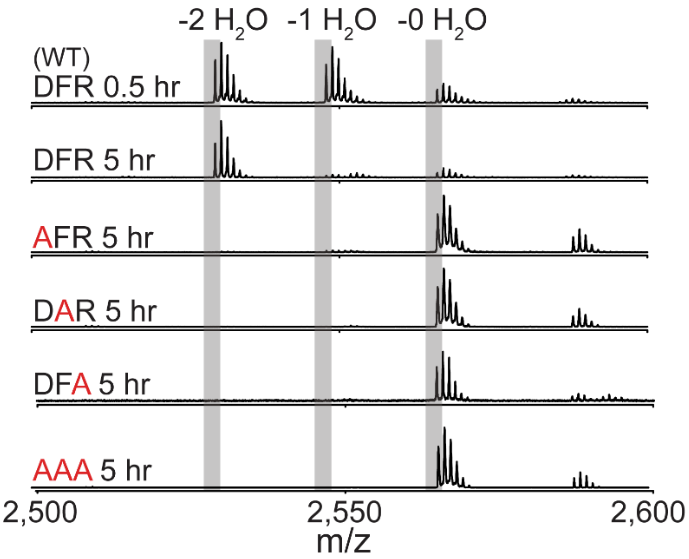

Figure 34. Activity of PsnB mutants in DFR motif. MALDI spectra of the reactions with PsnB variants (0.4 µM; 40 µM MP) that contain alanine mutation(s) in the DFR motif. Mutations on DFR abolished the enzyme activity.

3.8. PsnB complex structures of reaction intermediate or transition state mimic.

Former structural analyses highly expanded the understanding of the structural basis underlying the initial stage of the reaction, the substrate binding. Questions about molecular mechanism in PsnB catalysis still remains though. How can the phosphorylation and macrocyclization steps be highly coupled? Which residue functions as a catalytic base for Thr hydroxyl of core peptide? To answer the questions, I tried to determine the complex structures that display the intermediate or transition state-like structure.

Firstly, I synthesized the peptide mimetic of the phosphorylated peptide intermediate ($CO\text{-}OPO_3^{2-}$) by replacing unstable acyl-phosphate group with a more stable acyl difluoro-phosphonate ($CO\text{-}CF_2PO_3^{2-}$; see Figure 35 or Materials and Methods for chemical synthesis of Fmoc-pE37(**6**) and MP(pE37)). Synthesized phosphomimetic peptide showed tight binding to the PsnB (Figure 36A), whose affinity is between those of the minimal precursor peptide and the leader peptide, and inhibitor activity that delays the macrocyclization reaction better than the leader peptide (Figure 36B), which allude that the phosphomimetic peptide resembles the acyl-phosphate intermediate of the precursor peptide. The crystal structure of PsnB with the precursor carrying the phosphomimetic Glu37 (MP(pE37)) was determined (Table 1) and revealed that Arg213 binds to Glu38, instead of pE37 (Figure 36C). In this structure, however, I could not observe any direct interaction of PsnB with phosphonate, which rather faces the solvent region. Direction of the phosphonate was also far from the ADP molecule. A hydroxyl of threonine was even not resolved well, and it still remains elusive how the hydroxyl nucleophile of Thr32 substitutes the phosphate to form an ester linkage.

Next, I synthesized the ATPγS-peptide conjugate (**7**) that resembles the transition state of the reaction (see Figure 37 or Materials and Methods for chemical synthesis of ATPγS-peptide). PsnB complex structure that contains ATPγS-peptide conjugate was determined (Table 1), which displayed well-resolved leader peptide, ATPγS region, and even the core region of the ATPγS-peptide conjugate (Figure 38). Like a phosphomimetic peptide complex structure, Arg213 of PsnB recognizes Glu38. ATPγS region is stably attached to the ATP-binding site of PsnB, possessing a common ATP-enzyme interaction pattern. A covalent linkage between ATPγS and the 37th residue of the peptide is also well resolved and the side-chain of this residue heads toward the γ-phosphate of ATPγS rather than the solvent. Besides, the side-chain of Thr32, which works as a nucleophile, turns toward the active site of the PsnB and faces side-chain of 37th residue. Distance between the hydroxyl oxygen of Thr32 and the C(δ) of 37th residue which corresponds to the carbonyl carbon of Glu was 3.5 Å, suggesting that the stable conformation of the core peptide in phosphorylation step brings the nucleophile hydroxyl group close to acyl-phosphate intermediate, which couples the phosphorylation and ester formation steps.

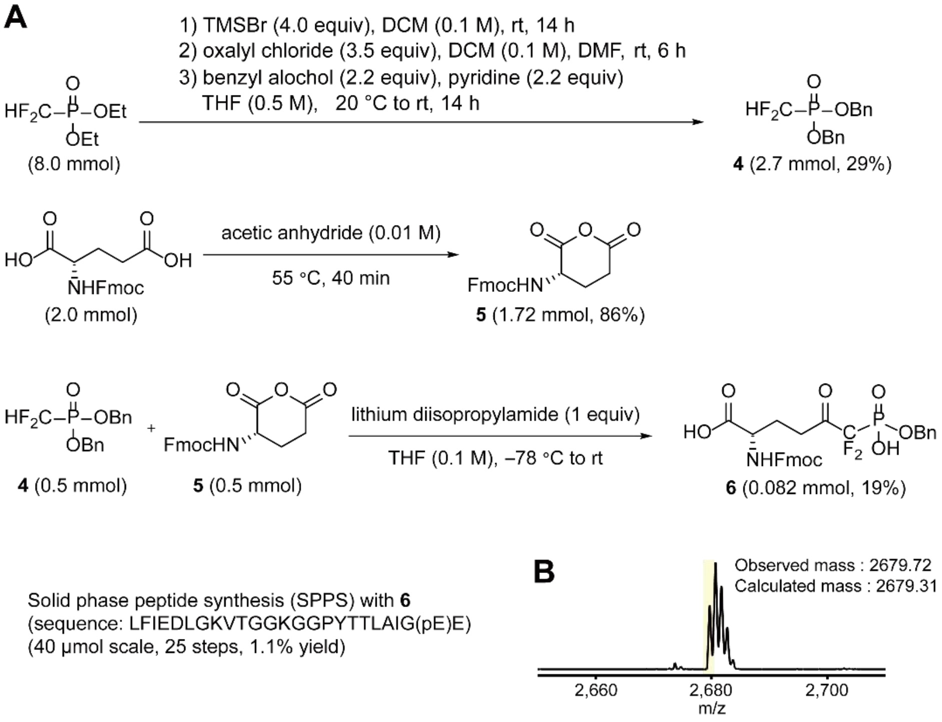

Figure 35. Chemical synthesis of a phosphomimetic glutamate (6). (A) Phosphomimetic glutamate (pE) is synthesized as following scheme. Dibenzyl-difluoromethylphosphonate **4** was generated from Diethyl-difluoromethyl-phosphonate. Fmoc-protected glutamic anhydride **5** was generated from Fmoc-protected glutamic acid[74]. From **4** and **5**, Fmoc-protected benzyl-difluoromethyl-phosphonate **6** was furnished by using LDA[75]. Detailed synthesis procedure is described in Supplementary Note. With **6**, peptide containing pE was synthesized with the yield of 1.1%. Peptide synthesis was performed as described in the method. (B) MALDI spectrum of synthesized phosphomimetic variant at Glu37(MP(pE37)).

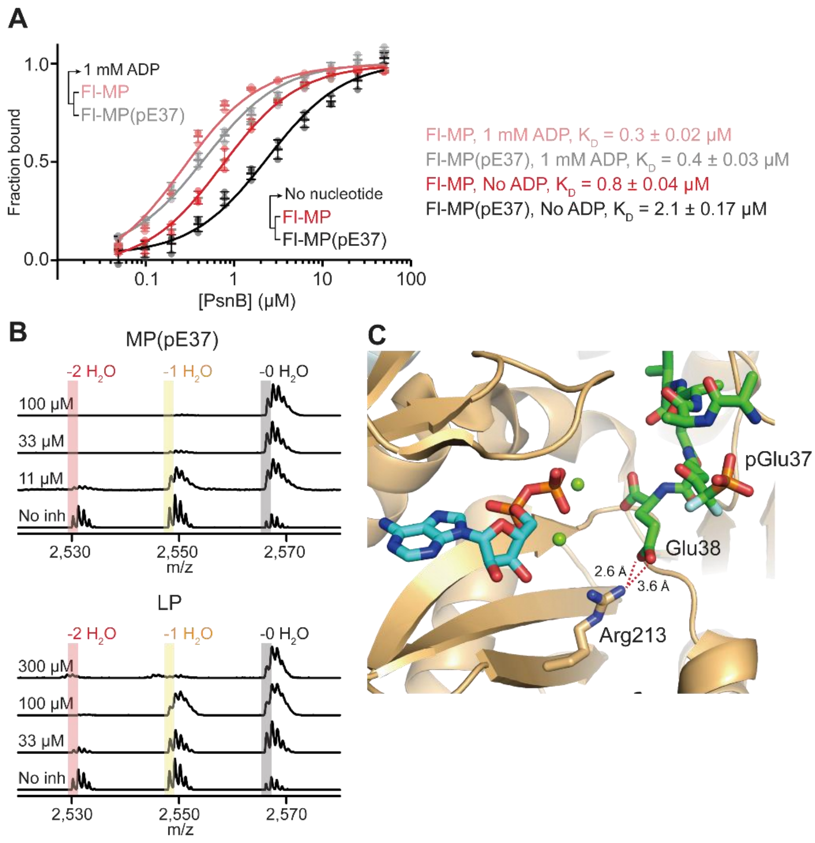

Figure 36. Molecular interaction, binding affinity, and inhibition effect of MP(pE37). a, Detailed interaction scheme of MP(pE37) and PsnB. pGlu37 makes no interaction, whereas Glu38 interacts with Arg213 (yellow sticks) of PsnB. b, Binding affinity of Fl-MP(pE37) to PsnB was measured by fluorescence anisotropy. MP(pE37) binds less tightly to PsnB than the MP no matter whether ADP is present. Data are presented as dot plots with mean ± 1 SD (n = 3 independent experiments) and fitted to a hyperbolic equation. c, Inhibition assay was performed with MP(pE37) or LP. 10 μM MP and 0.4 μM PsnB was co-incubated with various concentrations of MP(pE37) (left) or LP (right) in a buffer containing Tris-HCl (100 mM; pH 7.3), $MgCl_2$ (10 mM), KCl (50 mM) and ATP (5 mM) at 37 °C for 10 min.

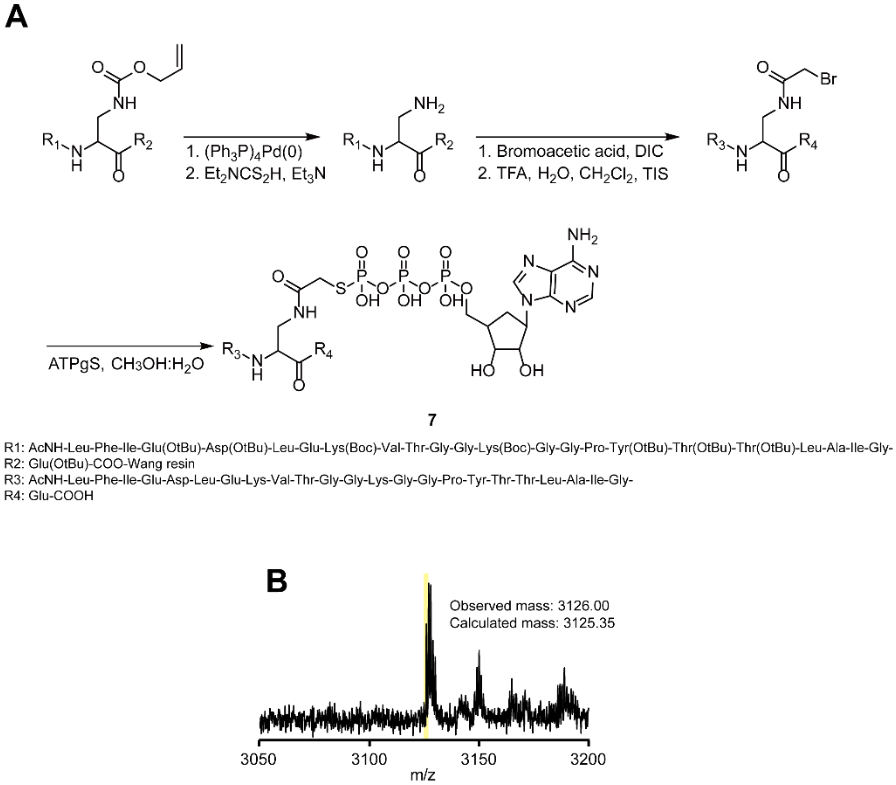

R1: AcNH-Leu-Phe-Ile-Glu(OtBu)-Asp(OtBu)-Leu-Glu-Lys(Boc)-Val-Thr-Gly-Gly-Lys(Boc)-Gly-Gly-Pro-Tyr(OtBu)-Thr(OtBu)-Thr(OtBu)-Leu-Ala-Ile-Gly-
R2: Glu(OtBu)-COO-Wang resin
R3: AcNH-Leu-Phe-Ile-Glu-Asp-Leu-Glu-Lys-Val-Thr-Gly-Gly-Lys-Gly-Gly-Pro-Tyr-Thr-Thr-Leu-Ala-Ile-Gly-
R4: Glu-COOH

Figure 37. Chemical synthesis of an ATPγS-peptide conjugate (7). (A) ATPγS-peptide conjugate was synthesized as following scheme. Glu37 is replaced with aminoalanine, bromoacetylated, cleaved, and purified. Purified bromo-peptide was then conjugated with ATPγS to produce ATPγS-peptide conjugate (**7**)[76]. (B) Produced ATPγS-peptide conjugate was verified with MALDI mass spectrometry.

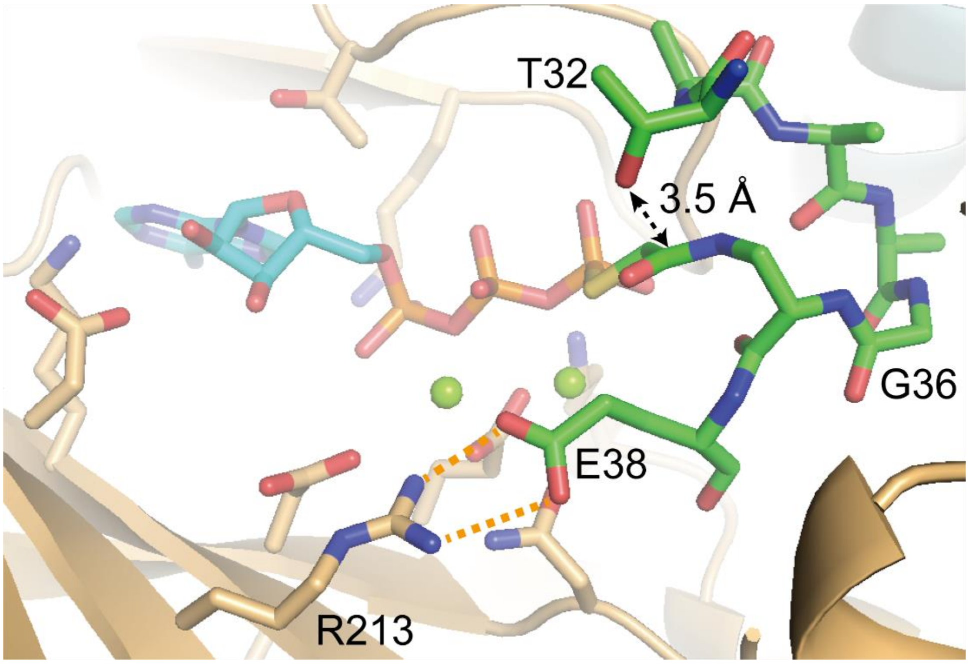

Figure 38. Molecular interaction of ATPec-peptide conjugate. ATPpt-peptide conjugate (green/cyan sticks) shows typical nucleotide binding of ATP-grasp ligase (PsnB, yellow sticks and cartoon). Distance between Thr32 and C(δ) of 37th residue is 3.5 Å. Arg213 recognizes side-chain of Glu38.

3.9. Arg235 may act as a catalytic base during the catalysis.

In the enzymatic reaction of ATP-grasp ligases, a catalytic base that deprotonates nucleophile amine or hydroxyl group is thought to be required for the nucleophilic attack step[52] and the specific catalytic base residue has been postulated for several ATP-grasp ligases (DdlB[59], Biotin carboxylase[51], N^5-CAIR synthetase[48], and MurD[77,78]) based on the structural and mutational studies. In ATPγS-peptide conjugate containing structure, the guanidinium moiety of Arg235 of PsnB leans toward the middle of hydroxyl oxygen of Thr32 and C(δ) of 37th residue, inferring Arg235 may function as a catalytic base that deprotonates hydroxyl of Thr32 and enhances its nucleophilicity (Figure 39A). Distance between Arg235 and Thr32 is 5.0 Å. Meanwhile, Asp233 masks the other side of guanidinium moiety of Arg235 by the electrostatic interaction, which is a very significant interaction scheme that lowers the pKa value of the partner arginine residue and enables it to act as a catalytic base[79,80]. This carboxyl-arginine interaction is commonly observed in other enzymes whose arginine residues work as catalytic base[81-86]. To examine whether Arg235 functions as a catalytic base in PsnB, I cloned PsnB D233N and PsnB R235K mutants and measured their activity (Figure 39B). Both D to N and R to K mutants showed severely reduced activity. Activity of PsnB D233N was reduced about 30-fold while R235K mutation abolished its activity. Collectively, I suggest the catalytic role of Arg235 as a catalytic base, with the assistance of Asp233.

As Asp233 and Arg235 are highly conserved in all of the graspetide biosynthetic enzymes (Figure 20) and a similar Asp-Arg interaction scheme was also observed in CdnC structure (Figure 40A)[27], the role of arginine as a catalytic base might be shared in graspetide biosynthetic enzymes. Though RimK, GshB, and PurT, non-RiPP biosynthetic ATP-grasp enzymes, contain Asp (or Glu) and Arg residues at the same position (Figure 20), similar Asp-Arg pairing and Arg-nucleotide interaction was not observed in their structures (Figure 43B-D)[50,67,69]. There might be another residue for the catalytic base due to different nature of the nucleophile, or similar Asp-Arg interaction would only be transiently formed during the reaction step.

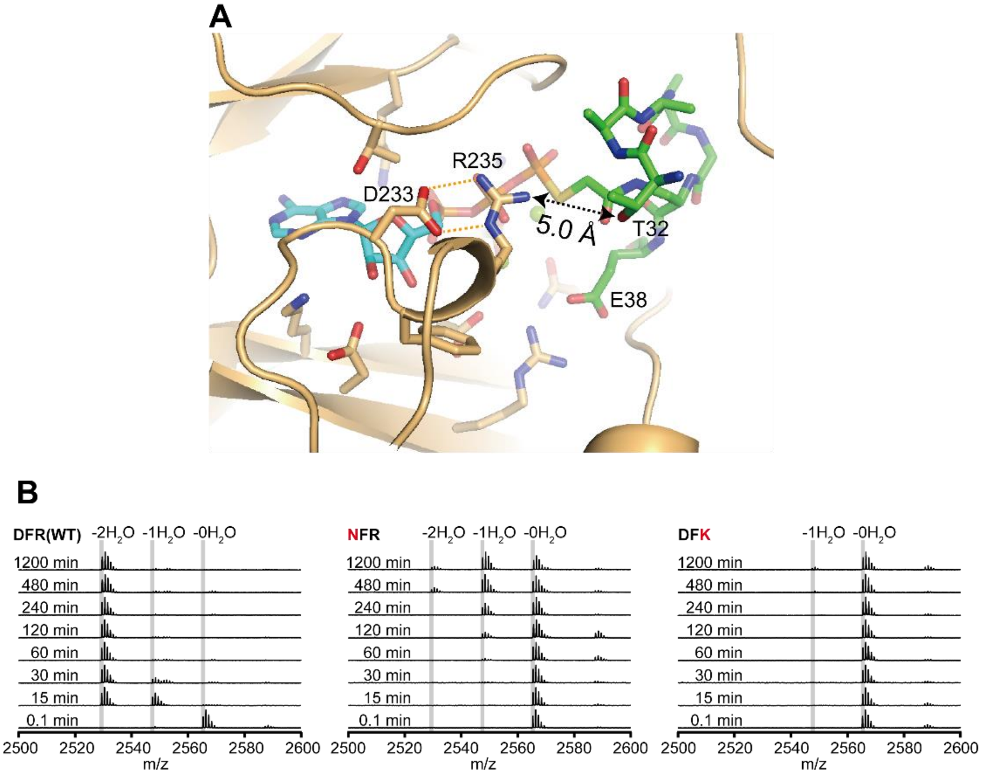

Figure 39. Arg235 may act as a catalytic base. (A) Structure of PsnB (yellow sticks and cartoon) complex with ATPom-peptide conjugate (green/cyan sticks). Arg235 is close to the hydroxyl of Thr32 (5.0 Å). (B) Activity of PsnB D233N and R235K. MALDI spectra of the reactions with PsnB variants (0.5 μM; 100 μM MP). D to N mutation reduced enzyme activity about 30-fold and R to K mutation abolished the enzyme activity.

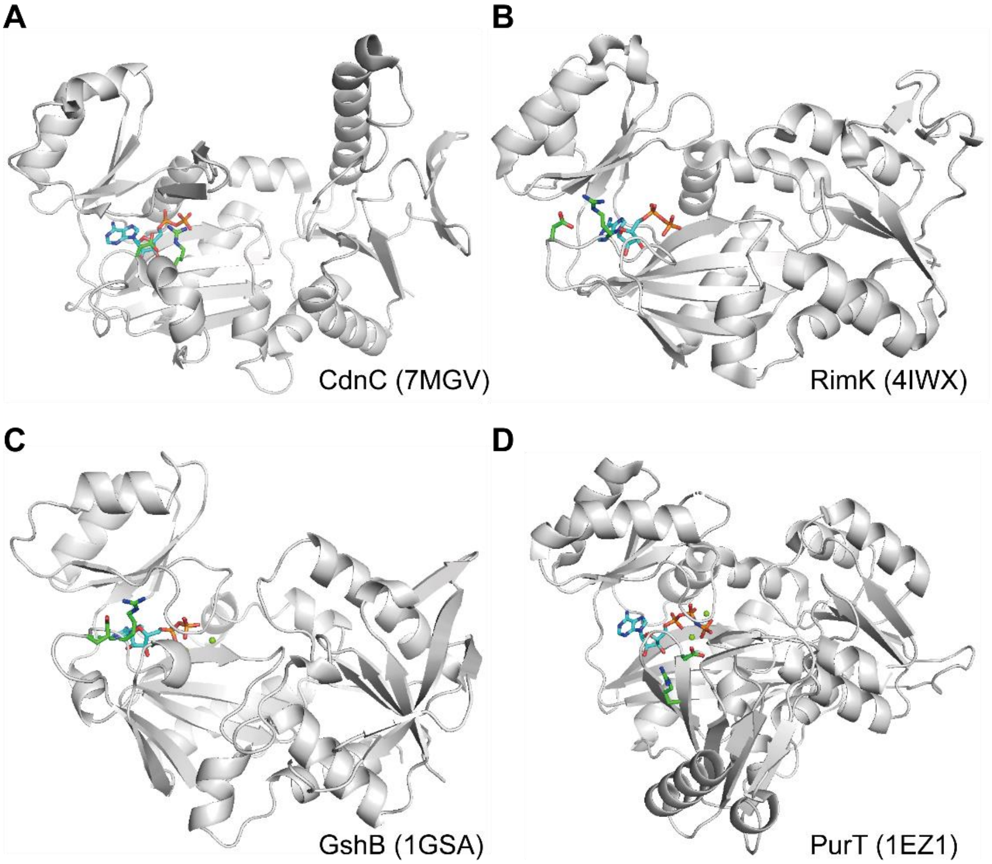

Figure 40. Conformation of DFR motif in other ATP-grasp ligases. Structure of DFR motif in CdnC (A, 7MGV), RimK (B, 4IWX), GshB (C, 1GSA), and PurT (D, 1EZ1). Side-chains of Asp (or Glu) and Arg are shown as green sticks. Nucleotides are colored as cyan. Arg-nucleotide interaction is observed only at CdnC.

Chapter 4. Discussion

4.1. Substrate binding model of PsnB.

In this study, molecular details underlying the interactions between PsnB and its substrates were exhibited by the biochemical and structural analyses. Interestingly, the substrates of the PsnB, leader and core region of the precursor and ATP, affect each other during their binding to the enzyme. Binding of the leader peptide activated the enzyme and allowed the tight binding of the core peptide to the enzyme. Nucleotide binding further enhanced the affinity between enzyme and core peptide. This cooperativity in enzyme-substrate interaction is achieved by the conformational change of enzyme during substrate recognition.

Based on the PsnB complex structures with various substrate combinations, a substrate binding model containing a scheme for the structural change of PsnB was proposed (Figure 41). As the core peptide itself does not tightly bind to the enzyme, binding of the leader peptide or ATP happens firstly. Leader peptide binding shifts α3α4 helices toward the active site, while the binding of ATP moves the leader binding domain (Domain B) to the center of the enzyme and fixes the β13β14 loop by interacting with highly conserved Arg235. These conformational change provides a proper binding site for the core peptide to bind to and makes the PsnB dimer asymmetric. The generated core peptide binding site, composed of three arginine residues (Arg213, Arg101, and Arg72) that recognize two glutamic acid residues (Glu37 and Glu38) and the Gly36 backbone of the core peptide, gives the core peptide a tight binding affinity to the enzyme. After the core peptide binding, β6α3 loop becomes ordered, covering the core peptide.

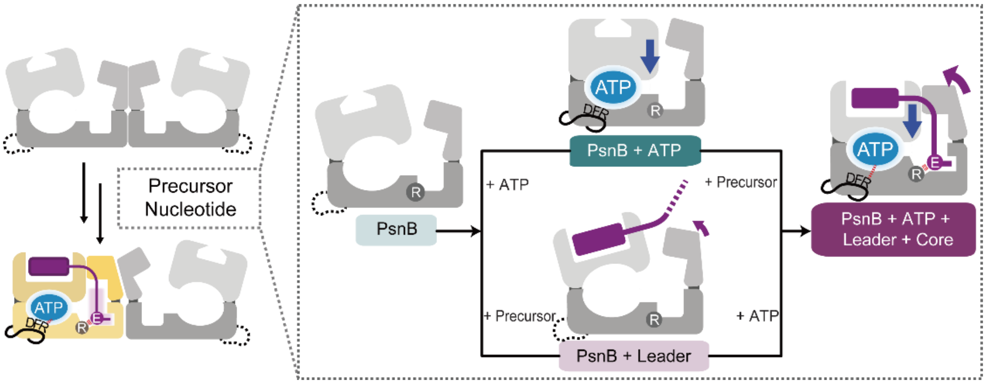

Figure 41. Substrate recognition model of PsnB. The binding of leader and ATP induces distinct conformational changes in PsnB, resulting in enhancement of the core binding. The core binding via conserved Arg213 generates the asymmetric dimer with a compact active site in core-bound PsnB.

4.2. Enzymatic reaction model of PsnB.

After the core peptide binding, core peptide undergoes phosphorylation and ester bond formation reaction. Conformational change of the core peptide during each reaction step can be seen from the snapshots of the steps obtained from crystal structures. Two PsnB-MP-AMPPNP complex structures with distinct core peptide conformations are obtained (I1 and I2; Figure 42A and B, respectively), which represents the initial stage of the enzyme catalysis. Both I1 and I2 display Arg213-Glu37 and Arg101-Glu38 pairing but the core peptide of I2 are more buried in the center of the enzyme, which converts the core peptide into loop-like conformation and brings Thr32 closer to the active site. Hydrogen bonding between hydroxyl of Thr31 and backbone nitrogen of Glu37 might be important for the I2 stage (Figure 42B). Then the core peptide undergoes phosphorylation step and PsnB-ATPγSpep complex (T; Figure 42C) represents the transition-state of this step. In phosphorylation reaction, side-chain of Glu37 heads toward ATP and reacts with γ-phosphate of ATP to yield an acyl-phosphate intermediate. In this step, Glu38 is delivered from Arg101 to Arg213 and loop-like structure of the core peptide rotates altogether. This movement invites hydroxyl of Thr32 close to the carbonyl carbon of acyl-phosphate intermediate, which raises immediate nucleophilic attack by hydroxyl, the following reaction step of PsnB catalysis. Conformation of core peptide in T stage escorts hydroxyl of Thr32 near the side-chain of Arg235, a putative catalytic base for the reaction, and facilitates the following step. I also obtained a PsnB complex structure containing the reaction product, a peptide with one ester crosslink between Thr32 and Glu37 (PsnB-MP(-1H_2O)-ADP; P; Table 1 and Figure 42D). Core peptide with one ester bond forms a stable loop which fit properly to the core binding site of the enzyme. High affinity between PsnB and MP(-1H_2O) (Figures 16A and B) might be attributed to the stable loop structure of the core peptide which matches well with the enzyme active site.

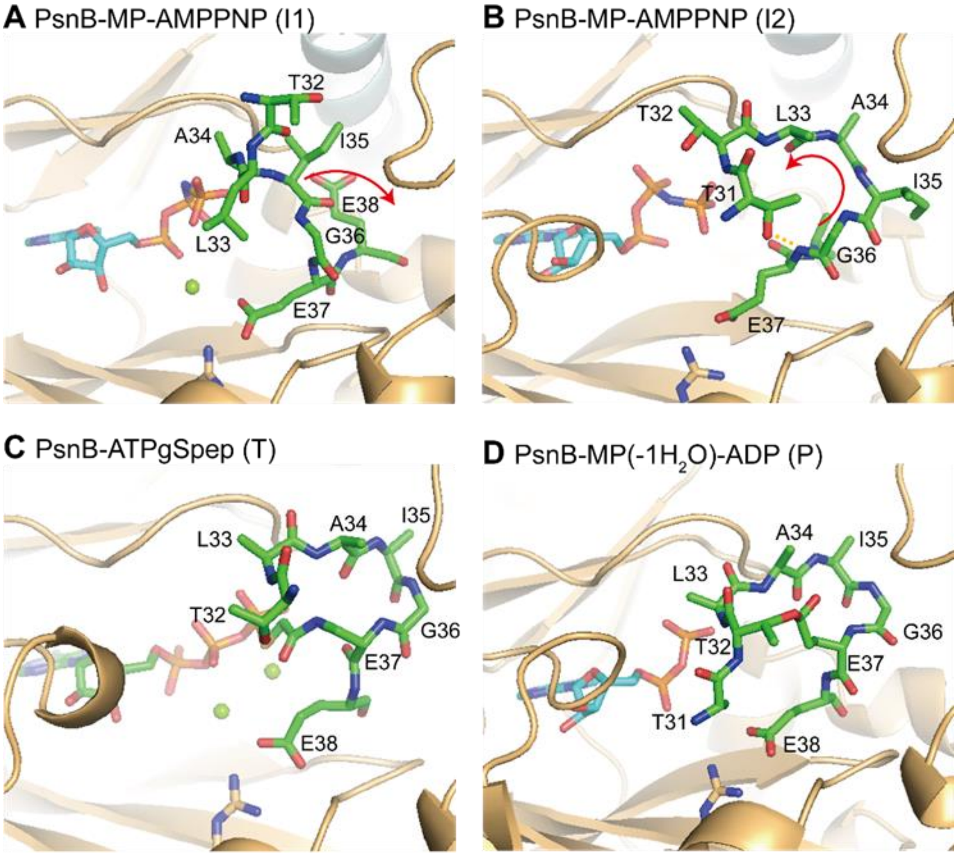

Figure 42. Conformational change of core peptide during the reaction. (A-D) Resolved core peptide regions of the complex structures of PsnB-MP-AMPPNP (A, I1), PsnB-MP-AMPPNP (B, I2), PsnB-ATPγSpep (C, T), and PsnB-MP(-1H_2O)-ADP (D, P). After the core binding (I1), core peptide forms loop-like conformation (I2) and undergoes enzymatic reaction.

4.3. PsnB: ATP-grasp ligase whose activity is strictly regulated

Regulation of enzyme-mediated ATP hydrolysis is crucial to maintain cellular homeostasis of ATP level[87]. PsnB shows strictly regulated ATP consumption that binding of leader peptide enhances ATP consumption rate about 6-fold and that the enzyme is fully active only when every reaction partner—leader peptide, core peptide with highly conserved Thr and Glu, and ATP—exist. Regulation of enzyme activity stems from the conformational change of enzyme during the substrate binding (Figure 41) and conformational change of core peptide during the enzyme reaction (Figure 42). (1) Enzyme conformational change: Binding of leader peptide and nucleotide flips DFR motif and locates catalytic residues toward the active site of the enzyme. Formation of a compact active site and ordered β6α3 loop by the substrate binding fastens the core peptide to the reaction chamber of the enzyme. Regulation of the enzyme by the conformational change is also shown in MdnC and CdnC[24,27]. (2) Conformational change of core peptide: During the enzymatic reaction, core peptide makes loop-like structure which is preferred to undergo the following reaction steps. After the phosphorylation step, reaction-participating hydroxyl group sits near the active site and excludes water molecules which can also work as putative nucleophiles. Highly conserved threonine residues of the core peptide might be responsible for the stabilization of the loop-like structure.

Based on structural and mutational studies, Catalytic residues of PsnB were defined and a model of PsnB reaction mechanism is proposed (Figure43). For the recognition of leader peptide, hydrophobic pocket at the leader-binding domain (B domain) is critical. Leu196 and Phe203 are most important and mutations at those residues impaired the binding of the leader peptide and enzyme activity. Binding of the core peptide is responsible for three arginine residues (Arg72, Arg101, and Arg213). After the substrate binding, macrocyclization reaction happens, which is divided into two steps, phosphorylation and ester formation. (1) Phosphorylation step: Carboxyl side-chain of glutamic acid reacts with ATP, yielding a phospho-glutamic acid intermediate. Arg213 especially recognizes reaction-participating glutamic acid residue of the core peptide, delivering it near to the ATP molecule and initiating the enzymatic reaction. Negative charges of ATP phosphate are stabilized by Mg^{2+} and positively charged residues (Lys133, Lys172, and Arg235) of the enzyme, which enhances the phosphorylation reaction by lowering the electrostatic repulsion between the γ-phosphate and the carboxyl group. (2) Ester formation: Acyl-phosphate intermediate then reacts with hydroxyl group of threonine to yield ester linkage. Catalytic base is thought to be needed for the deprotonation of the hydroxyl group, enhancing their nucleophilicity. From the transition-state mimicking structure and the mutation studies, Arg235 is proposed to act as a catalytic base.

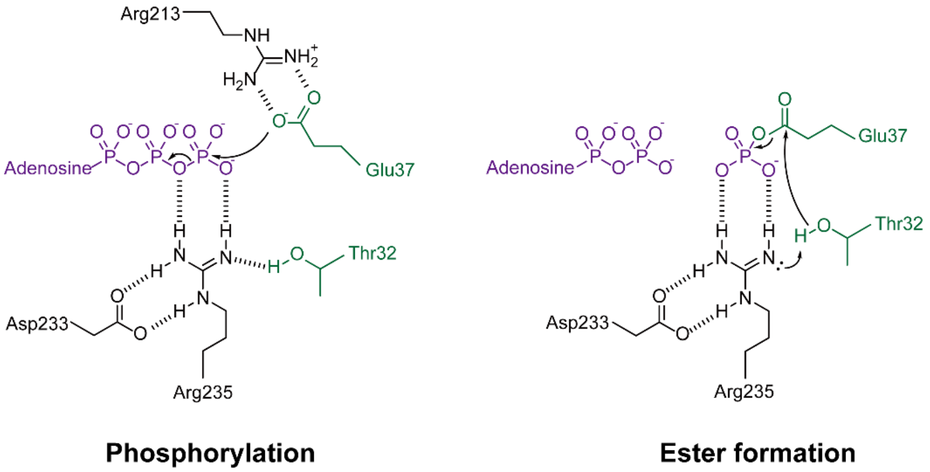

Phosphorylation

Ester formation

Figure 43. Suggested model of enzyme reaction. For the phosphorylation step, Arg213 of PsnB (black) recognizes and locates Glu37 of core peptide (green) close to ATP (purple). Carboxyl side-chain of Glu37 is then phosphorylated, yielding ADP. Arg235 and other positively charged residues stabilize phosphate and promotes the phosphorylation step. After the phosphorylation, ester formation step is performed by the nucleophilic attack of acyl-phosphate by the hydroxyl of Thr32. Thr32 is thought to be activated by the Arg235 which deprotonates and activates the hydroxyl group.

4.4. Role of leader peptide.

Leader peptide tightly binds to the PsnB via the hydrophobic interaction between the highly conserved Phe of leader peptide and the hydrophobic pocket of the PsnB. Cation-π and electrostatic interactions also support the enzyme-leader binding. This unique enzyme-leader interaction scheme is only conserved in group2a graspetide whose leader peptide contains a conserved LFIEDL motif. Biosynthetic enzymes in different groups cannot process the precursor with the leader of group2a, inferring the divergent evolution of enzymes across the different groups[44]. Co-evolution of enzyme and precursor brings orthogonality which allows biosynthesis of non-natural hybrid RiPP products by the fusion of leader peptides[88].

In RiPP biosynthesis, it is critical for the biosynthetic enzymes to recognize the leader peptide since the enzyme-leader interaction brings the core region close to the active site of the enzymes. Besides, enzyme-leader peptide interaction has an additional role, enzyme activation[66]. Likewise, binding of the leader peptide to the PsnB enhances the activity of PsnB. When PsnB meets leader peptide, ATP-consumption rate was elevated about 6-fold, which is further increased when the core peptide is in presence. Binding of the leader peptide also enhanced the affinity of the core peptide to the PsnB. Leader-mediated enzyme activation is explained by the conformational change of enzyme. Enzyme activating feature of leader peptide is also observed in other RiPP biosynthetic enzymes[66]. Lanthipeptide synthetase HalM1 and HalM2 showed synergistic binding of the leader and core peptides[32]. *In trans* addition of the leader and core peptides of the precursor LctA to LctM resulted in increased reaction rate[89]. Leader fused LctM showed even enhanced enzyme activity[63]. *In trans* activity also has been observed in the case of nisin[90], catenulipeptin[65], and microcin J25[91].

4.5. Unusual tight binding between the core peptide and PsnB.

In many RiPP biosynthetic systems, core peptide does not directly interact with the cognate modifying enzyme. Core peptide of PsnA2 (PsnA2$_{28\text{-}38}$) solely showed only a minimal binding affinity to the PsnB (> 100 μM) as well. However, the core peptide of PsnA2 is tightly bound to the PsnB in presence of leader peptide, whether *in cis* or *in trans*. The affinity was even enhanced when the nucleotide was added. Due to the cooperativity in core peptide binding, core peptide was well-resolved in structural models when the leader peptide and nucleotide were bound to the complex structure. Likewise, the complex structure of CdnC resolved the core peptide when there are leader peptide and nucleotide[27].

Biochemical and structural analyses revealed that the interaction between PsnB and core peptide is mainly mediated by two glutamic acid residues of the core peptide, which are recognized by the arginine residues of the PsnB. Arg213 of PsnB specifically recognizes the reaction-participating glutamic acid residue and brings the carboxyl side-chain near the γ-phosphate of ATP. Interestingly, precursor peptide with one ester bond (MP-1H_2O), possessing only one glutamic acid residue (Glu38), binds more tightly to the enzyme. It might be due to the restricted loop conformation of MP-1H_2O, which resembles a loop-like structure of core peptide in PsnB-MP-AMPPNP structure.

4.6. Substrate tolerance of PsnB.

Previous research for the development of novel functional biomolecules from the RiPP biosynthetic systems have relied on biosynthetic enzymes with broad substrate scope such as ProcM[9,11]. So, it is central to determine the substrate tolerance of the modifying enzyme and to discover new enzymes with broad substrate tolerance for the engineering of RiPPs. Here, although I did not directly measure the substrate tolerance of the PsnB, it could be estimated by the sequence conservation pattern and the structural models. Sequence conservation pattern of group2a graspetide displays a modestly conserved XAXG motif between the ring-forming Thr and Glu residues (TTXAXGEE) (Figure 6A). The conservation pattern of core peptide alludes that appropriate substrates of PsnB would like to possess Ala and Gly at an adequate position. Interspace between PsnB and side-chain of the core peptide also suggests substrate scope of the enzyme. Similar to the conservation pattern, side-chain of Ala34 and C(α) of Gly36 are blocked with the enzymatic surfaces while, for Leu33 and Ile35, interfaces between PsnB and side-chains reveal more opened space. Collectively, putative substrates of PsnB are likely to contain the TTXAXGEE motif at the core peptide.

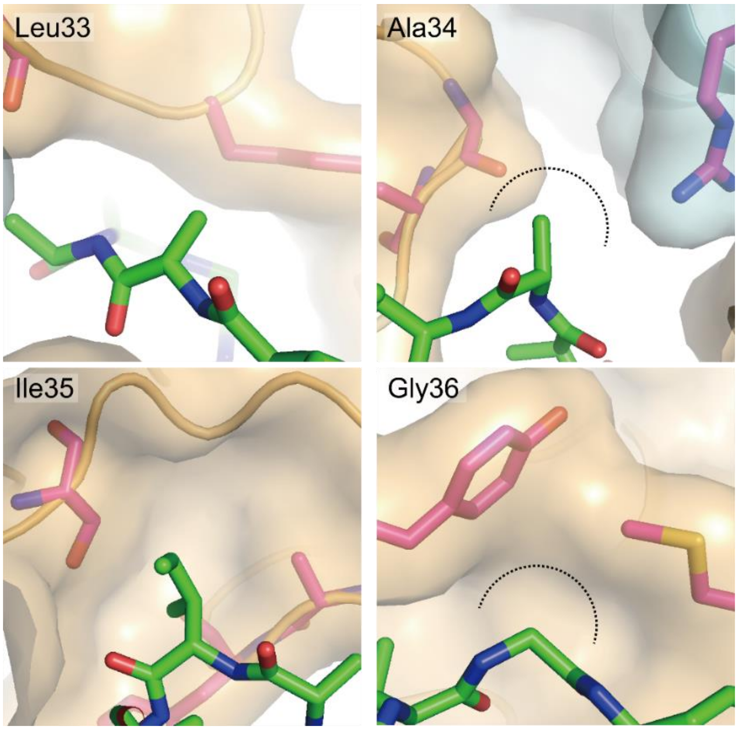

Figure 44. Enzyme-core interface. Interface between the PsnB (yellow/pale cyan, cartoon and surface) and Leu33-Ala34-Ile35-Gly36 of the core peptide (green sticks) shows interspace between the enzyme and core peptide. Enzyme residues closer than 5Å to the Cβ (or Cα for Gly36) of the core peptide residues are displayed as magenta sticks. Side-chain of the Ala34 and Gly36 are surrounded by the enzyme surfaces while the side-chain of the Leu33 and Ile35 are relatively solvent-exposed.

Materials and Methods

General materials and methods. Reagents for cloning were purchased from Enzynomics or Toyobo. Oligonucleotides were purchased from Macrogen. *Escherichia coli* DH10β and BL21(DE3) strains were used for cloning and protein overexpression, respectively. Protein and peptide concentrations were determined by ultraviolet absorbance at 280 nm. Amino acids, coupling reagents and resins for peptide synthesis were purchased from GL-Biochem. For protein purification, Ni sepharose 6 FastFlow beads were obtained from GE Healthcare. Anion exchange chromatography was performed using an Ä KTA pure system (GE Healthcare) on a MonoQ 5/50 GL column (GE Healthcare). Sample purification and analysis with HPLC were performed using an Agilent 1260 Infinity on a ZORBAX SB-C18 semipreparative column (9.4 × 250 mm, 5-μm particle size; Agilent) and a ZORBAX SB-C18 analytical column (4.6 × 250 mm, 5-μm particle size; Agilent), respectively. Trifluoroacetic acid (TFA; 0.05% (vol/vol)) in water (Solvent A) and 0.05% (vol/vol) TFA in acetonitrile (CH_3CN; Solvent B) were used as mobile phase for HPLC. Mass analysis was performed using an Ultraflextreme MALDI–TOF/ TOF mass spectrometer (Bruker Daltonics).

Cloning, overexpression and purification of PsnB variants. Plasmids and oligonucleotides used in this study are listed in **Tables 2 and 3**, respectively. Plasmids expressing PsnB variants were constructed using an inverse PCR method[92]. PsnB and its variants were expressed and purified as previously described[7]. Briefly, E. coli BL21(DE3) cells containing an appropriate plasmid were grown on LB-agar plate with antibiotics at 37°C for 16 hr. A single colony was incubated into 10 mL of LB with antibiotics at 37°C. Overnight culture was diluted with 1L of LB containing antibiotics at 37°C. When OD600 reached between 0.4 to 0.6, protein expression was induced by adding 0.1 mM of isopropyl β-D-1-thiogalactopyranoside (IPTG) and incubating for 12 hr at 180 rpm. Cells were harvested (4,000 x g for 15 min centrifugation), resuspended with Tris-wash buffer buffer (100 mM Tris-HCl, 300 mM NaCl, and 20 mM imidazole, pH 8.0), and lysed by sonication. Lysate was centrifuged at 18,000 x g for 30 min and the supernatant was applied to Ni Sepharose 6 Fast Flow beads (GE healthcare). Beads were washed with Tris-wash buffer. After, proteins were eluted with Tris-elution buffer (100 mM Tris-HCl, 300 mM NaCl, and 500 mM imidazole, pH 8.0). Amicon centrifugal filter (10K cutoff; Millipore) was used to concentrate the solution and to exchange buffer to 10 mM Tris pH 8.0

Peptide synthesis. MP (PsnA2$_{14\text{–}38}$), LP (PsnA2$_{14\text{–}24}$), CP (PsnA2$_{28\text{–}38}$) and its variants were synthesized by solid-phase peptide synthesis. Wang resin (200 μmol, 208 mg) was washed and soaked with 5 ml of 1:1 dimethylformamide (DMF) and dichloromethane (DCM) for 20 min in a reaction vessel for resin swelling. Attachment of the first amino acid was performed by N,N′- diisopropylcarbodiimide (DIC) coupling. The solution of Fmoc-amino acid-OH (5 equiv.), 4-dimethylaminopyridine (DMAP; 0.1 equiv.) and DIC (4 equiv.) in 2–3 ml of DMF was added to the reaction vessel carrying the resin and incubated at room temperature for 2–3 d. Resins were washed three times with DMF and DCM and were capped by acetic anhydride; acetic anhydride (10 equiv.) and DMAP (0.1 equiv) in 2 ml of DCM was incubated with resins for 1 h. After capping, resins were washed with

DMF and DCM again and mixed with 20% (vol/vol) piperidine in DMF for 30 min to cleave Fmoc. After the DMF and DCM wash, the first amino acid-bound resins went through sequential coupling–capping–deprotection. Coupling was performed by incubating the resins with reaction solution that contained Fmoc-amino acid-OH (5 equiv.) and HATU/N,N-diisopropylethylamine (DIEA; 10/5 equiv.) dissolved in DMF. Then, resins were treated with capping solution (DMF/acetic anhydride/DIEA in a 9:1:0.05 ratio) for 7 min. For the deprotection of Fmoc, resins were mixed with 20% piperidine in DMF for 30 min. Resins were washed with DMF and DCM three times between each step. All the remaining amino acids were sequentially attached by repeating coupling, capping and deprotection. The completion of each step was monitored by tests with ninhydrine or 2,4,6-trinitrobenzenesulfonic acid. After completion of the synthesis, peptides were detached from the resins by incubating the resins with cleavage cocktail (95% TFA, 2.5% deionized water, 2.5% triisopropyl silane) for 3 h. Cleavage solutions were then evaporated and mixed with tenfold excess of ether:hexane solution (1:1) for peptide precipitation. The precipitated peptides were collected by centrifugation at 4,000g for 15 min, dried, dissolved in DMSO, purified by HPLC and lyophilized. For the synthesis of fluorophore-labeled peptides, 5(6)-carboxyfluorescein (Acros) and serine (as a linker) were attached to the N termini of the peptides.

Fluorescence anisotropy. Fluorescence anisotropy was performed as follows: a dye-labeled peptide (0.1 μM) and twofold serial dilutions of PsnB variants (starting at 100–500 μM) were mixed in a buffer containing Tris-HCl (100 mM, pH 7.3), $MgCl_2$ (10 mM) and KCl (50 mM) at 37 ℃. Fluorescence (excitation, 485 nm;

emission, 535 nm; parallel or perpendicular) was monitored after a 1-min incubation by using an Infinite F200pro (Tecan). Data analysis was performed using GraphPad Prism.

ATPase assay. ATPase assays were performed as previously described[56]. Briefly, precursor peptide variants (0–200 μM) and PsnB variants (single concentrations at 0.4–2 μM) were co-incubated at 37 ℃ in a buffer containing ATP (5 mM; Sigma-Aldrich), NADH (400 μM; Sigma-Aldrich), pyruvate kinase (20 U ml^{-1}; Sigma-Aldrich), L-lactic dehydrogenase (20 U ml^{-1}; Sigma-Aldrich), phosphoenolpyruvate (3 mM; Sigma-Aldrich), Tris-HCl (100 mM, pH 7.3), $MgCl_2$ (10 mM) and KCl (50 mM). Reaction mixtures (47.5 μl) without ATP were transferred into a 384-well microplate (SPL life science). Then, 2.5 μl of ATP (100 mM) was supplied just before measurement. After ATP was added, absorbance at 340 nm was measured using an Infinite M200pro (Tecan) equipped with i-Control software. The rate of ATP hydrolysis was calculated from the following equation:

$$\text{ATP consumption rate } (\mathrm{enz}^{-1}\mathrm{min}^{-1}) = -dA_{340}/dt\ [\mathrm{OD\ min}] \times K_{\mathrm{path}}{}^{-1} \times [\mathrm{enz}]^{-1}$$

Here, K_{path} is the molar absorption coefficient for NADH for a given optical path length, OD is the optical density and K_{path} is equal to 6.67×10^2 for a 50-μl-well fill volume. The rates were normally corrected for background NADH decomposition of controls containing neither enzyme nor peptide. Data analysis was performed using GraphPad Prism.

In vitro reaction and analysis of PsnA2 variants. In vitro reactions were performed at 37 ℃ in solutions containing precursor peptide variants (40–100 μM), PsnB variants (0.5–5 μM), ATP (5 mM), Tris-HCl (100 mM, pH 7.3), $MgCl_2$ (10 mM) and KCl (50 mM). At the designated time points, reaction solutions were quenched by adding the same volume of 10% (vol/vol) TFA. After quenching, peptides were desalted using a C18 zip-tip (Millipore) and were analyzed by MALDI–MS. The MS profiles are provided in **Table 4**. Trapping the acyl-phosphate intermediate. Reaction conditions were the same as the in vitro reaction conditions except for the addition of hydroxylamine (0.5 M, final concentration) at the start of the reaction. The reaction was quenched after a 4hr incubation. Hydroxylamine-trapped peptides were monitored by MALDI, purified by HPLC and further analyzed by MALDI–MS/MS. The MS/MS profiles are provided in **Table 5**. Methanolysis to confirm the connectivity of the hydroxylamine-trapped peptides with one ester bond (2-c) was performed as previously described[42].

Chemical synthesis of the phosphomimetic glutamate. The phosphomimetic glutamate (pGlu or pE) contains acyl-difluoro-phosphonate ($CO\text{-}CF_2PO_3^{2-}$) instead of acyl-phosphate ($CO\text{-}OPO_3^{2-}$). Synthesis of the phosphomimic glutamate is described in Supplementary Note. Briefly, benzyl lithiodifluoromethylphosphonate was added to Fmoc-protected glutamic anhydride to furnish phosphomimetic glutamate[75]. Peptide synthesis with the phosphomimetic glutamate was performed in the same fashion as normal peptides.

Chemical synthesis of the ATPγS-peptide conjugate. ATPγS-peptide conjugate was synthesized as previously described[76]. Briefly, aminoalanine is used for the linkage to ATPγS via an acetyl bridge. Minimal precursor peptide was built on wang resin as previously described. Glutamic acid was replaced with Alloc-protected α-Fmoc-aminoalanine, which was then selectively deprotected with tetrakis-triphenyl phosphine palladium(0). The peptide was bromoacetylated, cleaved from the resin and purified by HPLC. ATPγS was coupled to the bromoacetylated peptide to produce the desired compound (**7**). Final HPLC purification was performed with neutral solvents. The structure and purity of the desired compound was verified using MALDI mass spectrometry (Figure. 37B).

Crystallization, data collection and crystallographic analysis. For PsnB-MP-ADP (PDB: 7DRM), PsnB-MP-AMPPNP (PDB: 7DRN) and PsnB-MP(pE37)-ADP (PDB: 7DRP), purified PsnB (3.8 mg/ml) was mixed with nucleotide (5 mM) $MgCl_2$ (5 mM) and 1.2 equiv. of MP ($PsnA2_{14-38}$) or phosphomimetic precursor ($PsnA2_{14-38}$(pE37)). Initial screening was performed in a vapor diffusion and sitting drop format. Small crystals were identified in a reservoir condition of 0.1 M sodium cacodylate, pH 6.5, 0.1 M calcium acetate and 12% PEG8000. pH, salt and precipitant optimization were performed in hanging drop screens. Final reservoir conditions were as follows: PsnB-MP-ADP, 0.1 M sodium acetate pH 5.4 and 7% PEG 3350; PsnB-MP-AMPPNP, 0.1 M sodium acetate pH 5.2 and 6% PEG 3350; PsnB-MP(pE37)-ADP, 0.1 M sodium acetate pH 5.0 and 3% PEG 3350. For PsnB–MP (PDB: 7DRO), purified PsnB (7.6 mg/ml) was mixed with ADP (1 mM), $MgCl_2$ (1 mM) and 1.2 equiv. of MP ($PsnA2_{14-38}$). Initial screening was performed in the same format, and small crystals were identified in a reservoir condition of 0.2 M potassium citrate tribasic monohydrate and 20% (wt/vol) PEG3350. The same optimization processes were done to obtain optimized protein crystals. The final reservoir condition was 10% tacsimate pH 7.6 and 14% PEG 3350. For PsnB-MP-ADP (B), PsnB-MP-AMPPNP (B), PsnB-ATPγSpep, and PsnB-MP(-1H_2O)-ADP, purified PsnB (3.8 mg/ml) was mixed with ADP or AMPPNP (5 mM), $MgCl_2$ (5 mM) and 1.2 equiv. of MP variants. Reservoir conditions were as follows: PsnB-MP-ADP (B), 10% Tacsimate pH 5.0 and 15% PEG 3350; PsnB-MP-AMPPNP (B), 10% Tacsimate pH 5.2, 16% PEG3350; PsnB-ATPγSpep, 10% Tacsimate pH 5.0, 13% PEG3350; PsnB-MP(-1H_2O)-ADP, 10% Tacsimate pH 5.2, 13% PEG3350. Crystals of the PsnB complex were grown at 20 ℃. Crystals were frozen in liquid nitrogen, and diffraction data were collected on the beamline 7A of the Pohang Accelerator Laboratory at a wavelength of 0.97934 Å . Data were processed by using HKL2000[93]. Molecular replacement was performed using Phaser[94], whereby the structure of MdnC (PDB: 5IG9) was used as a model. Refinement with Phenix[95] along with manual model rebuilding and ligand placement with COOT[96] produced the final models. Data collection and refinement statistics for the structural models are provided in Table 1. Polder OMIT maps were calculated for leader peptides, core peptides and nucleotides in Phenix[97]. Structural figures were prepared with PyMol (https://pymol.org/2/).

Binding stoichiometry. Binding stoichiometry between PsnB and minimal precursor peptide was measured by fluorescence anisotropy of fluorophore-labeled MP (Fl_MP). Fl_MP (0.1 μM) and PsnB (10 μM) were co-incubated with 0–20 μM of non-labeled MP in buffer containing 100 mM Tris-HCl (pH 7.3), 50 mM KCl, 10 mM $MgCl_2$ and 1 mM ADP at 37°C. The binding fraction of Fl_MP was measured with the different concentrations of non-labeled MP. Totally symmetric and totally asymmetric binding models were simulated with the K_d of 0.13 μM.

Size-exclusion chromatography. Size-exclusion chromatography was performed using an ÄKTA pure system (GE Healthcare) on a Superdex 200 column (GE Healthcare). Three types of solution were used as an eluent: (1) 20 mM Tris-HCl (pH 8.0), 100 mM NaCl solution; (2) 20 mM Tris-HCl (pH 8.0), 100 mM NaCl, 10 mM $MgCl_2$ solution; and (3) 20 mM Tris-HCl (pH 8.0), 100 mM NaCl, 10 mM $MgCl_2$, 1 mM ATP solution.

Dye labeling and FRET. Purified PsnB was incubated with 10 mM Tris and 10 mM DTT for 1 h and then purified by gel filtration using fresh 10 mM Tris buffer. At first, labeling with phenylmaleimide was performed to monitor which cysteine residues of PsnB were preferentially labeled. Reduced PsnB (50–100 μM) and 5 equiv. of phenylmaleimide were mixed in 10 mM Tris, pH 8.0. After a 2 hr incubation at room temperature, the reaction was quenched with excess DTT. Labeled PsnB was cleaved by adding trypsin (trypsin/PsnB 1:100 (wt/wt)) and analyzed by MALDI–MS/MS. Alexa Fluor 555 and Alexa Fluor 647 (Thermo Fisher Scientific) were covalently linked to native cysteine residues of PsnB in the same condition of phenylmaleimide labeling. After dye labeling, dye-labeled PsnB was purified by size-exclusion chromatography. FRET assays for enzyme assembly were performed with 0.2 μM donor- and acceptor-labeled PsnB using a microplate reader (excitation, 520 nm; emission, 570 or 670 nm; Infinite F200pro, Tecan).

Tables

Table 1A. Data collection and refinement statistics for structure models.

	PsnB +PsnA2$_{14-38}$ +ADP (7DRM)	PsnB +PsnA2$_{14-38}$ +AMPPNP (7DRN)	PsnB +PsnA2$_{14-38}$ (pE37) +ADP (7DRP)	PsnB +PsnA2$_{14-38}$ (7DRO)
Data collection				
Space group	P 1 21 1	P 1 21 1	P 1 21 1	P 21 21 21
Cell dimensions				
a, *b*, *c* (Å)	92.43, 91.29, 100.31	92.29, 92.65, 99.57	89.59, 91.66, 98.20	86.89, 146.94, 167.83
a, b, g (°)	90.00, 101.16, 90.00	90.00, 100.90, 90.00	90.00, 101.31, 90.00	90.00, 90.00, 90.00
Resolution (Å)	32.83-3.28 (3.40-3.28) *	32.95-3.56 (3.69-3.56)	33.19-2.98 (3.01-2.98)	47.04-3.25 (3.37-3.25)
CC1/2	0.99 (0.92)	0.98 (0.92)	0.99 (0.89)	0.97 (0.95)
R_{merge}	0.14 (0.66)	0.18 (0.55)	0.11 (0.58)	0.16 (0.59)
I / s*I*	10.1 (2.36)	5.70 (4.91)	9.40 (5.16)	8.90 (7.37)
Completeness (%)	97.2 (96.2)	99.4 (96.8)	99.1 (92.4)	99.7 (98.2)
Redundancy	7.40 (7.50)	7.40 (7.50)	7.20 (7.30)	14.6 (14.8)
Refinement				
Resolution (Å)	32.83-3.28	32.95-3.56	33.19-2.98	47.04-3.25
No. reflections	24590	19808	31751	34482
R_{work} / R_{free}	0.251 / 0.259	0.224 / 0.228	0.206 / 0.210	0.251 / 0.256
No. atoms	9513	9399	9483	13250
Protein	9441	9337	9335	13250
Ligand/ion	58	88	136	-
Water	14	-	12	-
B-factors	93.28	69.27	69.16	79.64
Protein	93.41	69.25	69.15	79.64
Ligand/ion	77.22	72.04	70.61	-
Water	70.78	-	63.47	-
R.m.s. deviations				
Bond lengths (Å)	0.008	0.007	0.006	0.006
Bond angles (°)	1.12	1.01	0.90	0.98

Table 1B. Data collection and refinement statistics for structure models.

	PsnB +PsnA2$_{14-38}$ +ADP (B)	PsnB +PsnA2$_{14-38}$ +AMPPNP (B)	PsnB + ATPγSpep	PsnB +PsnA2$_{14-38}$ (-1H_2O) + ADP
Data collection				
Space group	P 41	P 41	P 41	P 41
Cell dimensions				
a, *b*, *c* (Å)	59.58, 59.58, 180.80	64.23, 64.23, 183.30	62.63, 62.63, 182.548	60.59, 60.59, 185.15
a, b, g (°)	90.00, 90.00, 90.00	90.00, 90.00, 90.00	90.00, 90.00, 90.00	90.00, 90.00, 90.00
Resolution (Å)	34.53-2.90 (3.01-2.90) *	50.00-2.95 (3.13-2.95)	50.00-2.60 (2.70-2.60)	50.00-2.55 (2.62-2.55)
CC1/2	0.994 (0.811)	0.99 (0.95)	0.98 (0.90)	0.99 (0.93)
R_{merge}	0.10 (0.71)	0.15 (0.84)	0.18 (1.01)	0.10 (0.80)
I / s*I*	11.5 (3.38)	10.00 (6.10)	12.69 (5.27)	17.9 (7.48)
Completeness (%)	99.65 (98.91)	99.9 (99.9)	99.8 (99.9)	99.6 (99.8)
Redundancy	14.7 (16.4)	15.0 (15.2)	15.0 (15.1)	13.5 (14.3)
Refinement				
Resolution (Å)	34.53-2.90	32.26-2.95	30.86-2.60	29.90-2.55
No. reflections	13816	15551	21537	21544
R_{work} / R_{free}	0.254 / 0.291	0.272 / 0.293	0.192 / 0.246	0.226 / 0.272
No. atoms	4753	4703	4771	4859
Protein	4699	4641	4703	4714
Ligand/ion	54	72	95	145
Water	0	0	0	0
B-factors	72.57	64.80	63.00	82.03
Protein	72.60	64.68	62.77	81.53
Ligand/ion	70.43	73.40	78.89	98.19
Water	-	-	-	-
R.m.s. deviations				
Bond lengths (Å)	0.0012	0.012	0.010	0.009
Bond angles (°)	1.98	1.82	1.22	1.28

Table 2. Plasmids used in this study

Plasmids	**Description**	**Reference**
pHB012	pET28b-6His-[Tm]-PsnB	[42]
pYH001	pET28b-6His-[Tm]-PsnB (R192A)	This study
pYH003	pET28b-6His-[Tm]-PsnB (R181A)	This study
pYH006	pET28b-6His-[Tm]-PsnB (L196A)	This study
pYH007	pET28b-6His-[Tm]-PsnB (V201A)	This study
pYH010	pET28b-6His-[Tm]-PsnB (Y171A)	This study
pYH012	pET28b-6His-[Tm]-PsnB (F203A)	This study
pYH013	pET28b-6His-[Tm]-PsnB (R101A)	This study
pYH014	pET28b-6His-[Tm]-PsnB (R213A)	This study
pIN035	pET28b-6His-[Tm]-PsnB (I193A)	This study
pHB100	pET28b-6His-[Tm]-DLFIEDLGKVT-$(GS)_{10}$-PsnB	[7]
pIN036	pET28b-6His-[Tm]-DLFIEDLGKVT-$(GS)_{10}$-PsnB (R72A)	This study
pYH023	pET28b-6His-[Tm]-DLFIEDLGKVT-$(GS)_{10}$-PsnB (R101A)	This study
pYH024	pET28b-6His-[Tm]-DLFIEDLGKVT-$(GS)_{10}$-PsnB (R213A)	This study
pIN028	pET28b-6His-[Tm]-PsnB (D233A)	This study
pIN029	pET28b-6His-[Tm]-PsnB (F234A)	This study
pIN030	pET28b-6His-[Tm]-PsnB (R235A)	This study
pYJ123	pET28b-6His-[Tm]-PsnB (D233N)	This study
pYJ124	pET28b-6His-[Tm]-PsnB (R235K)	This study

Table 3. Oligonucleotides used in this study

Plasmids	**Primers**
pYH001	5'-CAGACAGACGTTCAATCGCATCAGCTTCCAGATCTTTCGC 5'-GGAAGCTGATGCGATTGAACGTCTGTCTGCAGC
pYH003	5'-GGTGCACGCACCGCCAAACTGGAAGCG 5'-CGCTTCCAGTTTGGCGGTGCGTGCACC
pYH006	5'-CAGGTGCTGCAGACGCACGTTCAATGCGATCAGCTTCC 5'-CATTGAACGTGCGTCTGCAGCACCTGTTTGTTTTCAGG
pYH007	5'-CAGTTCCTGAAAACACGCAGGTGCTGCAGACAGACG 5'-CGTCTGTCTGCAGCACCTGCGTGTTTTCAGGAACTGACCGGC
pYH010	5'-GTTGGCGATTGCATTGCGAAACCTGTTGCT 5'-AGCAACAGGTTTCGCAATGCAATCGCCAAC
pYH012	5'-GCACCTGTTTGTGCCCAGGAACTGCTG 5'-CAGCAGTTCCTGGGCACAAACAGGTGC
pYH013, 023	5'-CTGCTGGCCTTTGCCGAACGCAGCACCC 5'-GGGTGCTGCGTTCGGCAAAGGCCAGCAG
pYH014, 024	5'-CCGGCGATGATGTTGCGGTGTATGTTATTGATGATCAGG 5'-CCTGATCATCAATAACATACACCGCAACATCATCGCCGG
pIN035	5'-GCGGAACGTCTGTCTGCAGCACC 5'-GCGATCAGCTTCCAGATCTTTCGCTT
pIN036	5'-GCGAGTCTGTATCAGAGCCCGGGC 5'-CAGATACACGGCGGCCGGACG
pIN028	5'-GCGTTTCGCCAGGCGGAAGAACGCATTGAAGC 5'-GATTTCATCGGTAACAATGCGCAGAGCACA
pIN029	5'-GATGCACGTCAGGCGGAAGAACGCATTGAAGC 5'-GATTTCATCGGTAACAATGCGCAGAGCACA
pIN030	5'-GATTTTGCCCAGGCGGAAGAACGCATTGAAGC 5'-GATTTCATCGGTAACAATGCGCAGAGCACA
pYJ123	5’- AACTTTCGCCAGGCGGAAGAACG 5’-GATTTCATCGGTAACAATGCGCAGAGCACA
pYJ124	5’-GATTTTAAACAGGCGGAAGAACGCATTGAAGC 5’-GATTTCATCGGTAACAATGCGCAGAGCACA

Table 4. Observed and calculated mass values of MALDI data

Ion	Observed	Calculated	Difference
0.1min, 0	2565.16	2565.34	-0.18
7.5min, 2	2529.13	2529.3	-0.17
7.5min, 1	2547.24	2547.32	-0.08
15min, 2	2529.09	2529.3	-0.21
15min, 1	2547.14	2547.32	-0.18
30min, 2	2529.1	2529.3	-0.2

Figure 7A

Ion	Observed	Calculated (av)	Difference
0.1min, 0	7489.5	7486.2	3.2
30min, 5	7398.4	7396.3	2.1
30min, 6	7381.0	7378.3	2.7
30min, 7	7363.7	7360.4	3.3
30min, 8	7345.2	7342.4	2.8
60min, 8	7345.8	7342.4	3.4
120min, 8	7345.2	7342.4	2.8

Figure 7B

Ion	Observed	Calculated	Difference
1-a	2564.97	2565.34	-0.37
2-a	2546.91	2547.32	-0.41
3-a	2528.87	2529.3	-0.43
1-c	2579.9	2580.35	-0.45
2-c	2561.95	2562.33	-0.38

Figure 9B, left

Ion	Observed	Calculated	Difference
3-a	2529.01	2529.3	-0.29

Figure 9B, right

Ion	Observed	Calculated	Difference
2-c	2562.02	2562.33	-0.31
2-d	2594.04	2594.33	-0.29

Figure 9C

Ion	Observed	Calculated	Difference
PsnB,0	1150.39	1150.56	-0.17
LP_PsnB,0	1150.42	1150.56	-0.14
LP_PsnB,1	1132.42	1132.54	-0.12
LP_PsnB,2	1114.41	1114.52	-0.11

Figure 12C

Ion	Observed	Calculated	Difference
WT,0.1,0	2565.35	2565.34	0.01
WT,7.5,0	2565.39	2565.34	0.05
WT,7.5,1	2547.39	2547.32	0.07
WT,7.5,2	2529.33	2529.3	0.03
WT,15,2	2529.47	2529.3	0.17
T31A,0.1,0	2535.39	2535.33	0.06
T31A,7.5,0	2535.46	2535.33	0.13
T31A,15,0	2535.53	2535.33	0.2
T31A,30,0	2535.49	2535.33	0.16
T31A,30,1	2517.52	2517.31	0.21
T31A,60,0	2535.55	2535.33	0.22
T31A,60,1	2517.56	2517.31	0.25
T31A,120,1	2517.59	2517.31	0.28
T32A,0.1,0	2535.51	2535.33	0.18
T32A,7.5,0	2535.6	2535.33	0.27
T32A,15,0	2535.6	2535.33	0.27
T32A,30,0	2535.6	2535.33	0.27
T32A,60,0	2535.67	2535.33	0.34
T32A,120,0	2535.67	2535.33	0.34
31A32A,0.1,0	2505.53	2505.32	0.21
31A32A,7.5,0	2505.6	2505.32	0.28
31A32A,15,0	2505.64	2505.32	0.32
31A32A,30,0	2505.66	2505.32	0.34
31A32A,60,0	2505.7	2505.32	0.38
31A32A,120,0	2505.73	2505.32	0.41
E37A,0.1,0	2507.58	2507.33	0.25
E37A,7.5,0	2507.64	2507.33	0.31
E37A,7.5,1	2489.62	2489.31	0.31
E37A,15,0	2507.6	2507.33	0.27
E37A,15,1	2489.62	2489.31	0.31
E37A,30,0	2507.69	2507.33	0.36
E37A,30,1	2489.62	2489.31	0.31
E37A,60,1	2489.75	2489.31	0.44
E37A,120,1	2489.8	2489.31	0.49
E38A,0.1,0	2507.51	2507.33	0.18
E38A,7.5,0	2507.58	2507.33	0.25
E38A,7.5,1	2489.5	2489.31	0.19
E38A,15,0	2507.6	2507.33	0.27
E38A,15,1	2489.59	2489.31	0.28
E38A,30,0	2507.71	2507.33	0.38
E38A,30,1	2489.7	2489.31	0.39
E38A,60,0	2507.67	2507.33	0.34
E38A,60,1	2489.66	2489.31	0.35
E38A,120,1	2489.75	2489.31	0.44
37A38A,0.1,0	2449.54	2449.33	0.21
37A38A,7.5,0	2449.63	2449.33	0.3

37A38A,15,0	2449.67	2449.33	0.34
37A38A,30,0	2449.67	2449.33	0.34
37A38A,60,0	2449.72	2449.33	0.39
37A38A,120,0	2449.77	2449.33	0.44

Figure 14

Ion	**Observed**	**Calculated**	**Difference**
WT,0.01,0	2565.31	2565.34	-0.03
WT,0.5,2	2529.08	2529.3	-0.22
WT,2,2	2529.24	2529.3	-0.06
WT,8,2	2529.24	2529.3	-0.06
WT,32,2	2529.19	2529.3	-0.11
Y171A,0.01,0	2565.16	2565.34	-0.18
Y171A,0.5,0	2565.26	2565.34	-0.08
Y171A,0.5,1	2547.21	2547.32	-0.11
Y171A,2,0	2565.24	2565.34	-0.1
Y171A,2,1	2547.27	2547.32	-0.05
Y171A,2,2	2529.24	2529.3	-0.06
Y171A,8,1	2547.25	2547.32	-0.07
Y171A,8,2	2529.24	2529.3	-0.06
Y171A,32,1	2547.23	2547.32	-0.09
Y171A,32,2	2529.21	2529.3	-0.09
R181A,0.01,0	2565.4	2565.34	0.06
R181A,0.5,0	2565.31	2565.34	-0.03
R181A,0.5,1	2547.37	2547.32	0.05
R181A,0.5,2	2529.31	2529.3	0.01
R181A,2,2	2529.35	2529.3	0.05
R181A,8,2	2529.31	2529.3	0.01
R181A,32,2	2529.47	2529.3	0.17
R192A,0.01,0	2565.38	2565.34	0.04
R192A,0.5,0	2565.4	2565.34	0.06
R192A,0.5,1	2547.34	2547.32	0.02
R192A,0.5,2	2529.26	2529.3	-0.04
R192A,2,2	2547.3	2547.32	-0.02
R192A,8,2	2529.28	2529.3	-0.02
R192A,32,2	2529.51	2529.3	0.21
I193A,0.01,0	2529.4	2529.3	0.1
I193A,0.5,0	2565.38	2565.34	0.04
I193A,0.5,1	2565.47	2565.34	0.13
I193A,0.5,2	2547.41	2547.32	0.09
I193A,2,2	2529.42	2529.3	0.12
I193A,8,2	2529.51	2529.3	0.21
I193A,32,2	2529.4	2529.3	0.1
L196A,0.01,0	2529.54	2529.3	0.24
L196A,0.5,0	2565.38	2565.34	0.04
L196A,2,0	2565.49	2565.34	0.15
L196A,8,0	2565.49	2565.34	0.15

L196A,32,0	2565.51	2565.34	0.17
V201A,0.01,0	2565.51	2565.34	0.17
V201A,0.5,0	2565.56	2565.34	0.22
V201A,0.5,1	2565.49	2565.34	0.15
V201A,0.5,2	2547.44	2547.32	0.12
V201A,2,2	2529.42	2529.3	0.12
V201A,8,2	2529.49	2529.3	0.19
V201A,32,2	2529.58	2529.3	0.28
F203A,0.01,0	2529.58	2529.3	0.28
F203A,0.5,0	2565.51	2565.34	0.17
F203A,2,0	2565.47	2565.34	0.13
F203A,8,0	2565.61	2565.34	0.27
F203A,32,0	2565.68	2565.34	0.34

Figure 21

Ion	Observed	Calculated	Difference
WT,0.1,0	2565.31	2565.34	-0.03
WT,0.5,2	2529.08	2529.3	-0.22
WT,32,2	2529.19	2529.3	-0.11
R101A,0.1,0	2565.56	2565.34	0.22
R101A,0.5,2	2529.7	2529.3	0.4
R101A,32,2	2529.74	2529.3	0.44
R213A,0.1,0	2565.56	2565.34	0.22
R213A,0.5,0	2565.49	2565.34	0.15
R101A,32,0	2565.65	2565.34	0.31
R101A,32,1	2547.64	2547.32	0.32

Figure 24B

Ion	Observed	Calculated	Difference
DFR,0.5,1	2547.89	2547.32	0.57
DFR,0.5,2	2529.84	2529.3	0.54
DFR,5,2	2529.84	2529.3	0.54
AFR,5,2	2565.99	2565.34	0.65
DAR,5,2	2565.99	2565.34	0.65
DFA,5,2	2565.88	2565.34	0.54
AAA,5,2	2565.99	2565.34	0.65

Figure 34

Ion	Observed	Calculated	Difference
MP(pE37),100,0	2566.52	2565.34	1.18
MP(pE37),33,0	2566.38	2565.34	1.04
MP(pE37),11,0	2566.57	2565.34	1.23
MP(pE37),11,1	2548.56	2547.32	1.24
No inh, 0	2566.23	2565.34	0.89
No inh, 1	2548.27	2547.32	0.95
No inh, 2	2530.23	2529.3	0.93
LP, 300, 0	2566.41	2565.34	1.07

LP, 100, 0	2566.31	2565.34	0.97
LP, 100, 1	2548.31	2547.32	0.99
LP, 33, 0	2566.36	2565.34	1.02
LP, 33, 1	2548.36	2547.32	1.04
LP, 33, 2	2530.32	2529.3	1.02
No inh, 0	2566.22	2565.34	0.88
No inh, 1	2548.26	2547.32	0.94
No inh, 2	2530.29	2529.3	0.99

Figure 36B

Ion	Observed	Calculated	Difference
DFR,0.1,0	2565.36	2565.34	0.02
DFR,15,0	2565.45	2565.34	0.11
DFR,15,1	2547.45	2547.32	0.13
DFR,15,2	2529.44	2529.3	0.14
DFR,30,1	2547.52	2547.32	0.2
DFR,30,2	2529.51	2529.3	0.21
DFR,60,2	2529.45	2529.3	0.15
DFR,120,2	2529.51	2529.3	0.21
DFR,240,2	2529.58	2529.3	0.28
DFR,480,2	2529.65	2529.3	0.35
DFR,1200,2	2529.64	2529.3	0.34
NFR,0.1,0	2565.36	2565.34	0.02
NFR,15,0	2565.43	2565.34	0.09
NFR,30,0	2565.45	2565.34	0.11
NFR,60,0	2565.48	2565.34	0.14
NFR,60,1	2547.45	2547.32	0.13
NFR,120,0	2565.59	2565.34	0.25
NFR,120,1	2547.55	2547.32	0.23
NFR,240,0	2565.57	2565.34	0.23
NFR,240,1	2547.55	2547.32	0.23
NFR,480,0	2565.51	2565.34	0.17
NFR,480,1	2547.49	2547.32	0.17
NFR,480,2	2529.47	2529.3	0.17
NFR,1200,0	2565.64	2565.34	0.3
NFR,1200,1	2547.63	2547.32	0.31
NFR,1200,2	2529.61	2529.3	0.31
DFK,0.1,0	2565.36	2565.34	0.02
DFK,15,0	2565.42	2565.34	0.08
DFK,30,0	2565.45	2565.34	0.11
DFK,60,0	2565.48	2565.34	0.14
DFK,120,0	2565.52	2565.34	0.18
DFK,240,0	2565.55	2565.34	0.21
DFK,240,1	2547.53	2547.32	0.21
DFK,480,0	2565.51	2565.34	0.17
DFK,480,1	2547.49	2547.32	0.17

DFK,1200,0	2565.59	2565.34	0.25
DFK,1200,1	2547.56	2547.32	0.24

Figure 39B

Table 5. Observed and calculated mass values of MS/MS data

Ion	Observed	Calculated	Difference
b2	261.26	261.16	0.1
b5	618.43	618.31	0.12
b9	1015.71	1015.58	0.13
b10	1116.73	1116.63	0.1
b13	1358.77	1358.77	0
b14	1415.84	1415.79	0.05
b15	1472.93	1472.81	0.12
b17	1732.96	1732.93	0.03
b18	1833.98	1833.98	0
b19	1935.04	1935.02	0.02
b20	2048.13	2048.11	0.02
b21	2119.13	2119.14	-0.01
b22	2232.31	2232.23	0.08
b23	2289.36	2289.25	0.11
b24	2433.38	2433.29	0.09
y17	1664.88	1664.84	0.04
y19	1849.98	1849.95	0.03
y20	1963.12	1963.04	0.08
y22	2207.01	2207.11	-0.1
$[M+H]^+$	2579.9	2580.35	-0.45

Figure 9D, 1-b

Ion	Observed	Calculated	Difference
b2	261.08	261.16	-0.08
b5	618.18	618.31	-0.13
b9	1015.39	1015.58	-0.19
b10	1116.36	1116.63	-0.27
b13	1358.42	1358.77	-0.35
b14	1415.4	1415.79	-0.39
b15	1472.4	1472.81	-0.41
b17	1732.42	1732.93	-0.51
b18	1833.56	1833.97	-0.41
b19	1916.59	1917.02	-0.43
b24	2399.9	2400.29	-0.39
b25	2528.96	2529.33	-0.37
y13	1332.31	1332.68	-0.37
y14	1389.35	1389.7	-0.35

y15	1446.35	1446.72	-0.37
y16	1547.36	1547.77	-0.41
y17	1646.36	1646.84	-0.48
y18	1774.53	1774.93	-0.4
y20	1944.59	1945.04	-0.45
y22	2188.75	2189.11	-0.36
y23	2301.88	2302.19	-0.31
$[M+H]^+$	2562.02	2562.33	-0.31

Figure 9D, 2-b

Ion	**Observed**	**Calculated**	**Difference**
b2	261.26	261.16	0.1
b5	618.47	618.31	0.16
b9	1015.8	1015.58	0.22
b10	1116.87	1116.63	0.24
b13	1358.88	1358.77	0.11
b14	1415.9	1415.79	0.11
b15	1472.93	1472.81	0.12
b17	1732.95	1732.93	0.02
b18	1834.13	1833.98	0.15
b19	1935.12	1935.02	0.1
b20	2048.27	2048.11	0.16
b21	2119.27	2119.14	0.13
b22	2232.31	2232.23	0.08
b23	2289.31	2289.25	0.06
b24	2432.38	2432.29	0.09
b25	2561.49	2561.33	0.16
y16	1579.88	1579.77	0.11
y17	1678.88	1678.84	0.04
y19	1864.12	1863.95	0.17
y20	1977.14	1977.04	0.1
y21	2092.16	2092.07	0.09
$[M+H]^+$	2594.04	2594.33	-0.29

Figure 9D, 2-c

Synthesis

1. General Information

Unless otherwise noted, all reactions were performed under inert conditions. Nuclear magnetic resonance (NMR) spectra were recorded in $CDCl_3$ or CD_3CN on Varian 400 NMR (400 MHz) spectrometers, with the residual solvent signal was used as a reference. MestreNova was used for data analysis. High-resolution mass spectrometry (HRMS) was performed at the Organic Chemistry Research Center in Sogang University or at the Department of Chemistry in Seoul National University using the electrospray ionization (ESI) method. Chemical shifts are reported in ppm and coupling constants are given in Hz. Reactions were monitored by thin-layer chromatography (TLC) on EMD Silica Gel 60 F254 plates, and visualized either using UV light (254 nm) or by staining with potassium permanganate and heating. Dichloromethane (CH_2Cl_2) and tetrahydrofuran (THF) were dried using a PureSolv solvent purification system. Deuterated compounds were purchased from Cambridge Isotope Laboratories, Inc. and Sigma-Aldrich Corporation.

2. Reagents

Diethyl (difluoromethyl)phosphonate (Sigma), Bromotrimethylsilane (Acros), Oxalyl chloride (Alfa), Dichloromethane (Acros), N,N-diisopropylethylamine (Alfa), Benzyl alcohol (Samchun), Pyridine (Samchun), Tetrahydrofuran (Fisher), Fmoc-Glu-OH (GL biochem), Acetic anhydride (Samchun), Diisopropylamine (Acros), n-Butyllithium (Acros), Ammonium chloride (Samchun).

3. Substrate Preparation

Dibenzyl (difluoromethyl)phosphonate (4)

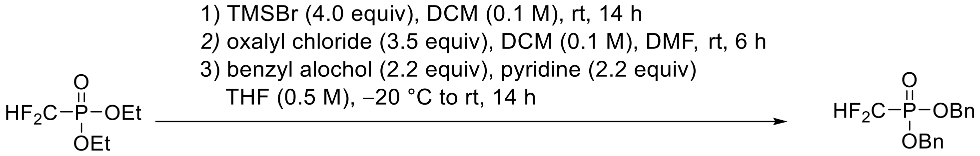

4

Dibenzyl (difluoromethyl)phosphonate was synthesized via a previously reported procedure with slight modifications[98]. To a stirred solution of diethyl (difluoromethyl)phosphonate (1.50 g, 8.0 mmol) in anhydrous CH_2Cl_2 (8 mL) was added bromotrimethylsilane (4.90 g, 32.0 mmol) at room temperature. The reaction mixture was stirred for 14 h at the same temperature and then concentrated to give a residue. To a stirred solution of this residue in anhydrous CH_2Cl_2 (8 mL) was slowly added oxalyl chloride (3.55 g, 28.0 mmol) and DMF (a few drops) at 0 ºC. After being stirred for 6 h at room temperature, the reaction mixture was concentrated to give a residue. To a stirred solution of this residue in THF (16 mL) was added benzyl alcohol (1.90 g, 17.6 mmol) and pyridine (1.39 g, 17.6 mmol) at 20 ºC. After the resulting mixture was stirred for 30 min at the same temperature, stirring was continued for 6 h at room temperature before it was quenched with $KHSO_4$ (sat. aq, 15 mL). The layers were separated and the aqueous layer was extracted with EtOAc (3 × 15 mL). The combined organic extracts were dried (anhydrous Na_2SO_4) and concentrated in *vacuo*. The resulting residue was purified by flash column chromatography (silica gel, hexanes/ EtOAc, gradient elution) to afford **4** (730 mg, 2.7 mmol, 29% yield). All physical and spectroscopic data were in accordance with the literature[75].

(9H-Fluoren-9-yl)methyl (S)-(2,6-dioxotetrahydro-2H-pyran-3-yl)carbamate (5)

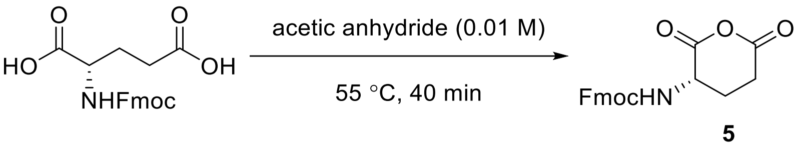

(((9H-fluoren-9-yl)methoxy)carbonyl)glutamic acid (738.7 mg, 2.0 mmol) and acetic anhydride (200 mL) were heated to 55 ºC until the solution turned clear and then were stirred for an additional 40 min at 55 ºC. The solution was cooled and evaporated under reduced pressure (12 mbar) at 55 ºC. The resulting solid was dried under vacuum to afford **5** (604 mg, 1.72 mmol, 86% yield).

^{1}H NMR (400 MHz, CD$_3$CN): δ = 7.84 (d, *J* = 7.5 Hz, 2H), 7.68 (d, *J* = 6.9 Hz, 2H), 7.43 (t, *J* = 7.4 Hz, 2H), 7.35 (t, *J* = 7.3 Hz, 2H), 6.33 – 6.15 (m, 1H), 4.54 – 4.44 (m, 1H), 4.42 – 4.34 (m, 2H), 4.26 (t, *J* = 6.7 Hz, 1H), 2.96 – 2.83 (m, 2H), 2.14 – 2.05 (m, 2H); ^{13}C NMR (101 MHz, CD$_3$CN): δ = 168.35, 167.95, 167.36, 144.98, 142.10, 128.69, 128.09, 126.10, 120.96, 67.55, 51.42, 47.89, 30.51, 23.36; HRMS-ESI (m/z) [M+Na]$^+$ calcd for $C_{20}H_{17}NO_5Na$, 374.1004; found: 374.0990

(2S)-2-((((9H-fluoren-9-yl)methoxy)carbonyl)amino)-6-((benzyloxy)(hydroxy)phosphoryl)-6,6-difluoro-5-oxohexanoic acid (6)

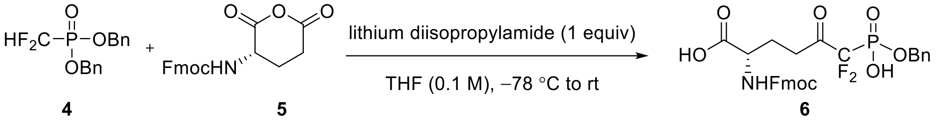

To a stirred solution of diisopropylamine (50.6 mg, 0.5 mmol) in anhydrous THF (2.0 mL) was added a solution of *n*-BuLi (312.5 µL, 1.6 M, 0.5 mmol) in anhydrous THF dropwise at –40 °C. The reaction mixture was warmed up to 0 °C, stirred for 30 min, and cooled down again to –78 °C. To the reaction mixture was added **4** (156.1 mg, 0.5 mmol) in anhydrous THF (0.5 mL) dropwise for 10 min at –78 ºC. After 1 h, the corresponding anhydride **5** (184.7 mg, 0.5 mmol) in anhydrous THF (2.5 mL) was added dropwise to the reaction mixture at –78 ºC. After Stirring for 1 h at –78 ºC, stirring was continued for 10 h at room temperature before it was quenched with NH_4Cl (sat. aq, 5 mL). The layers were separated and the aqueous layer was extracted with EtOAc (5 × 5 mL). The combined organic extracts were dried (anhydrous Na_2SO_4) and concentrated in *vacuo*. The resulting residue was purified by preparative reversed phase HPLC chromatography (Agilent 1260 Infinity / ZORBAX SB-C18 Semi-preparative column (9.4 x 250 mm, 5 µm particle size; Agilent)) to afford **6** (47 mg, 0.082 mmol, 16% yield, elution time: 11.08 min at linear gradient elution program from 58% to 64% eluent B for 13 min (0-2 min: 40% eluent B, 2-15 min: gradient) at a 4.0 mL/min flow rate) which was used in the next reaction.

^{1}H NMR (400 MHz, $CDCl_3$) δ 7.79 – 7.71 (m, 2H), 7.61 – 7.53 (m, 2H), 7.42 – 7.27 (m, 9H), 5.54 – 5.47 (m, 1H), 5.13 (s, 2H), 4.48 – 4.35 (m, 3H), 4.23 – 4.17 (m, 1H), 2.63 – 2.43 (m, 2H), 2.35 – 2.24 (m, 1H), 2.12 – 2.00 (m, 1H) ppm. ^{13}C NMR (101 MHz, $CDCl_3$) δ 175.28, 173.10, 156.35, 143.74, 141.45, 135.70, 128.75, 128.52, 128.46, 127.90, 127.24, 125.20, 120.14, 67.37, 66.89, 53.36, 47.27, 30.51, 29.85, 27.42 ppm*; ^{19}F NMR (376 MHz, $CDCl_3$) δ –114.38 (d, J = 107.1 Hz) ppm**; HRMS-ESI (m/z) $[M-H]^-$ calcd for $C_{28}H_{25}F_2NO_8P$, 572.1286; found: 572.1291

* The ^{13}C signals corresponding to the ketone carbon and the fluorinated alpha carbon could not be detected due to the weak signals originating from the 3J and 2J C-F coupling, respectively[99].

** The ^{19}F NMR chemical shifts for related compounds are reported[100,101].

References

1 Arnison, P. G. *et al.* Ribosomally synthesized and post-translationally modified peptide natural products: overview and recommendations for a universal nomenclature. *Nat Prod Rep* **30**, 108-160, doi:10.1039/c2np20085f (2013).

2 Hudson, G. A. & Mitchell, D. A. RiPP antibiotics: biosynthesis and engineering potential. *Curr Opin Microbiol* **45**, 61-69, doi:10.1016/j.mib.2018.02.010 (2018).

3 Sardar, D., Lin, Z. & Schmidt, E. W. Modularity of RiPP Enzymes Enables Designed Synthesis of Decorated Peptides. *Chem Biol* **22**, 907-916, doi:10.1016/j.chembiol.2015.06.014 (2015).

4 Montalban-Lopez, M. *et al.* New developments in RiPP discovery, enzymology and engineering. *Nat Prod Rep* **38**, 130-239, doi:10.1039/d0np00027b (2021).

5 Newman, D. J. & Cragg, G. M. Natural Products as Sources of New Drugs from 1981 to 2014. *J Nat Prod* **79**, 629-661, doi:10.1021/acs.jnatprod.5b01055 (2016).

6 Kloosterman, A. M., Medema, M. H. & van Wezel, G. P. Omics-based strategies to discover novel classes of RiPP natural products. *Curr Opin Biotechnol* **69**, 60-67, doi:10.1016/j.copbio.2020.12.008 (2021).

7 Lee, C., Lee, H., Park, J. U. & Kim, S. Introduction of Bifunctionality into the Multidomain Architecture of the omega-Ester-Containing Peptide Plesiocin. *Biochemistry* **59**, 285-289, doi:10.1021/acs.biochem.9b00803

(2020).

8 Pan, S. J. & Link, A. J. Sequence diversity in the lasso peptide framework: discovery of functional microcin J25 variants with multiple amino acid substitutions. *J Am Chem Soc* **133**, 5016-5023, doi:10.1021/ja1109634 (2011).

9 Schmitt, S. *et al.* Analysis of modular bioengineered antimicrobial lanthipeptides at nanoliter scale. *Nat Chem Biol* **15**, 437-443, doi:10.1038/s41589-019-0250-5 (2019).

10 Knappe, T. A. *et al.* Introducing lasso peptides as molecular scaffolds for drug design: engineering of an integrin antagonist. *Angew Chem Int Ed Engl* **50**, 8714-8717, doi:10.1002/anie.201102190 (2011).

11 Urban, J. H. *et al.* Phage display and selection of lanthipeptides on the carboxy-terminus of the gene-3 minor coat protein. *Nat Commun* **8**, 1500, doi:10.1038/s41467-017-01413-7 (2017).

12 Yang, X. *et al.* A lanthipeptide library used to identify a protein-protein interaction inhibitor. *Nat Chem Biol* **14**, 375-380, doi:10.1038/s41589-018-0008-5 (2018).

13 King, A. M. *et al.* Selection for constrained peptides that bind to a single target protein. *Nat Commun* **12**, 6343, doi:10.1038/s41467-021-26350-4 (2021).

14 Ortega, M. A. & van der Donk, W. A. New Insights into the Biosynthetic Logic of Ribosomally Synthesized and Post-translationally Modified Peptide Natural Products. *Cell Chem Biol* **23**, 31-44, doi:10.1016/j.chembiol.2015.11.012 (2016).

15 Ortega, M. A. *et al.* Structure and mechanism of the tRNA-dependent lantibiotic dehydratase NisB. *Nature* **517**, 509-512, doi:10.1038/nature13888 (2015).

16 Koehnke, J. *et al.* Structural analysis of leader peptide binding enables leader-free cyanobactin processing. *Nat Chem Biol* **11**, 558-563, doi:10.1038/nchembio.1841 (2015).

17 Regni, C. A. *et al.* How the MccB bacterial ancestor of ubiquitin E1 initiates biosynthesis of the microcin C7 antibiotic. *EMBO J* **28**, 1953-1964, doi:10.1038/emboj.2009.146 (2009).

18 Evans, R. L., 3rd, Latham, J. A., Xia, Y., Klinman, J. P. & Wilmot, C. M. Nuclear Magnetic Resonance Structure and Binding Studies of PqqD, a Chaperone Required in the Biosynthesis of the Bacterial Dehydrogenase Cofactor Pyrroloquinoline Quinone. *Biochemistry* **56**, 2735-2746, doi:10.1021/acs.biochem.7b00247 (2017).

19 Sumida, T., Dubiley, S., Wilcox, B., Severinov, K. & Tagami, S. Structural Basis of Leader Peptide Recognition in Lasso Peptide Biosynthesis Pathway. *ACS Chem Biol* **14**, 1619-1627, doi:10.1021/acschembio.9b00348 (2019).

20 Chekan, J. R., Ongpipattanakul, C. & Nair, S. K. Steric complementarity directs sequence promiscuous leader binding in RiPP biosynthesis. *Proc Natl Acad Sci U S A* **116**, 24049-24055, doi:10.1073/pnas.1908364116 (2019).

21 Ghilarov, D. *et al.* Architecture of Microcin B17 Synthetase: An Octameric Protein Complex Converting a Ribosomally Synthesized Peptide into a

DNA Gyrase Poison. *Mol Cell* **73**, 749-762 e745, doi:10.1016/j.molcel.2018.11.032 (2019).

22 Grove, T. L. *et al.* Structural Insights into Thioether Bond Formation in the Biosynthesis of Sactipeptides. *J Am Chem Soc* **139**, 11734-11744, doi:10.1021/jacs.7b01283 (2017).

23 Davis, K. M. *et al.* Structures of the peptide-modifying radical SAM enzyme SuiB elucidate the basis of substrate recognition. *Proc Natl Acad Sci U S A* **114**, 10420-10425, doi:10.1073/pnas.1703663114 (2017).

24 Li, K., Condurso, H. L., Li, G., Ding, Y. & Bruner, S. D. Structural basis for precursor protein-directed ribosomal peptide macrocyclization. *Nat Chem Biol* **12**, 973-979, doi:10.1038/nchembio.2200 (2016).

25 Chekan, J. R., Estrada, P., Covello, P. S. & Nair, S. K. Characterization of the macrocyclase involved in the biosynthesis of RiPP cyclic peptides in plants. *Proc Natl Acad Sci U S A* **114**, 6551-6556, doi:10.1073/pnas.1620499114 (2017).

26 Ludewig, H. *et al.* Characterization of the Fast and Promiscuous Macrocyclase from Plant PCY1 Enables the Use of Simple Substrates. *ACS Chem Biol* **13**, 801-811, doi:10.1021/acschembio.8b00050 (2018).

27 Zhao, G. *et al.* Structural Basis for a Dual Function ATP Grasp Ligase That Installs Single and Bicyclic omega-Ester Macrocycles in a New Multicore RiPP Natural Product. *J Am Chem Soc* **143**, 8056-8068, doi:10.1021/jacs.1c02316 (2021).

28 Song, H. *et al.* A molecular mechanism for the enzymatic methylation of nitrogen atoms within peptide bonds. *Sci Adv* **4**, eaat2720,

doi:10.1126/sciadv.aat2720 (2018).

29 Ongpipattanakul, C. & Nair, S. K. Molecular Basis for Autocatalytic Backbone N-Methylation in RiPP Natural Product Biosynthesis. *ACS Chem Biol* **13**, 2989-2999, doi:10.1021/acschembio.8b00668 (2018).

30 Bothwell, I. R. *et al.* Characterization of glutamyl-tRNA-dependent dehydratases using nonreactive substrate mimics. *Proc Natl Acad Sci U S A* **116**, 17245-17250, doi:10.1073/pnas.1905240116 (2019).

31 Dong, S. H., Liu, A., Mahanta, N., Mitchell, D. A. & Nair, S. K. Mechanistic Basis for Ribosomal Peptide Backbone Modifications. *ACS Cent Sci* **5**, 842-851, doi:10.1021/acscentsci.9b00124 (2019).

32 Thibodeaux, G. N., McClerren, A. L., Ma, Y., Gancayco, M. R. & van der Donk, W. A. Synergistic binding of the leader and core peptides by the lantibiotic synthetase HalM2. *ACS Chem Biol* **10**, 970-977, doi:10.1021/cb5009876 (2015).

33 Cogan, D. P. *et al.* Structural insights into enzymatic [4+2] aza-cycloaddition in thiopeptide antibiotic biosynthesis. *Proc Natl Acad Sci U S A* **114**, 12928-12933, doi:10.1073/pnas.1716035114 (2017).

34 Reyna-Gonzalez, E., Schmid, B., Petras, D., Sussmuth, R. D. & Dittmann, E. Leader Peptide-Free In Vitro Reconstitution of Microviridin Biosynthesis Enables Design of Synthetic Protease-Targeted Libraries. *Angew Chem Int Ed Engl* **55**, 9398-9401, doi:10.1002/anie.201604345 (2016).

35 Ruffner, D. E., Schmidt, E. W. & Heemstra, J. R. Assessing the combinatorial potential of the RiPP cyanobactin tru pathway. *ACS Synth*

Biol **4**, 482-492, doi:10.1021/sb500267d (2015).

36 Goto, Y., Ito, Y., Kato, Y., Tsunoda, S. & Suga, H. One-pot synthesis of azoline-containing peptides in a cell-free translation system integrated with a posttranslational cyclodehydratase. *Chem Biol* **21**, 766-774, doi:10.1016/j.chembiol.2014.04.008 (2014).

37 Si, Y., Kretsch, A. M., Daigh, L. M., Burk, M. J. & Mitchell, D. A. Cell-Free Biosynthesis to Evaluate Lasso Peptide Formation and Enzyme-Substrate Tolerance. *J Am Chem Soc* **143**, 5917-5927, doi:10.1021/jacs.1c01452 (2021).

38 Fleming, S. R. *et al.* Exploring the Post-translational Enzymology of PaaA by mRNA Display. *J Am Chem Soc* **142**, 5024-5028, doi:10.1021/jacs.0c01576 (2020).

39 Ishitsuka, M. O., Kusumi, T., Kakisawa, H., Kaya, K. & Watanabe, M. M. Microviridin - a Novel Tricyclic Depsipeptide from the Toxic Cyanobacterium Microcystis-Viridis. *Journal of the American Chemical Society* **112**, 8180-8182, doi:DOI 10.1021/ja00178a060 (1990).

40 Ziemert, N., Ishida, K., Liaimer, A., Hertweck, C. & Dittmann, E. Ribosomal synthesis of tricyclic depsipeptides in bloom-forming cyanobacteria. *Angew Chem Int Ed Engl* **47**, 7756-7759, doi:10.1002/anie.200802730 (2008).

41 Philmus, B., Christiansen, G., Yoshida, W. Y. & Hemscheidt, T. K. Post-translational modification in microviridin biosynthesis. *Chembiochem* **9**, 3066-3073, doi:10.1002/cbic.200800560 (2008).

42 Lee, H., Park, Y. & Kim, S. Enzymatic Cross-Linking of Side Chains

Generates a Modified Peptide with Four Hairpin-like Bicyclic Repeats. *Biochemistry* **56**, 4927-4930, doi:10.1021/acs.biochem.7b00808 (2017).

43 Roh, H., Han, Y., Lee, H. & Kim, S. A Topologically Distinct Modified Peptide with Multiple Bicyclic Core Motifs Expands the Diversity of Microviridin-Like Peptides. *Chembiochem* **20**, 1051-1059, doi:10.1002/cbic.201800678 (2019).

44 Lee, H., Choi, M., Park, J. U., Roh, H. & Kim, S. Genome Mining Reveals High Topological Diversity of omega-Ester-Containing Peptides and Divergent Evolution of ATP-Grasp Macrocyclases. *J Am Chem Soc* **142**, 3013-3023, doi:10.1021/jacs.9b12076 (2020).

45 Unno, K. & Kodani, S. Heterologous expression of cryptic biosynthetic gene cluster from Streptomyces prunicolor yields novel bicyclic peptide prunipeptin. *Microbiol Res* **244**, 126669, doi:10.1016/j.micres.2020.126669 (2021).

46 Li, H., Fast, W. & Benkovic, S. J. Structural and functional modularity of proteins in the de novo purine biosynthetic pathway. *Protein Sci* **18**, 881-892, doi:10.1002/pro.95 (2009).

47 Wang, W., Kappock, T. J., Stubbe, J. & Ealick, S. E. X-ray crystal structure of glycinamide ribonucleotide synthetase from Escherichia coli. *Biochemistry* **37**, 15647-15662, doi:10.1021/bi981405n (1998).

48 Thoden, J. B., Holden, H. M. & Firestine, S. M. Structural analysis of the active site geometry of N5-carboxyaminoimidazole ribonucleotide synthetase from Escherichia coli. *Biochemistry* **47**, 13346-13353, doi:10.1021/bi801734z (2008).

49 Zhang, Y., Morar, M. & Ealick, S. E. Structural biology of the purine biosynthetic pathway. *Cell Mol Life Sci* **65**, 3699-3724, doi:10.1007/s00018-008-8295-8 (2008).

50 Hara, T., Kato, H., Katsube, Y. & Oda, J. A pseudo-michaelis quaternary complex in the reverse reaction of a ligase: structure of Escherichia coli B glutathione synthetase complexed with ADP, glutathione, and sulfate at 2.0 A resolution. *Biochemistry* **35**, 11967-11974, doi:10.1021/bi9605245 (1996).

51 Chou, C. Y., Yu, L. P. & Tong, L. Crystal structure of biotin carboxylase in complex with substrates and implications for its catalytic mechanism. *J Biol Chem* **284**, 11690-11697, doi:10.1074/jbc.M805783200 (2009).

52 Fawaz, M. V., Topper, M. E. & Firestine, S. M. The ATP-grasp enzymes. *Bioorg Chem* **39**, 185-191, doi:10.1016/j.bioorg.2011.08.004 (2011).

53 Murzin, A. G. Structural classification of proteins: new superfamilies. *Curr Opin Struct Biol* **6**, 386-394, doi:10.1016/s0959-440x(96)80059-5 (1996).

54 Ahmed, M. N. *et al.* Phylogenomic Analysis of the Microviridin Biosynthetic Pathway Coupled with Targeted Chemo-Enzymatic Synthesis Yields Potent Protease Inhibitors. *ACS Chem Biol* **12**, 1538-1546, doi:10.1021/acschembio.7b00124 (2017).

55 Weiz, A. R. *et al.* Harnessing the evolvability of tricyclic microviridins to dissect protease-inhibitor interactions. *Angew Chem Int Ed Engl* **53**, 3735-3738, doi:10.1002/anie.201309721 (2014).

56 Sausen, C. W., Rogers, C. M. & Bochman, M. L. Thin-Layer Chromatography and Real-Time Coupled Assays to Measure ATP

Hydrolysis. *Methods Mol Biol* **1999**, 245-253, doi:10.1007/978-1-4939-9500-4_15 (2019).

57 Zhang, Y. *et al.* A distributive peptide cyclase processes multiple microviridin core peptides within a single polypeptide substrate. *Nat Commun* **9**, 1780, doi:10.1038/s41467-018-04154-3 (2018).

58 Tanaka, T., Nishioka, T. & Oda, J. Nicked multifunctional loop of glutathione synthetase still protects the catalytic intermediate. *Arch Biochem Biophys* **339**, 151-156, doi:10.1006/abbi.1996.9821 (1997).

59 Shi, Y. & Walsh, C. T. Active site mapping of Escherichia coli D-Ala-D-Ala ligase by structure-based mutagenesis. *Biochemistry* **34**, 2768-2776, doi:10.1021/bi00009a005 (1995).

60 Lipmann, F. & Tuttle, L. C. The detection of activated carboxyl groups with hydroxylamine as interceptor. *J Biol Chem* **161**, 415 (1945).

61 Jencks, W. P. The mechanism of the reaction of hydroxylamine with activated acyl groups. *Biochim Biophys Acta* **27**, 417-418, doi:10.1016/0006-3002(58)90355-x (1958).

62 Weiz, A. R. *et al.* Leader peptide and a membrane protein scaffold guide the biosynthesis of the tricyclic peptide microviridin. *Chem Biol* **18**, 1413-1421, doi:10.1016/j.chembiol.2011.09.011 (2011).

63 Oman, T. J., Knerr, P. J., Bindman, N. A., Velasquez, J. E. & van der Donk, W. A. An engineered lantibiotic synthetase that does not require a leader peptide on its substrate. *J Am Chem Soc* **134**, 6952-6955, doi:10.1021/ja3017297 (2012).

64 Dunbar, K. L. & Mitchell, D. A. Insights into the mechanism of peptide

cyclodehydrations achieved through the chemoenzymatic generation of amide derivatives. *J Am Chem Soc* **135**, 8692-8701, doi:10.1021/ja4029507 (2013).

65 Wang, H. & van der Donk, W. A. Biosynthesis of the class III lantipeptide catenulipeptin. *ACS Chem Biol* **7**, 1529-1535, doi:10.1021/cb3002446 (2012).

66 Yang, X. & van der Donk, W. A. Ribosomally synthesized and post-translationally modified peptide natural products: new insights into the role of leader and core peptides during biosynthesis. *Chemistry* **19**, 7662-7677, doi:10.1002/chem.201300401 (2013).

67 Zhao, G. *et al.* Structure and function of Escherichia coli RimK, an ATP-grasp fold, L-glutamyl ligase enzyme. *Proteins* **81**, 1847-1854, doi:10.1002/prot.24311 (2013).

68 Ouchi, T. *et al.* Lysine and arginine biosyntheses mediated by a common carrier protein in Sulfolobus. *Nat Chem Biol* **9**, 277-283, doi:10.1038/nchembio.1200 (2013).

69 Thoden, J. B., Firestine, S., Nixon, A., Benkovic, S. J. & Holden, H. M. Molecular structure of Escherichia coli PurT-encoded glycinamide ribonucleotide transformylase. *Biochemistry* **39**, 8791-8802, doi:10.1021/bi000926j (2000).

70 Batson, S. *et al.* Inhibition of D-Ala:D-Ala ligase through a phosphorylated form of the antibiotic D-cycloserine. *Nat Commun* **8**, 1939, doi:10.1038/s41467-017-02118-7 (2017).

71 Fan, C., Moews, P. C., Walsh, C. T. & Knox, J. R. Vancomycin resistance:

structure of D-alanine:D-alanine ligase at 2.3 A resolution. *Science* **266**, 439-443, doi:10.1126/science.7939684 (1994).

72 Ko, J. *et al.* The FALC-Loop web server for protein loop modeling. *Nucleic Acids Res* **39**, W210-214, doi:10.1093/nar/gkr352 (2011).

73 Park, H., Lee, G. R., Heo, L. & Seok, C. Protein loop modeling using a new hybrid energy function and its application to modeling in inaccurate structural environments. *PLoS One* **9**, e113811, doi:10.1371/journal.pone.0113811 (2014).

74 Veleti, S. K., Petit, C., Lindenberger, J. J., Ronning, D. R. & Sucheck, S. J. Zwitterionic pyrrolidene-phosphonates: inhibitors of the glycoside hydrolase-like phosphorylase Streptomyces coelicolor GlgEI-V279S. *Org Biomol Chem* **15**, 3884-3891, doi:10.1039/c7ob00388a (2017).

75 Bouwman, S., Orru, R. V. & Ruijter, E. Stereoselective synthesis of fluorinated aminoglycosyl phosphonates. *Org Biomol Chem* **13**, 1317-1321, doi:10.1039/c4ob02317j (2015).

76 Hines, A. C. & Cole, P. A. Design, synthesis, and characterization of an ATP-peptide conjugate inhibitor of protein kinase A. *Bioorg Med Chem Lett* **14**, 2951-2954, doi:10.1016/j.bmcl.2004.03.039 (2004).

77 Bertrand, J. A. *et al.* Determination of the MurD mechanism through crystallographic analysis of enzyme complexes. *J Mol Biol* **289**, 579-590, doi:10.1006/jmbi.1999.2800 (1999).

78 Perdih, A., Hodoscek, M. & Solmajer, T. MurD ligase from E. coli: Tetrahedral intermediate formation study by hybrid quantum mechanical/molecular mechanical replica path method. *Proteins* **74**, 744-

759, doi:10.1002/prot.22188 (2009).

79 Guillen Schlippe, Y. V. & Hedstrom, L. A twisted base? The role of arginine in enzyme-catalyzed proton abstractions. *Arch Biochem Biophys* **433**, 266-278, doi:10.1016/j.abb.2004.09.018 (2005).

80 Fitch, C. A., Platzer, G., Okon, M., Garcia-Moreno, B. E. & McIntosh, L. P. Arginine: Its pKa value revisited. *Protein Sci* **24**, 752-761, doi:10.1002/pro.2647 (2015).

81 Storbeck, S. *et al.* Crystal structure of the heme d1 biosynthesis enzyme NirE in complex with its substrate reveals new insights into the catalytic mechanism of S-adenosyl-L-methionine-dependent uroporphyrinogen III methyltransferases. *J Biol Chem* **286**, 26754-26767, doi:10.1074/jbc.M111.239855 (2011).

82 Singh, W. *et al.* Conformational Dynamics, Ligand Binding and Effects of Mutations in NirE an S-Adenosyl-L-Methionine Dependent Methyltransferase. *Sci Rep* **6**, 20107, doi:10.1038/srep20107 (2016).

83 Evans, R. M. *et al.* Mechanism of hydrogen activation by [NiFe] hydrogenases. *Nat Chem Biol* **12**, 46-50, doi:10.1038/nchembio.1976 (2016).

84 Mehra-Chaudhary, R., Mick, J. & Beamer, L. J. Crystal structure of Bacillus anthracis phosphoglucosamine mutase, an enzyme in the peptidoglycan biosynthetic pathway. *J Bacteriol* **193**, 4081-4087, doi:10.1128/JB.00418-11 (2011).

85 Jegerschold, C. *et al.* Structural basis for induced formation of the inflammatory mediator prostaglandin E2. *Proc Natl Acad Sci U S A* **105**,

11110-11115, doi:10.1073/pnas.0802894105 (2008).

86 Fellner, M., Desguin, B., Hausinger, R. P. & Hu, J. Structural insights into the catalytic mechanism of a sacrificial sulfur insertase of the N-type ATP pyrophosphatase family, LarE. *Proc Natl Acad Sci U S A* **114**, 9074-9079, doi:10.1073/pnas.1704967114 (2017).

87 Hara, K. Y. & Kondo, A. ATP regulation in bioproduction. *Microb Cell Fact* **14**, 198, doi:10.1186/s12934-015-0390-6 (2015).

88 Burkhart, B. J., Kakkar, N., Hudson, G. A., van der Donk, W. A. & Mitchell, D. A. Chimeric Leader Peptides for the Generation of Non-Natural Hybrid RiPP Products. *ACS Cent Sci* **3**, 629-638, doi:10.1021/acscentsci.7b00141 (2017).

89 Levengood, M. R., Patton, G. C. & van der Donk, W. A. The leader peptide is not required for post-translational modification by lacticin 481 synthetase. *J Am Chem Soc* **129**, 10314-10315, doi:10.1021/ja072967+ (2007).

90 Khusainov, R. & Kuipers, O. P. When the leader gets loose: in vivo biosynthesis of a leaderless prenisin is stimulated by a trans-acting leader peptide. *Chembiochem* **13**, 2433-2438, doi:10.1002/cbic.201200437 (2012).

91 Yan, K. P. *et al.* Dissecting the maturation steps of the lasso peptide microcin J25 in vitro. *Chembiochem* **13**, 1046-1052, doi:10.1002/cbic.201200016 (2012).

92 Hemsley, A., Arnheim, N., Toney, M. D., Cortopassi, G. & Galas, D. J. A simple method for site-directed mutagenesis using the polymerase chain

reaction. *Nucleic Acids Res* **17**, 6545-6551, doi:10.1093/nar/17.16.6545 (1989).

93 Otwinowski, Z. & Minor, W. Processing of X-ray diffraction data collected in oscillation mode. *Methods Enzymol* **276**, 307-326 (1997).

94 McCoy, A. J. *et al.* Phaser crystallographic software. *J Appl Crystallogr* **40**, 658-674, doi:10.1107/S0021889807021206 (2007).

95 Adams, P. D. *et al.* PHENIX: a comprehensive Python-based system for macromolecular structure solution. *Acta Crystallogr D Biol Crystallogr* **66**, 213-221, doi:10.1107/S0907444909052925 (2010).

96 Emsley, P. & Cowtan, K. Coot: model-building tools for molecular graphics. *Acta Crystallogr D Biol Crystallogr* **60**, 2126-2132, doi:10.1107/S0907444904019158 (2004).

97 Liebschner, D. *et al.* Polder maps: improving OMIT maps by excluding bulk solvent. *Acta Crystallogr D Struct Biol* **73**, 148-157, doi:10.1107/S2059798316018210 (2017).

98 Veleti, S. K., Petit, C., Ronning, D. R. & Sucheck, S. J. Zwitterionic pyrrolidine-phosphonates: Inhibitors of the glycoside hydrolase-like phosphorylase Streptomyces coelicolor GlgEI-V279S. *Org. Biomol. Chem.* **15**, 3884, doi:10.1039/C7OB00388A (2017).

99 Radwan-Olszewska, K., Palacios, F. & Kafarski, P. Selective synthesis of alpha-fluoro-beta-keto- and alpha-fluoro-beta-aminophosphonates via electrophilic fluorination by selectfluor. *J Org Chem* **76**, 1170-1173, doi:10.1021/jo102276y (2011).

100 Chambers, R. D. & Hutchinson, J. Elemental fluorine. Part 9 - Catalysis of

the direct fluorination of 2-substituted carbonyl compounds. *J Fluorine Chem* **92**, 45-52, doi:Doi 10.1016/S0022-1139(98)00254-1 (1998).

101 Zhao, H. Y., Feng, Z., Luo, Z. & Zhang, X. Carbonylation of Difluoroalkyl Bromides Catalyzed by Palladium. *Angew Chem Int Ed Engl* **55**, 10401-10405, doi:10.1002/anie.201605380 (2016).

국문초록

리보솜 합성 및 번역 후 변형 펩타이드(RiPP)는 펩타이드 사슬에 다양한 번역 후 변형을 갖는 천연물의 일종이다. RiPP 의 단순한 생합성 및 광범위한 기질 다양성으로 인해 생물 활성을 갖는 분자 개발의 좋은 후보로 여겨진다. 따라서 RiPP 생합성 시스템은 이용하여 새로운 생체 기능 분자를 개발하려는 시도가 많고, RiPP 생합성 시스템을 효율적으로 이용하기 위한 메커니즘 연구 또한 활발하다. 본 연구에서는 아미노산 잔기 사이의 에스터 또는 아마이드 결합을 갖는 RiPP 의 일종인 graspetide 의 생합성 분자 기반을 이해하기 위한 모델 시스템으로 plesiocin 의 생합성 유전자 클러스터를 선택했고 graspetide 생합성의 분자적 세부 사항을 밝히기 위해 생화학적, 구조적 분석을 수행했다. 제 1 장에서는 RiPP 생합성에 대한 생화학적, 구조적 연구의 예와 graspetide 생합성에 대한 이전의 연구를 설명하였다.

제 2 장, 제 3 장, 제 4 장에서는 plesiocin 생합성에 대한 생화학적, 구조적 연구를 서술하였다. plesiocin 은 graspetide 의 일종으로 보존된 트레오닌과 글루탐산 잔기 사이에 8 개의 에스터 결합을 갖는 물질이다. ATP-grasp 연결효소인 PsnB 는 ATP 분자를 소비하여 plesiocin 의 전구 펩타이드인 PsnA2 에 에스터 결합을 도입한다. 본 연구에서는 plesiocin 생합성에 관여하는 주요 효소 및 기질 쌍인 PsnB 와 PsnA2 를 모델 시스템으로 선택했다.

제 2 장에서는 PsnB 의 기질 결합과 효소 반응에 대한 생화학적 분석을 설명한다. 최소 전구 펩타이드는 효소 반응의 정량적 분석을 위해 설계되었다. PsnB 의 각 반응 단계에 대한 동역학적 연구는 인산화

단계와 에스터 형성 단계가 매우 긴밀하게 일어난다는 것을 보여주었다. PsnB 와 기질 사이의 결합을 측정함으로써 전구 펩타이드의 보존된 글루탐산을 통해 PsnB 와 전구 펩타이드 코어 영역 사이의 상호작용을 확인하였다. PsnB 의 기질인 리더 펩타이드, 코어 펩타이드 및 뉴클레오타이드는 효소 결합 과정에서 서로 협동성을 보였다.

제 3 장에서는 효소-기질 복합체에 대한 구조적 연구를 서술하였다. 다양한 기질과 결합한 PsnB 복합체 구조를 결정하였고 이를 통해 효소-기질 상호작용을 분자 수준에서 이해하였다. 특히, PsnB 의 보존된 Arg213 은 인산화 이전 단계에서 반응을 일으키는 글루탐산 잔기를 인식한다. PsnB 의 Arg235 는 트레오닌의 친핵성 하이드록실기를 탈양성자화하는 촉매성 염기로 작용할 것으로 제안되었다. 기질 결합 시 PsnB 의 구조 변화가 관찰되었으며, 이는 기질 결합의 협동성과 비대칭성을 일으킨다.

제 4 장에서 PsnB 촉매의 기질 결합과 반응 메커니즘의 모델이 제안되었다. 생화학적 및 구조적 결과를 결합하여, 촉매 작용에 중요한 효소 잔기와 리더 펩타이드, 코어 펩타이드의 역할을 서술하였고 효소 반응의 각 단계를 분자 수준에서 설명하였다. 종합적으로, 본 연구에서는 group2 graspetide 를 모델 시스템으로 사용하여 graspetide 생합성 과정의 메커니즘을 이해할 수 있었다.

Keywords: 천연물, RiPP, Graspetide, Omega-Ester containing peptides, ATP-grasp 연결효소, 작동 기전

Student Number: 2017-25274

Acknowledgements (감사의 말)

6년의 박사과정을 마치고 학위 논문을 제출하게 되었습니다. 박사과정 동안 많은 분들의 도움을 받았고 학위 논문을 마치면서 그 분들께 감사의 말씀을 전합니다.

먼저 학위 과정 동안 저를 잘 이끌어주시고 지도해주신 김석희 교수님께 감사드립니다. 교수님의 가르침 덕분에 연구 내용뿐만 아니라 연구자로서 학문을 대하는 자세를 배울 수 있었습니다. 또한 공동연구를 통해 많은 가르침 주신 송윤주 교수님과 이홍근 교수님께 감사드립니다. 학위논문 심사를 맡아 주시고 많은 조언을 해주신 이연 교수님, 이형호 교수님, 송윤주 교수님, 그리고 기정민 교수님께도 감사드립니다.

학부생 시절부터 사수로서 연구의 많은 부분을 지도해주시고 연구 외적으로도 많은 도움 주신 김성재 선배님께 감사의 말 전해드립니다. 함께 실험하고 연구 내용에 대해 많은 이야기를 나눈 김영현 학생과 공동연구를 통해 연구 과정에 많은 도움을 주고 새로운 분야에 대한 이해를 넓혀준 유재승, 고수용 학생에게도 감사의 말을 전합니다. 연구 과정에서 겪은 어려움을 함께 고민해주고 해결해준 실험실 멤버들인 박효진, 엄가을, 조현진, 이현빈 박사님들 그리고 서대제, 노희진, 남현성, 이찬우, 양기정, 김혜원, 박현규에게도 감사드립니다. 부사수로서 함께 실험하면서 함께 공부한 김서연, 박민찬, 심우열, 김용아, 이권재, 우승연, 박용주, 황동민 인턴 친구들도 감사드립니다. 끝으로 긴 학위 과정을

묵묵히 기다려 주시고 응원해주신 부모님과 동생에게도 감사의 인사 전합니다.

학위 과정을 통해 정말 많은 것을 배웠고 많은 분들의 도움 덕분에 성장할 수 있었습니다. 지금까지의 배움을 밑거름 삼아 앞으로도 좋은 연구자, 좋은 어른이 되도록 노력하겠습니다. 감사합니다.